2019

Development of nanophotonic biosensor platform towards on-chip liquid biopsy

Yifei Wang
Iowa State University

Development of nanophotonic biosensor platform towards on-chip liquid biopsy

by

Yifei Wang

A dissertation submitted to the graduate faculty

in partial fulfillment of the requirements for the degree of

DOCTOR OF PHILOSOPHY

Major: Electrical Engineering

Program of Study Committee:
Meng Lu, Co-major Professor
Liang Dong, Co-major Professor
Michael Kimber
Long Que
Mani Mina

The student author, whose presentation of the scholarship herein was approved by the program of study committee, is solely responsible for the content of this dissertation. The Graduate College will ensure this dissertation is globally accessible and will not permit alterations after a degree is conferred.

Iowa State University

Ames, Iowa

2019

TABLE OF CONTENTS

Page

LIST OF FIGURES

Page

LIST OF TABLES

Page

NOMENCLATURE

BIC	Bound state in the continuum
sHCG	Slotted high-contrast grating
HCG	High-contrast grating
EV	Exosome vesicle
PC	Photonic crystal
Q	Quality factor
S/N	Signal-to-noise
SPR	Surface plasma resonance
RI	Refractive index
High-*Q*	High-quality factor
GMR	Guided-mode resonance
1D	One-dimensional
2D	Two-dimensional
SPRi	Surface plasma resonance imaging
CCD	closed circuit display
TE	Transverse electric
TM	Transverse magnetic
RIU	Refractive index unit
RCWA	Rigorous coupled-wave analysis
FEM	Finite-element method
DFB	Distributed feedback
SOI	Silicon on insulator

SNPs	Silicon nanoposts
GO	Graphene oxide
PDMS	Polydimethylsiloxane
ELISA	enzyme-linked immunosorbent assay
PVA	Polyvinylamine
GA	Glutaraldehyde
BSA	Bovine serum albumin
SEM	Scanning electron microscope
PBS	Phosphate buffered saline
UV	Ultraviolet
DI	Deionized water
ROC	Receiver operator characteristic

ACKNOWLEDGMENTS

It is a wonderful and memorable experience at Iowa State University (ISU). I would like to thank all of the people who have supported me during my pursuing a Ph.D. and beyond.

First, I want to express my sincere gratitude to my major professors, Prof. Meng Lu and Prof. Liang Dong, for their guidance and support during my study over the past five years. They have helped me to broaden my horizon and provided me with many valuable suggestions for my future career. I believe I am the luckiest one to have them as my Ph.D. advisors. My dreams do not come true at ISU without them.

Secondly, I would like to thank my committee members, Prof. Long Que, Prof. Michael Kimber, and Prof. Mani Mina, for their guidance, discussion, and support throughout the whole process of this research project.

Thirdly, I would like to thank all my colleagues from Laboratory of Integrated Optical Sensors, Laboratory for MEMS & Biochips, and my colleagues in 2135 Coover with whom I have had a pleasant and precious time in my Ph.D. life.

I would also like to thank Prof. Jiming Song for valuable discussions on the optical bound states in the high-contrast grating project. Also, thanks to Dr. Edmond K.C. Chow at the UIUC's Micro and Nanotechnology Laboratory for device fabrication in the optofluidic metasurface project. I would like to thank Dr. Leung Wai at the ISU's Microelectronics Research Center for his help with microfabrication.

I would like to acknowledge the U.S. National Science Foundation under Grant Nos. ECCS 17-11839 and ECCS 16-53673, the Catron Center for Solar Energy Research

for the Carton Graduate Fellowship, and the Warfield Graduate Scholarship for the generous support to my research presented in this dissertation.

Last, but not least, I would also like to thank my family, my parents, my wife, and my lovely daughter for their unconditional love, trust, and accompany. Without them, I definitely cannot make my journey wonderfully.

ABSTRACT

Liquid biopsy has the potential to enable diagnosis, prognosis, and monitoring of some diseases at an early stage using body fluids from patients. This minimally invasive, label-free detection method is less likely to harm the cell's viability through binding to the surface protein. Smart integration of liquid biopsy designs with microfluidics on a single chip will lead to a considerable reduction in the detection time (due to controlled diffusion length), and the volumes of sample, agent and reagent, and the limit of detection.

Optical label-free biosensors are a powerful tool to analyze biomolecular interactions and have been widely studied in the field of biomedical and biological science and engineering. Label-free detection enables direct measurement of key characteristic properties of the chemical compound, DNA molecule, peptide, protein, virus, or cell, while eliminating experimental uncertainty induced by the effect of the label on molecular conformation, thus reducing the time and effort required for bioassay. Existing optical label-free biosensors suffer from three limitations, including low detection sensitivity, slow molecules mass transfer, and poor throughput. The goal of this dissertation is to overcome these limitations through the development of a novel and efficient modality towards liquid biopsy-based bioassay with increased detection sensitivity, speed, and throughput.

To increase the detection sensitivity, we investigate the optical bound states in the continuum (BIC) of slotted high-contrast grating (sHCG) structures. We demonstrate that the sHCG support BICs and high-Q resonant modes, and the slot position can be utilized to tune and optimize the linewidth of the high-Q resonances. To overcome the mass-

transfer limitation and reduce the assay time, we propose a lateral flow-through optical biosensor integrating high-contrast gratings and microfluidics on a silicon-on-insulator platform. The biosensor design allows reducing the diffusion length to a submicron scale and enhancing direct interactions between the analytes and sensing structures. Finally, we develop a high-throughput, label-free exosome vesicles (EVs) detection microarray formed on a photonic crystal (PC) biosensor surface. We design and implement a hyperspectral imaging approach to quantify the antibody and EV absorptions on the PC-based microarray consisting of a panel of seven antibodies specific to multiple membrane receptors of the target EVs. We validate that the EV microarray by adopting it to detect EVs released by macrophages for the analysis of immune responses.

CHAPTER 1. INTRODUCTION

1.1 Background and Motivation

Currently, existing optical label-free biosensors suffer from three major limitations: insufficient detection sensitivity, slow mass transfer, and poor throughput. This dissertation seeks to develop a new modality able to overcome these limitations. First, we describe the background of the optical label-free sensing. Then, we look into the challenges of label-free biosensors and come up with our solutions, including (1) designing high-contrast gratings with a high-quality (Q) factor to improve the detection sensitivity; (2) developing a rapid, lateral flow-through, optofluidic biosensor to overcome the mass-transfer limitation; and (3) developing a label-free imaging-based microarray to achieve the high-throughput molecular profiling of exosome vesicles (EVs). Lastly, we outline the work presented here.

Liquid biopsy has significant advantages over traditional tumor biopsies [1-4]. Generally, cancer cells secrete cytokines, chemokines, and nucleic acids that have traditionally served as biomarkers for disease diagnosis and prognosis. Consequently, several detection assay methods have been developed to perform cell-based assays. The biosensor-based detection approaches can be broadly classified into label-based and label-free types. Label-based detection relies on the specific properties of labels for detecting a particular target. For example, fluorescence labeling [5-9], chemiluminescence [10-12], and radiolabeling labeling [13-15] are three popular label-based techniques. The principle of the fluorescence biosensor is that the target molecules with labeled reagents, such as antigens with fluorophore are loaded on the surface immobilized by the probe molecules. Although fluorescence-based biosensors can be thought of as the short-time category of luminescence, the labeling of biomolecules with fluorescent or other similar tags for detection can result in

sample losses during the labeling and purification process and occasional loss of functionality.

In contrast, label-free detection does not require labeling of ligand or receptor [16-21]. Optical label-free biosensors can screen for biologically active molecular interactions and cellular responses, and provide detailed information on selectivity, kinetics, and binding affinity. The approach is suitable to detect target molecules that are not labeled or screen analytes that are not easy to tag. Because the label-free biosensors skip the labeling process, they can greatly simplify the time and effort required for assay development, thus offering rapid and simplified assays [22-30]. Among various biosensor systems, label-free optical biosensors often have faster response and higher signal-to-noise (S/N) ratio [31], and thus are regarded as a new generation of analytical modalities for studying biomolecular binding, recognition, and function.

In the category of label-free biosensors, surface plasmon resonance (SPR) initially dominated commercial label-free biosensor solutions [32, 33]. Recently, other optical label-free biosensors have emerged with much higher performances than SPR using various optical structures such as slot waveguide [34], ring and disk resonators [35], interferometer [36], and porous materials [37]. These new label-free biosensors have the potential to meet the biosensing need in the field of biomedical and biological science and engineering, including apoptosis, bacteriology, virology, molecular engineering, cell biology, cell adhesion, signal transduction, immune regulation, and enzyme mechanisms.

1.2 **Photonic crystals and high-contrast gratings**

Clinical diagnostic assays require high sensitivity of label-free detection of biomolecules (e.g., virus, DNA, and proteins). Although most of the refractive index (RI) based biosensors have been proposed, high-quality (high-*Q*) optical sensors are perhaps the

most sensitive label-free sensors to enhance light interactions with the sensing target such as proteins. These biosensors use micro/nanophotonic structures to supports multi-pass light owing to the difference in refractive index between the photonic structures and surrounding. The light confinement leads to an increased effective interaction length, and thus a high-*Q* factor for obtaining high sensitivity of the sensors.

Photonic Crystal (PC) is a periodic optical structure that has the dielectric constant variation to control the flow of light. A PC slab can be seen as a diffraction grating and a waveguide brought into proximity. It is often obtained by depositing a dielectric thin film with a relatively high refractive index onto a sub-wavelength periodic structure. The PC in the form of a sub-wavelength grating is essentially a narrowband optical reflector that reflects a particular wavelength of a broadband excitation.

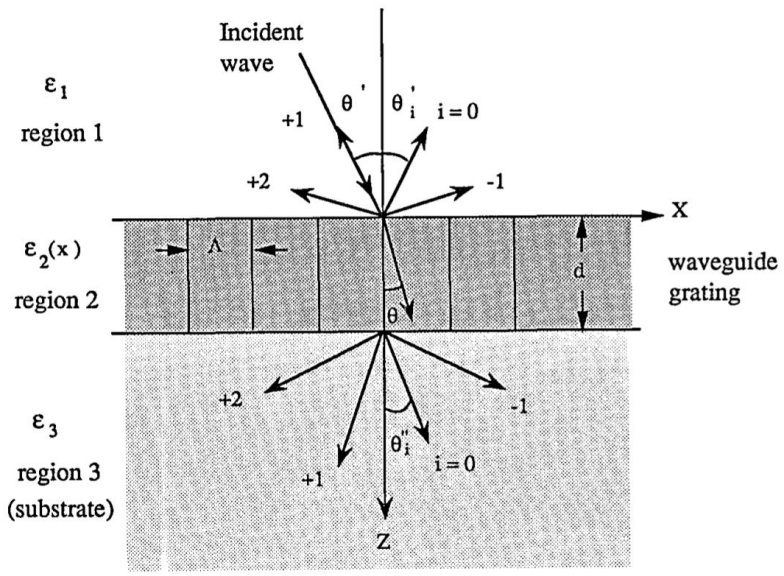

Figure 1-1 Theory of guided-mode resonance [38].

Guide-mode resonance (GMR) (shown in Figure 1-1) occurs when the diffracted mode and guided-mode meet the phase-matching condition. By taking the grating equation:

$$n_2 \sin[\theta(m)] = n_1 sin\theta_{in} - \frac{m\lambda_0}{\Lambda} sin\phi \qquad 1\text{-}1$$

and the ray-tracing analysis:

$$\beta_m = k_0 n_{eff} = k_0 n_2 \sin[\theta(m)] \quad 1\text{-}2$$

for a waveguide into account, the effective refractive index n_{eff} inside a 1D-PC can be described using Equation 1-3 :

$$n_{eff} = n_1 \sin\theta_{\text{in}} - m\frac{\lambda_0}{\Lambda} \quad 1\text{-}3$$

where n_1 is the refractive index of the cladding layer, θ_{in} is the incident angle of the excitation, λ_0 is the free space wavelength of the incident light, and Λ is the periodicity of the PC structure. The guided-mode represented when the condition satisfied:

$$\max[n_1, n_3] \leq n_{\text{eff}} < n_2 \quad 1\text{-}4$$

where n_1 and n_3 are the refractive indices of the cladding materials above or beneath the waveguide layer, respectively, and n_2 is the refractive index of the waveguide layer.

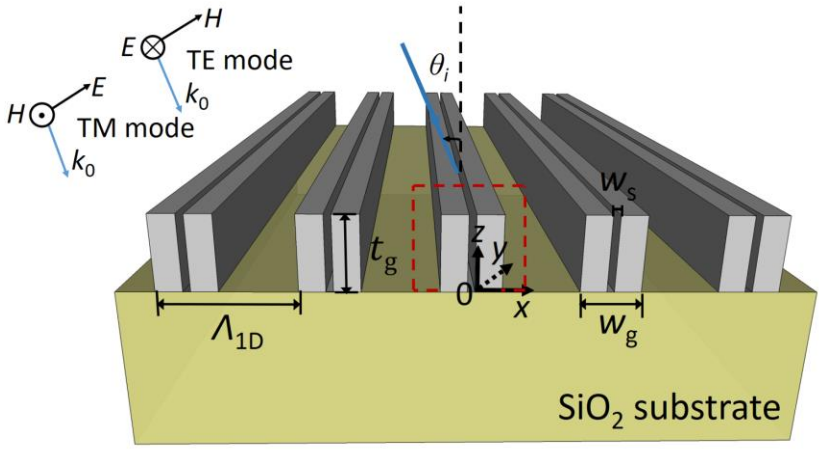

Figure 1-2 Schematic of the sHCG structure on an SOI substrate.

A high contrast grating (HCG) is a planar subwavelength grating structure, where the grating material has a greater refractive index than its surrounding materials [39]. An HCG (shown in Figure 1-2) can be engineered to display strong broadband reflection and transmission, and narrowband high-*Q* resonances. Following the demonstration of broadband

reflection, recent studies have shown that an HCG also exhibits Fano resonances with a high-*Q* factor. In 1929, von Neumann and Wigner first proposed the possibility of BICs based on potential engineering [40]. Then, the possibility has been considered by Stillinger and Herrick [41]. More recently, Yoon *et al*. numerically investigated the *TM*-polarized optical bound states in the continuum (BIC) for a one-dimensional (1D) silicon grating [42]. In these devices, the optical bound states provide ideal confinement of light in the continuum of the free-space light cone. Although the BICs do not radiate, the high-*Q* modes with quasi-embedded eigenvalues in the close vicinity of the BICs are particularly interesting, owing to their many potential applications to, e.g., optomechanics, nonlinear optics, cavity QED, and biomolecule detections. With regard to the HCG, the BICs play an important role in determining the characteristics of the radiative high-*Q* resonances. The underlying principle of guided-mode resonance (GMR) can be applied to understanding the resonances. For guided-mode resonance, the incoming light is coupled to the in-plane waveguide mode via the grating modulation with in-plane wave-vector:

$$\boldsymbol{k}_{//} = \hat{x} k_0 \sin\theta_i \pm \hat{x} G_x, \qquad 1\text{-}5$$

where $k_0 = 2\pi/\lambda$ is the free-space wavenumber and $G_x = 2m\pi/\Lambda$ with an integer m. The in-plane guided wave is scattered back into the continuum by the grating, and thus behaves as a leaky waveguide mode [43]. The constructive interference of the backward-scattered light with the zero-order reflection achieves a high-efficiency reflection. Meanwhile, the destructive interference of the forward-scattered light with the zero-order transmission produces a transmission minimum.

1.3 **Lateral flow-through assay**

1.3.1 Flow-through v.s. flow-over

To date, most of the label-free sensors employ the "flow-over" scheme, where the analytes diffuse slowly from a bulk solution to the surface of a transducer and rely on the analytes in bulk solution to diffuse to the sensing surface (Figure 1-3(a)). This approach is simple and has been commonly used but suffers from the mass transport problems that negatively affect the detection limit and slow down the detection speed. Practically, molecules are dispersed in solutions and are free to diffuse into the liquid volume. When only a small number of molecules are studied, a large sensing area often produces a relatively poor signal-to-noise ratio. On the other hand, it has been demonstrated that when the sensing area is reduced to submicron dimensions and the concentration of the solution is on the order of femtomolar, the accumulation time for the detection of a few molecules would be on the scale of days.

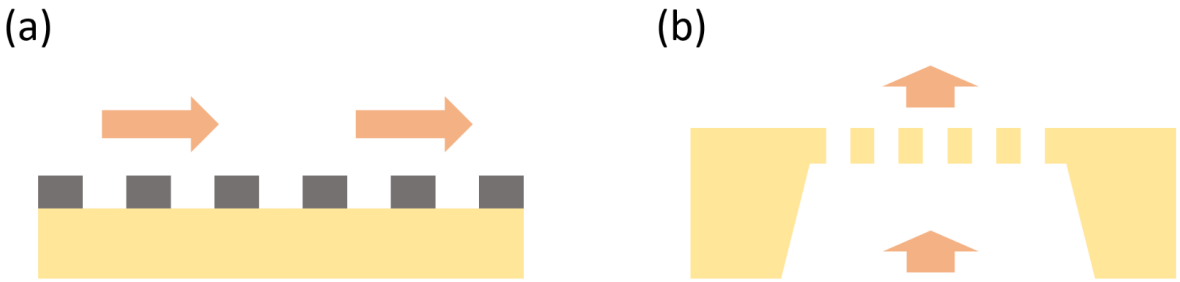

Figure 1-3 Issues with (a) conventional flow-over sensor and recent (b) vertical flow-through device

To enhance the transport of analyte to the sensor surface, recently, some vertical flow-through scheme was implemented in a few label-free sensors [44-48], where an array of nanoholes is created in a suspended dielectric or metallic membrane to form a biosensor. These nanoholes allow the analytes to pass through the porous membrane (Figure 1-3(b)).

When the analyte transport and time response of the flow-through nanohole arrays is compared with the traditional flow-over sensors in a microchannel, the transport scaling analysis indicates that flow-through sensor exhibits a Peclet number 10^2-fold less than the flow-over scheme with the same flow rate. Also, a 20-fold faster time response is achieved for the flow-through case with rapidly diffusing analytes by compare with the flow-over case based on their experimental results [46].

Due to the complex structure, these vertical flow-through devices are difficult to make and integrate with other functions (e.g., sorting) on a single chip. Therefore, a lateral flow-through device was proposed to not only overcome the issue of diffusion-limited detection that occurs in almost all conventional biosensors, but also largely simplify sensor design to achieve high S/N ratio and fast detection speed. Effective integration between label-free sensors and microfluidics is highly desirable for efficient sample delivery to achieve rapid and sensitive detection. Based on the flow over the structure, simply decreasing the height of the channel and increasing the fluidic velocity can shorten the analyte binding time. The diffusion limit will thus be overcome.

We use the finite element method to model the kinetic response of the sensor as analyte molecules in the bulk solution are transported and diffused to bind with the capture antibodies available on the sensor surface. Three processes, including the sample transport, diffusion, and surface reaction, are modeled.

1.3.2 Fluidic Kinetic analysis

1.3.2.1 Laminar flow

For the flow velocity field $\vec{u}$, the parabolic fluid flow velocity profile derived from the incompressible fluid Navier-Stokes equation with no-slip boundary condition was used.

The Navier-Stokes equation governs the motion of fluidics and can be seen as Newton's second law of motion for fluids. In the case of a compressible Newtonian fluid, this yields

$$\rho(\frac{\partial \vec{u}}{\partial t} + \vec{u} \cdot \nabla \vec{u}) = -\nabla p + \nabla \cdot (\mu(\nabla \vec{u} + (\nabla \vec{u})^T) - \frac{2}{3}\mu(\nabla \cdot \vec{u})I) + F \quad 1\text{-}6$$

where $\vec{u}$is the fluid velocity, $p$is the fluid pressure, $\rho$is the fluid density, and μ is the dynamic fluid viscosity.

1.3.2.2 Mass transport and diffused of diluted specious

At the sensor surface, the kinetic sensor responds as the analyte molecules in the bulk solution are transported and diffused to bind with the capture molecules. The governing differential equation used for the analyte concentration in the bulk solution was the convection-diffusion equation listed below as

$$\frac{\partial c_A}{\partial t} + \nabla \cdot (-D\nabla c_A + c\vec{u}) = 0 \quad 1\text{-}7$$

where c_A, D, and $\vec{u}$ are the bulk analyte concentration, bulk diffusion constant, and fluid flow velocity vector, respectively.

1.3.2.3 Surface reaction

For a one-to-one interaction in solution observed is between an immobilized ligand A and soluble ligate B, which can form a complex AB, for the reversible interaction,

$$A + B \overset{k_a k_d}{\rightleftarrows} AB \quad 1\text{-}8$$

The rate of formation of AB complexes at the time t may be written as

$$d[AB]/dt = k_a[A][B] - k_d[AB] \quad 1\text{-}9$$

where k_a is the association rate constant and k_d is the dissociation rate constant. After some reaction time *t*, $[B] = [B]_0 - [AB]$, substituting into equation (b) gives

$$d[AB]/dt = k_a[A]([B]_0 - [AB]) - k_d[AB] \quad 1\text{-}10$$

where $[B]_0$ is the total concentration of reactant B at $t = 0$.

In the biosensor, one of the reactants is immobilized to the sensor surface, and the other is continuously replenished from a solution flowing past the sensor surface. The response cAB corresponds to the amount of AB complexes formed, and the maximum response θ_0 is proportional to the surface concentration of immobilized ligand. The rate equation can thus be written as

$$dc_{AB}/dt = k_a c_A(\theta_0 - c_{AB}) - k_d c_{AB} \quad 1\text{-}11$$

where $dc_{AB}/dt$is the rate of the formation of surface complexes, c_A is the concentration of the analyte in free solution (which is the constant), $\theta_0$is the total amount of binding sites of the immobilized ligand, and $\theta_0 - c_{AB}$ is the amount of remaining free binding sites at time *t*.

At the biosensor surface, the boundary condition is represented by coupling the rate of reaction at the surface with the flux of the reacting species and the concentration of the adsorbed species and bulk species as

$$N = k_a c_A(\theta_0 - c_{AB}) - k_d c_{AB} \quad 1\text{-}12$$

where *N* is the adsorption and desorption of analyte at the reactive surfaces give rise to a net flux, which represents $\vec{n} \cdot (-D\nabla c_A + c\vec{u})$. At the inlet of the channel where the analyte solution is introduced, the boundary condition used here is $c = c_0$. At the outlet, the outflow condition is defined as $\vec{n} \cdot (-D\nabla c) = 0$, and the boundary condition of the channel wall is defined as $\vec{n} \cdot (-D\nabla c_A + c\vec{u}) = 0$. For the FEM simulation, the association rate constant and dissociation rate constant of $k_a = 1\times10^7$ $(mol/L)^{-1}s^{-1}$ and $k_d = 0.01$ s^{-1} are used. For the surface of the capture antibody, $\theta_0 = 5\times10^{-8}$ mol/m^2 is used. For the flow velocity within the channel, a Gaussian distribution profile with a velocity of 0.04 m/min is used. For the diffusion coefficient, 1×10^{-11} m^2/s is used. Therefore the Onsager coefficient of mass transport,

$$L_m \approx \sqrt[3]{\frac{D^2 \cdot v}{h^2 \cdot b \cdot l}} \qquad 1\text{-}13$$

can be calculated to be 1.2×10^{-7} m/s.

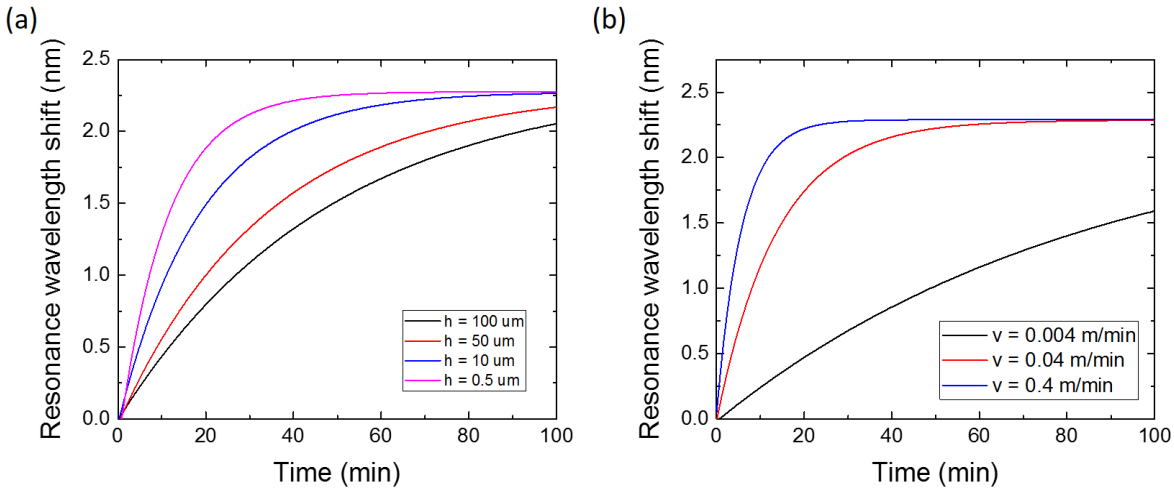

Figure 1-4 The binding process of the analyte molecules and sensor surface with (a) different channel height. (b) different velocity.

Figure 1-4 **(a)** compares the assay performance for the scenario in which the sensor is placed in the channel with the height h = 0.5 μm, 10 μm, 20 μm, and 50 μm, respectively. The height of 0.5 μm corresponds to the flow-through sensor, where the sample only flows within the interstitials between the nanoposts. Our results show that the flow-through scheme dramatically reduces the time (t_{eq}) required to establish steady-state equilibrium. For the flow-through assay, the sensor response saturates after 10 min of sample flow. Furthermore, we studied the kinetic binding response as a function of sample flow rate (Figure 1-4 **(b)**). High flow rates could result in shorter t_{eq}. These results will be used to guide the design of the sensor system.

1.4 **Microarray imaging**

Sensitivity and throughput are two key points to evaluate the performance of a label-free biosensor. We propose a high-contrast grating with a high *Q*-factor to increase the

sensitivity. To maximize the throughput of measurements, we propose a high-throughput microarray device that simultaneously performs multiple measurements on a single chip.

Generally, a microarray consists of surface-immobilized biomolecules such as DNAs, proteins, and carbohydrates. These biomolecules are spotted, imprinted, or directly synthesized on glass or silicon wafers, or other functionalized surfaces. Edwin M. Southern proposed the first simple DNA arrays, which they called “dot blots” in 1975 [49]. Later, Fodor *et al*. fabricated a DNA microarray on glass chips of using photolithographic light-directed synthesis method in 1991 [50]. Figure 1-5 shows the fluorescence scan of an array of 1024 peptides generated by a ten-step binary synthesis. Many different types of microarray technologies have been developed, and a variety of DNA microarray and DNA chip devices and systems have been commercialized. These microarray systems are being used for gene expression, genotyping, and other applications.

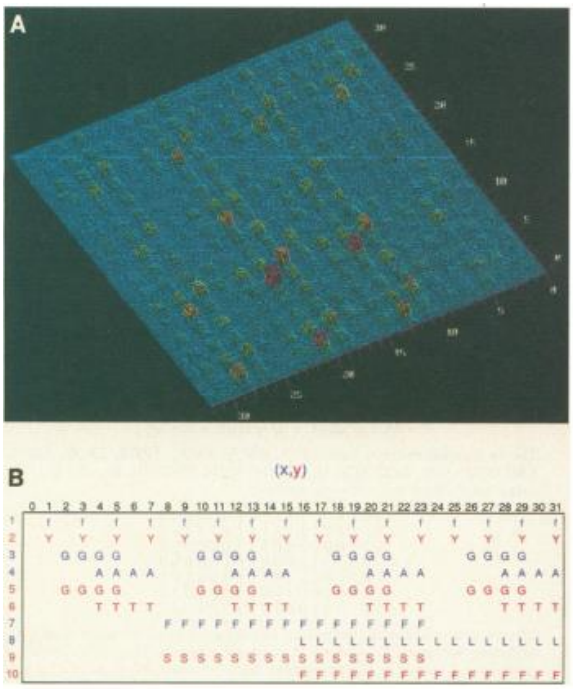

Figure 1-5 Fluorescence scan of an array of 1024 peptides generated by a ten-step binary synthesis [50].

Surface plasma resonance imaging (SPRi) microscopy (Figure 1-6) is a well-known label-free biosensor technique. SPR is suitable for studying interactions between different biomolecules in real-time and refers to the resonant oscillation of conduction electrons at the interface between negative and positive permittivity material stimulated by incident light. The SPRi measures the reflection coefficient of monochromatic incident light at a fixed angle and fixed wavelength. In this system, an expanded and collimated light is incident over the entire sensor surface. The microarray will be detected, and the reflection coefficients at different locations of the array will be imaged by using a closed-circuit display (CCD) camera. Biomolecule binding will change the surface refractive index, and the intensity of the reflected light in the corresponding CCD pixel will change proportionally. Therefore, combining the SPRi with microarray technologies allow high-throughput detection of biomolecule interactions.

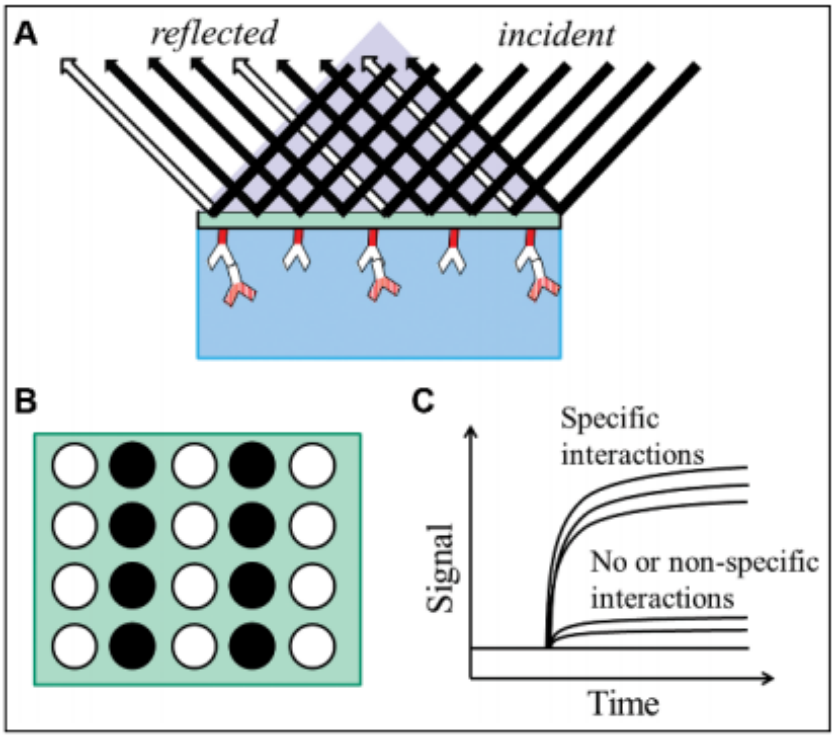

Figure 1-6 Surface plasmon resonance imaging (SPRi) microscopy [51].

SPRi requires illumination to pass through biomolecules that introduce changes in reflected light intensity that are not related to the surface attachment of the biomolecules. Also, the lateral propagation distance of surface plasmons limits spatial resolution [52]. Therefore, among the earliest developed label-free imaging modalities based on the PC biosensors [53-55], PC Enhanced Microscopy [53-59] represents a new form of optical microscopy that uses a PC surface to dynamically detect and visualize biomaterial-surface interactions (Figure 1-7).

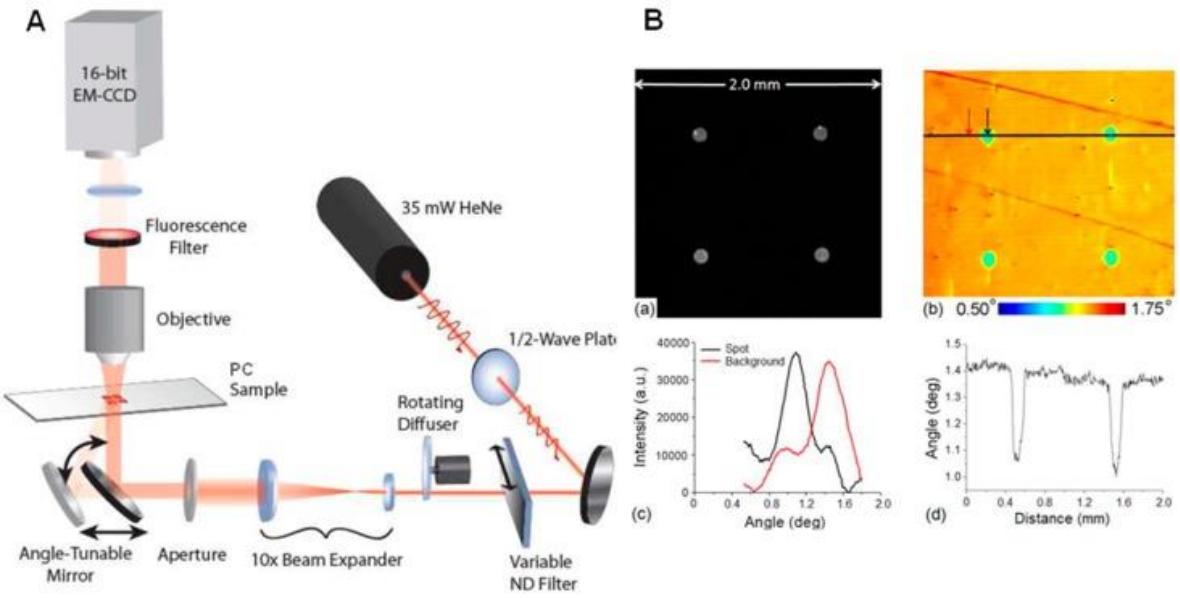

Figure 1-7 Transmission acquisition mode of photonic crystal biosensor integrated with an upright imaging microscope and using laser as light source. (A) Schematic of combined label-free and enhanced-fluorescence imaging instrument; (B) Enhanced (a) fluorescence and (b) label-free images on a PC biosensor. [60]

1.5 **Dissertation organization**

In this dissertation, I will first introduce a few key concepts extensively used in this work in Chapter 1, including the PC and HCG structures, GMRs, label-free biosensors, and flow-through biosensors.

In Chapter 2, slotted high-contrast gratings or sHCGs are developed, and the BIC modes are studied. The eigenvalue solver is used to determine the BICs. Also, the high-Q resonance phenomena for both TE (transverse electric)- and TM (transverse magnetic)-polarized cases are investigated. The sHCG device has a high index sensitivity of 368 nm/RIU (refractive index unit), thus showing the promise to explore refractive index-based sensing using the sHCG device.

In Chapter 3, based on, an HCG-based lateral flow-through biosensor is developed for the detection of cancer biomarker. The sensor design overcomes the mass transfer limitation and reduces the limit of detection. The biosensor is formed using the CMOS-compatible silicon-on-insulator technology.

In Chapter 4, we develop a label-free PC based biosensor for rapid and specific discrimination of murine host exosome vesicles (EVs) from parasite EVs extracted from the culture media.

In Chapter 5, a high-throughput EV detection assay is developed using a label-free EV microarray. The EV microarray enables low-cost, rapid, and high-throughput characterization of macrophage EVs.

In Chapter 6, we conclude this dissertation and look into our future work.

CHAPTER 2. OPTICAL BOUND STATES IN SLOTTED HIGH-CONTRAST GRATING

2.1 Abstract

This chapter investigates the optical bound states in the continuum (BIC) supported by a slotted high-contrast grating (sHCG) structure. The sHCG structure consists of a periodic array of silicon ridges with a slot in each ridge. Given that the BICs are perfectly confined, their spectral locations are identified using a finite-element method formulated from a generalized eigenvalue problem. The real eigenvalues represent the wavelengths of BIC modes and the associated eigenvectors correspond to the electric field distributions. In the spectral and angular vicinity of the BICs, the leaky waveguide modes are studied using the rigorous coupled-wave analysis. The combination of the full-wave eigenvalue solver and the coupled-wave analysis provides an ideal setting for investigating the optical BICs of periodic structures for various applications. For example, the simulation results show that the sHCG structures can support symmetry-protected bound states with zero in-plane wave vector as well as high-quality-factor (high-Q) resonances for both TE and TM polarizations. By adjusting the slot, the BIC mode can be turned into high-Q modes and the linewidth of the mode is determined by the degree of asymmetry.

2.2 Introduction

Dielectric slabs with periodic sub-wavelength features, such as photonic crystal slabs, guided-mode resonance filters, and high-contrast gratings (HCG), have attracted considerable attention for their fascinating optical properties caused by the modulation and confinement of light [39, 61-66]. Previous studies carried out on these devices have demonstrated numerous applications to high-performance optical filters [67-71], solid-state light sources [72, 73], nonlinear optics [74-78], biomolecule detection [79, 80], to name but some. Among the

grating-patterned slabs, the HCG structure, built upon a silicon-on-insulator substrate, is particularly interesting, owing to its extraordinary optical properties and compatibility with the complementary metal-oxide semiconductor process [81]. As reported by Mateus *et al.* [82] and Shokooh-Saremi *et al.* [83], a HCG device allows broadband reflection with a reflectivity more than 99% in the near-infrared wavelength regime. Following the demonstration of broadband reflection, recent studies have shown that a HCG device also exhibits Fano resonances with a high-quality factor (*Q* factor). In 1929, von Neumann and Wigner first proposed the possibility of BICs based on potential engineering [40]. Then the possibility has been considered by Stillinger and Herrick [41]. More recently, Yoon *et al*. numerically investigated the *TM*-polarized optical bound states in the continuum (BIC) for a one-dimensional (1D) silicon grating [42].

The existence of a perfectly confined optical mode within the radiation continuum was shown using a parallel dielectric grating [84], 1D periodic array of dielectric rods and spheres [85, 86], and two-dimensional photonic crystal slab [87-92] that supported a scattering resonance with a vanishing linewidth. A recent seminal work by Hsu *et al*. shows experimentally demonstrated the BICs of a2D Si_3N_4 photonic crystal slab [93]. Later, layered sub-wavelength nanoparticles were numerically designed to achieve the BIC in three-dimensional open scattering systems [94]. For these devices, the optical bound states provide an ideal confinement of light in the continuum of the free-space light cone. Although the BICs do not radiate, the high-*Q* modes with quasi-embedded eigenvalues in the close vicinity of the BICs are particularly interesting, owing to their many potential applications to, e.g., optomechanics, nonlinear optics, cavity QED, and biomolecule detections. With regard to the HCG, the BICs play an important role in determining the characteristics of the radiative high-

Q resonances. However, the relations between the broadband reflective modes, high-*Q* modes, and BICs have not yet been systematically studied.

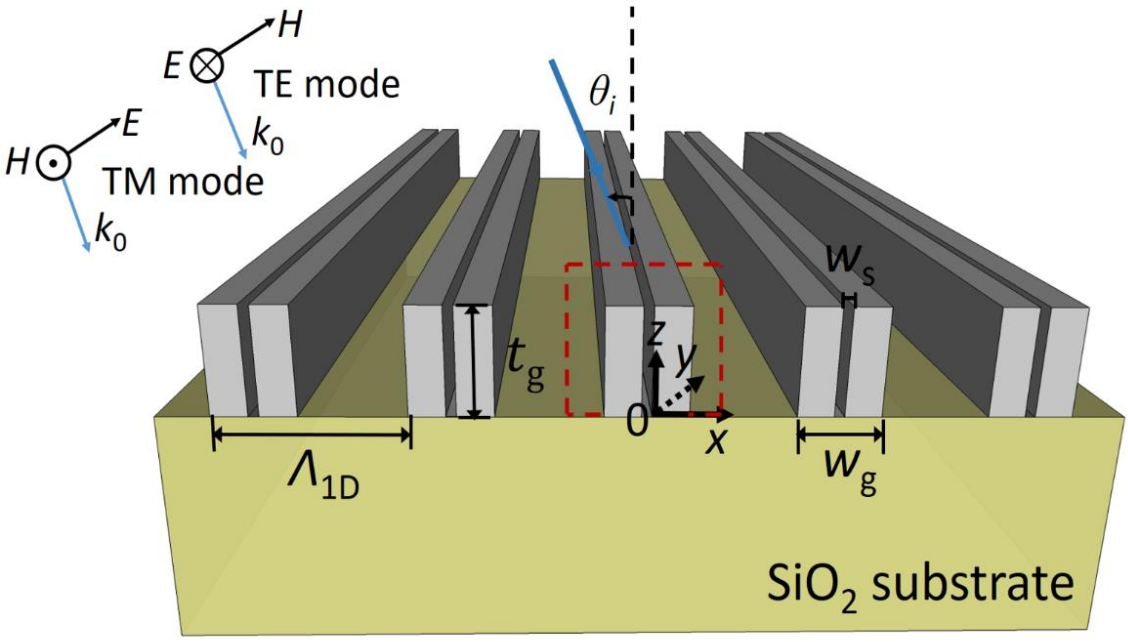

Figure 2-1 Schematic of 1D sHCG structure on a SiO_2 substrate. (Not to scale). The 1D sHCG consists of an array of slotted nano-ridges. The device is excited by a plane wave at an incidence angle of θ_i. The TE- and TM-polarized modes correspond to the modes with the electric field component parallel and perpendicular to the grating lines, respectively.

This paper investigates the TE- and TM-polarized BICs and high-*Q* resonance modes of a silicon-based slotted HCG (sHCG). As shown in Figure 2-1, the sHCG has a rectangular nanoslot cut into each ridge of the grating. The position of slot in the ridge can determine the resonant characteristics of the device. Since the slot can be fabricated along with the HCG structure using a lithography process, the proposed structure is ready for manufacture. Although previous studies utilized rigorous coupled-wave analysis (RCWA) or a finite-difference time-domain method to identify BICs in an asymptotic manner [42], none of these studies directly calculated the eigenfrequency of the resonance modes that do not interact with the radiation continuum. Here, we employ a finite-element method (FEM) to

solve the eigenvalue problems for the periodic structures, and consequently determine the resonance wavelengths (λ_r) and the associated mode distributions. The eigenvalue analysis shows that the BIC wavelengths increase proportionally with increasing grating period and that the number of BICs increases with increasing sHCG thickness. To acquire an in-depth understanding of the phenomena associated with the BICs, we calculated the spectral and angular reflectance of 1D SHCG structures. Furthermore, we show that breaking the symmetry in the grating design produces a transition of a BIC mode to a high-*Q* mode.

This paper is organized as follows. Section 2 specifies the SHCG structures and Section 3 describes the numerical methods used to analyze and simulate the phenomena of interest. Section 4 describes the bound states of the 1D sHCG device for two different polarizations. Section 5 demonstrates the possibility of forming an asymmetric SHCG structures to turns BICs into high-*Q* resonances. Section 6 provides concluding remarks.

2.3 **Definitions, phenomenology, and characterization techniques**

2.3.1 sHCG structure and physical principles

The sHCG structure used in this study consists of a periodic pattern made of silicon and formed on a 3-μm-thick SiO_2 buffer layer. The main geometric parameters are the grating period (Λ_{1D}), grating width (w_g), slot width (w_s), nanoslot offset from the grating center (d_s), grating-layer thickness (t_g), and duty cycle ($\eta = w_g/\Lambda$), as depicted in Figure 2-1. For the symmetry protected structure, the slot stands at the middle of the ridge, which $d_s = 0$. The period of 1D arrays is smaller than the free-space wavelength λ. The thin device layer of silicon can be patterned by lithography, followed by a reactive-ion etching process [95]. Crystalline silicon is a suitable material for fabricating high-*Q* optical devices because it is transparent in the near-infrared regime, with a negligible extinction coefficient $\kappa < 0.001$ and a large refractive index $n = 3.477$. A plane-wave excitation beam is shone on the device from

the grating side. As shown in the schematic view of the sHCG devices (Figure 2-1), the incident angle θ_i is measured from the normal of the grating surface Incident plane waves with their electric field polarized parallel or perpendicular to the grating bars are described as having transverse-electric (TE) or transverse-magnetic (TM) polarizations, respectively.

Optical phenomena supported by HCGs and their underlying principles have been described previously. [38, 42, 96-98] Briefly, a HCG structure can be engineered to display strong broadband reflection and transmission, and narrowband high-Q resonances. The underlying principle of guided-mode resonance can be applied to understanding the resonances. For guided-mode resonance, incoming light is coupled to the in-plane waveguide mode via the grating modulation with in-plane wavevector:

$$\boldsymbol{k}_{//} = \hat{x} k_0 \sin\theta_i \pm \hat{x} G_x, \qquad 2\text{-}1$$

where $k_0 = 2\pi/\lambda$ is the free-space wavenumber and $G_x = 2m\pi/\Lambda$ with an integer m. The in-plane guided wave is scattered back into the continuum by the grating, and thus behaves as a leaky waveguide mode [43]. The constructive interference of the backward-scattered light with the zero-order reflection achieves a high-efficiency reflection. Meanwhile, the destructive interference of the forward-scattered light with the zero-order transmission produces a transmission minimum. The BIC characteristics can be simulated using electromagnetic simulations as discussed below.

2.3.2 Numerical characterization techniques

RCWA and the finite-difference time-domain method have previously been used to study HCG devices and photonic crystals [42]. These methods can simulate the optical phenomena that occur in a structure in response to excitation, and yield the reflectance, transmittance, and near-field distribution that can then be used to guide nanostructure design.

However, these methods are unable to find non-radiative BICs directly. We therefore developed a generalized eigenvalue problem using an FEM-based solver to find all the BICs supported by the sHCG structure. The FEM simulation model included only one period of the sHCG structure. The periodic boundary condition in the *x*-direction, together with the perfectly matched layers in the *z*-direction, defined the simulation domain in the *x*-*z* plane. The simulation domain was discretized using a triangular mesh. By basing the finite-element analysis on the electric-field discretization, the variational problem that is equivalent to the wave equation (source-free) led to a generalized eigenvalue problem [99]. By solving the generalized eigenvalue equation, the eigenvalue solver yielded the eigenvalues and eigenvectors, which represent the resonance wavelength and electric field, respectively. Only the real eigenvalues correspond to the bound states with a radiative coupling coefficient of zero ($\kappa = 0$). For the sHCG structure shown in Figure 2-1, we used the eigenvalue solver to determine the BICs for different device geometries. The details and equations involved in the FEM analysis are given in the Appendix.

After finding the BICs, we used the RCWA method to study the BICs in an asymptotic manner. The RCWA algorithm is based on the Fourier expansions of the electromagnetic fields and the permittivity profiles ($\varepsilon_r(x, y)$) in each layer of a periodic structure. The diffraction efficiencies for each harmonic in the Fourier expansion were calculated to determine the reflectance or transmittance. The analysis was carried out using a commercial RCWA software package (DiffractMOD, Synopsis). The RCWA simulation was set up to analyze a unit volume of the HCG structures, and periodic boundary conditions were applied to define the calculation domain, as labeled by the dashed box in Figure 2-1. Twenty harmonics were used to expand the permittivity and fields along the *x*-direction. The

dispersive and complex refractive indices of crystalline silicon, $n(\lambda) = n_{si}(\lambda) + i\kappa_{si}(\lambda)$, were taken from Palik's handbook [100], where $n_{si} = 3.486 + i0.001$ at $\lambda = 1550$ nm. The reflection and transmission spectra were calculated in the desired near-infrared wavelength range.

2.4 **Eigenvalue analysis of silicon-based sHCGs**

The eigenvalue solver was applied to study how the geometric parameters of the silicon grating affect the BICs and illustrate the principles behind the sHCG-supported BICs. Material loss was neglected by assuming $\kappa_{si} = 0$, leaving out-of-plane scattering as the only loss mechanism. As a result, the real eigenvalue solutions correspond to the perfectly confined BICs and those with an imaginary part are associated with the modes coupling with the radiation continuum. To characterize resonances supported by sHCGs with different grating periods, we considered sHCG structures with a thickness, duty cycle, slot width of t_g = 500 nm, η = 50%, w_s = 50 nm, respectively. As for the periodic boundary condition described in Eq. A (3), the phase shift was set to $\phi = 0$, representing the normal incidence case with $\theta_i = 0°$. The grating period ranges from Λ = 500 to 1800 nm with the increment of 50 nm. Eigenvalues were solved for each grating period, but only the real eigenvalues are plotted in Figure 2-2(a) as the BIC resonant wavelengths. The eigen-wavelengths can be grouped into three branches. The two branches shown in black represent the TE modes (TE_{10} and TE_{11}) and the one shown in red is the TM_{10} mode. The modes are labeled as TE_{mn} (or TM_{mn}), where the integers m and n are determined by the distribution of the longitudinal component of the field along x- and z-axes, respectively. The polarizations of these modes were determined by the electric-field components given by the eigenvectors. Here, the high refractive index grating-patterned silicon slab provides the in-plane confinement. The Bragg condition gives the resonance wavelength,

$$\lambda = 2\mathrm{n}_{eff}\Lambda/m \qquad 2\text{-}2$$

where n_{eff} is the effective waveguide index and m is a positive integer that denotes the order of diffraction. According to the Bragg condition, the resonance wavelength increases with the grating period, in agreement with the simulation results shown in Figure 2-2(a).

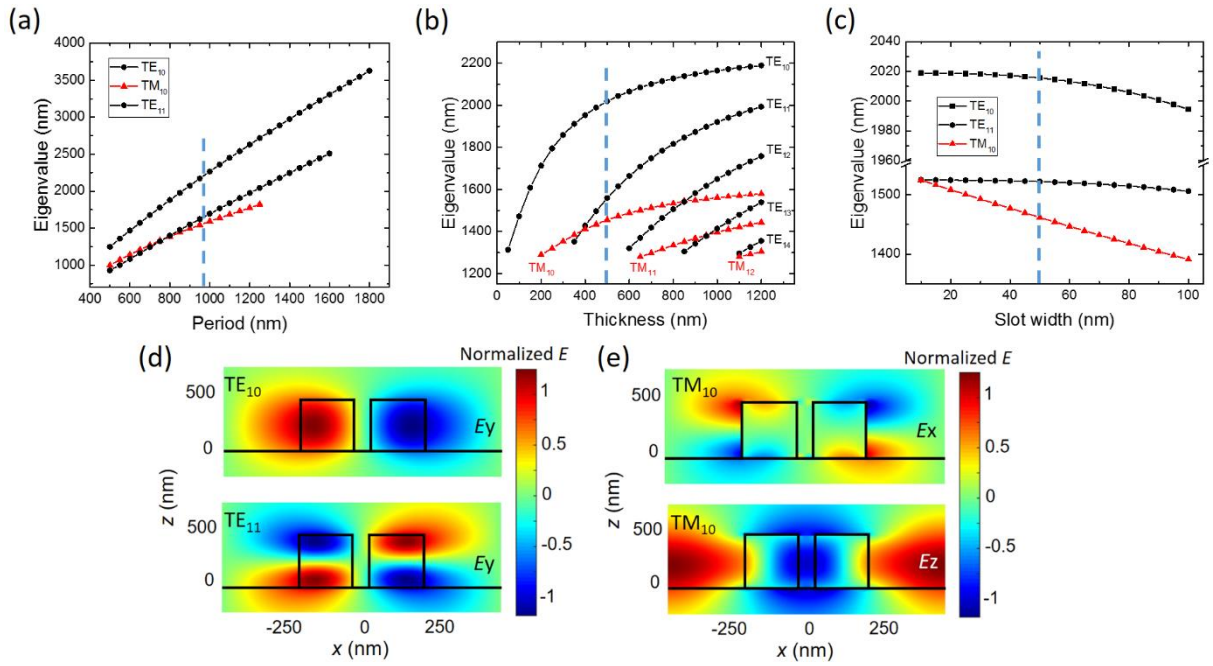

Figure 2-2 Eigen-wavelength calculated as a function of (a) the grating period and (b) the grating thickness (c) the slot width. (d) Eigenvectors of the TE_{10}, and TE_{11} modes when Λ = 880 nm, η = 50%, and w_s = 50 nm labeled by the blue line. For the TE modes, the E_y components at the corresponding wavelength 2012 nm and 1519 nm are plotted in the upper and lower panels, respectively. (e) Eigenvectors of the TM_{10} mode. The E_x and E_z components of the TM_{10} mode are shown in the top and lower panels at λ_r = 1459 nm.

Figure 2-2(b) shows the eigen-wavelengths calculated as functions of the grating thickness when the grating period and duty cycle are fixed at Λ = 880 nm and η = 50%, respectively. The grating thickness increases from t_g = 50 to 1200 nm with the increment of 50 nm. The number of BIC modes can be estimated as $\#_{BIC} = \frac{2t_g}{\lambda}\sqrt{n_{avg}^2 - n_{cladding}^2}$, where n_{avg} can be estimated using the average refractive index of the patterned slab. As shown in Figure 2-2(b), the number of BIC modes increases with increasing grating thickness. Single-

mode operation occurs when the grating thickness is less than 200 nm. For each mode, the BIC wavelength shifts to the red end as the grating thickness increases. Figure 2-2(c) shows the eigen-wavelengths calculated as a function of the slot width ranging from 10 nm to 100 nm. As shown in the Figure 2-2, the BIC wavelength decreases when the slot widens for all three modes (TE_{00}, TE_{11}, and TM_{10}). The blueshift of the resonant wavelength is owing to the decrease of the averaged refractive index when the slot becomes wider.

Next, the field distributions of the BICs were studied using the eigenvectors associated with the real eigen-wavelengths. To this end, we considered a 1D sHCG device with grating period Λ = 880 nm, grating thickness t_g = 500 nm and slot width 50 nm. This particular device supports three BICs at λ_r = 1455.1, 1558.4, and 2018.7 nm, respectively. The modes at λ_r = 1455.1 and 2018.7 nm are TE-polarized modes with only the E_y components shown in the top and bottom panels of Figure 2-2(d). The eigenvectors of the E_x and E_z components are trivial and are therefore omitted from the Figure 2-2. The mode at λ_r = 1558.4 nm is a TM-polarized mode with its E_x and E_z components shown in Figure 2-2(e). Being a TM mode, its E_y component is trivial compared to the E_x and E_z components. The resonant field distributions indicate that the order of Bragg diffraction is m = 2. We note that the distributions of the resonant fields are antisymmetric and these modes can be considered to be symmetry-protected bound states. The coupling to the continuum in the surface-normal direction is forbidden because of symmetry incompatibility with the external radiation, whose tangential field components are symmetric with respect to the mirror-symmetry axis at x = 0. The BIC mode is distinct from the resonance of a distributed-feedback (DFB) cavities [101] because they reside inside the light cone of a photonic band diagram, shown in the following section. Moreover, we sought the real eigenvalues of the sHCG with the incident

light at an oblique angle ($0° < \theta_i < 90°$). For the structure shown in Figure 2-1(a), real eigenvalues are only present when $\theta_i = 0°$.

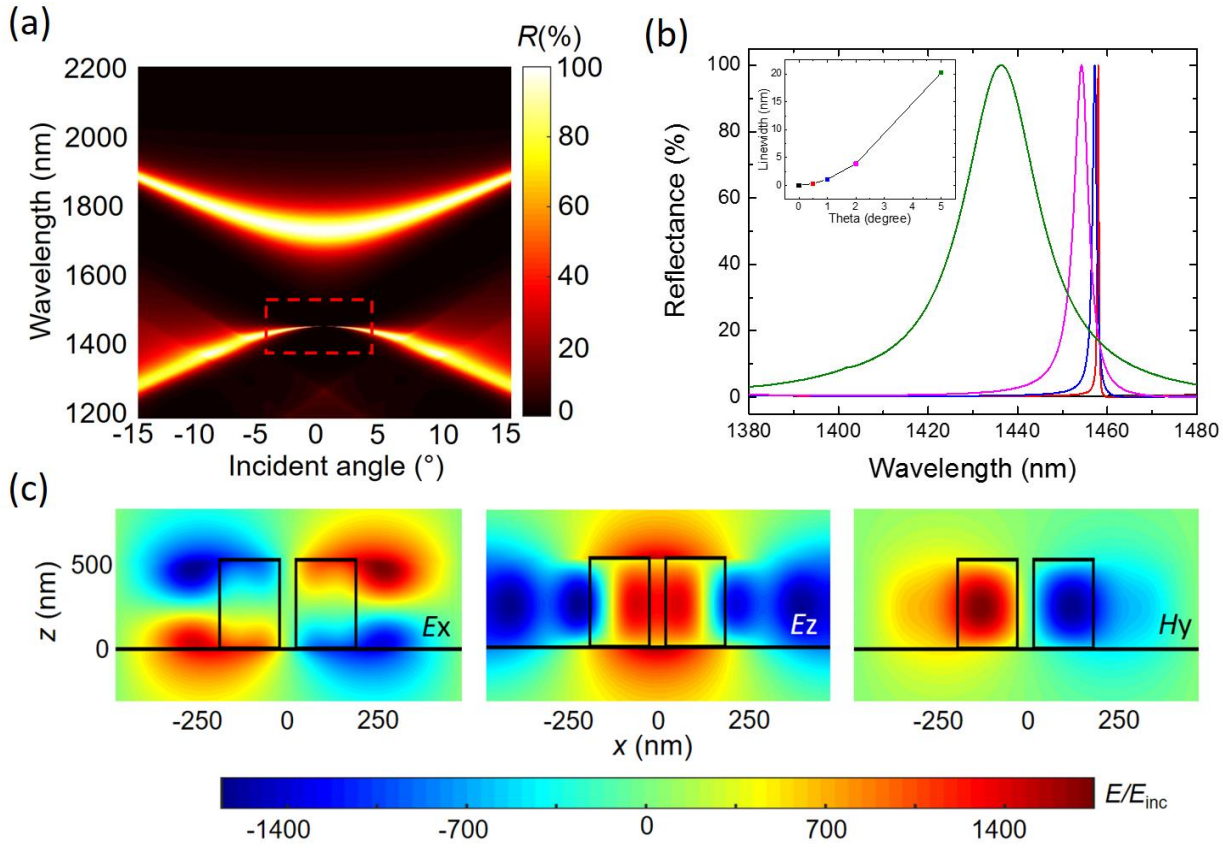

Figure 2-3 TM-mode characteristics. (a) Calculated reflection spectra in the wavelength range 1200 to 2200 nm, for incident angles ranging from -15° to 15°. (b) the reflection spectra calculated for $\theta_i = 0°$, 0.5°, 1°, 2°, and 5°. The corresponding linewidths for each angle are plotted in the inset. (c) The near-field distributions of E_x, E_z, and H_y components for the high-Q resonance (Q factor = 1.7×10^5) at $\lambda_r = 1458.3$ nm and $\theta_i = 0.01°$.

2.5 **Broadband, BIC, and high-Q modes**

The sHCG device can be designed to exhibit a single BIC mode when $t_g < 200$ nm. To illustrate the couplings between the broadband reflection, the high-Q mode, and the BIC, we selected a design that supports both TE and TM modes. The device consists of a grating with period $\Lambda = 880$ nm, thickness $t_g = 500$ nm, and slot width $w_s = 50$ nm. As shown in Figure 2-2 (a) and (b), there should be two TE modes and one TM mode. We first study the

TM mode. The calculated reflection spectra are plotted as functions of the incident angle in Figure 2-3(a). The wavelength and incident angle range from 1200 to 2200 nm and from -15° to 15°, respectively. The TM-polarized resonances appear as reflection peaks. In contrast, the HCG structure without the slot exhibits the TM-polarized resonances as narrowband dips [102]. In Figure 2-3(a), the region indicated by the red box contains the BIC and high-Q modes. To elaborate on these phenomena, the reflection spectra calculated for θ_i = 0°, 0.5°, 1°, 2°, and 5° are compared in Figure 2-3(b). The resonant linewidth decreases significantly as the incidence angle approaches 0°. For example, when the incident angle is 1°, the resonance linewidth is 1.1 nm, which corresponds to a Q factor of 1305. In comparison, the Q factor increases to 4766.6 nm when θ_i is reduced to 0.5°. The vanishing of the linewidth at θ_i = 0° implies the existence of BIC. As shown in Figure 2-3(b), the BIC mode locates at λ_r = 1458 nm in the spectrum, in agreement with the eigenvalue analysis. Because the TM mode displays a weak reflection in the spectral range of interest, the high-Q resonance modes are displayed as peaks with a high reflectance at the resonant wavelength.

The near-field distribution of a representative high-Q mode is calculated using the RCWA simulation and shown in in Figure 2-3(c). Here, the near-field distributions of the E_x, E_z, and H_y components are associated with the high-Q resonance (Q factor = 1.3×10^5) at λ_r = 1458.3 nm and θ_i = 0.01°. The color axis expresses the amplitudes of the electric and magnetic fields, normalized by that of the incident field. As seen from the field distributions, the maximum field enhancement factor is 1500. The enhancement factor of the field intensity is calculated by averaging the electric field intensities within the sHCG area ($-\Lambda/2 < x < \Lambda/2$ and $0 < z < t_g$). As a result, the averaged enhancement factor of the field strength is approximately 1.7×10^5. The distributions of the tangential components (E_x and H_y) are

asymmetric. The mode can be excited because the asymmetric nature of the incident wave at $\theta_i = 0.01°$.

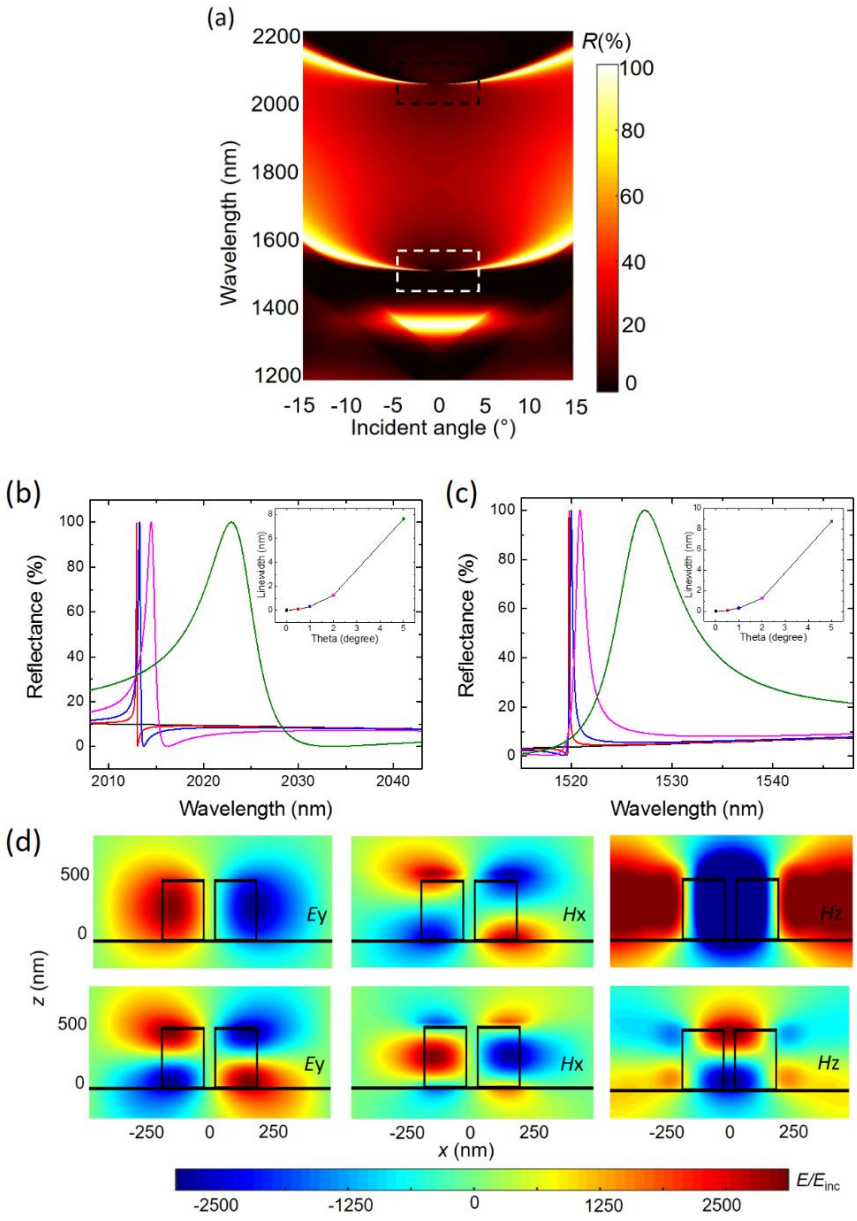

Figure 2-4 Characteristics of the TE-mode. (a) Calculated reflection spectra in the wavelength range of 1200 nm to 2200 nm as a function of incident angles from -15° to 15°. (b) The reflection spectra calculated for $\theta_i = 0°$, 0.5°, 1°, 2° and 5° for the modes around 2012.9 nm. (c) The reflection spectra calculated for $\theta_i = 0°$, 0.5°, 1°, 2° and 5° for the modes around 1519.7 nm. The corresponding of linewidth for each small angle shown in inset. (d) The near field distributions of E_y, H_x, and H_z components with the high-Q resonances (Q factor = 4×10^7) at $\lambda_r = 2012.9$ nm and $\theta_i = 0.01°$ for TE_{10} (top) and TE_{11} (bottom) mode, respectively.

Having characterized the TM mode, we used the same approach to study the TE-polarized modes. Figure 2-4(a) shows the reflection spectra of the TE modes plotted as a function of the incident angle, which ranges from -15° to 15°. As shown in Figure 2-2(b), there are two TE-polarized BIC modes (TE_{10} and TE_{11}) when the silicon grating thickness is 500 nm. In Figure 2-4(a), the regions of the TE resonances are outlined by the black (TE_{10} mode) and white boxes (TE_{11} mode), respectively. Figure 2-4 (b) and 4(c) summarizes the reflection spectra for θ = 0°, 0.5°, 1°, 2°, and 5° for the TE_{10} and TE_{11} modes, respectively. Like the TM resonances, the TE modes also display as peaks in the reflection spectra. Also, the TE resonance linewidth decreases as the incidence angle approaches 0° and disappears at θ = 0°. This phenomenon indicates the existence of the BICs at λ_r = 1519 and 2012 nm. The near-field distributions of a representative high-Q mode for two TE modes are plotted, as obtained using the RCWA simulation. Figure 2-4(d) shows the amplitude distribution of the E_y, H_x, and H_z components that are associated with the high-Q resonance at θ_i = 0.01° for the TE_{11} mode at λ_r = 1519.7 nm (top row) and the TE_{10} mode at λ_r = 2012.9 nm (bottom row). The tangential components (E_y and H_x) of these mode are clearly asymmetric. The near fields of both TE modes are significantly enhanced relative to the incident wave.

2.6 **Asymmetric sHCGs**

In the previous section, we showed that the transition from a BIC mode transit to a high-Q resonant mode when the sHCG is illuminated from an off-normal direction (0° < θ < 1°). Recent research demonstrated an approach for transforming the perfectly confined mode to high-Q resonances using non-equivalent sub-cells in one period of the grating [103]. Since the BIC mode with k_x = 0 is symmetry-protected, an asymmetric design of the sHCG can be exploited to eliminate the BIC and tune the high-Q resonant modes. This section

demonstrates another approach that allows the precise control of the resonance using the slot position.

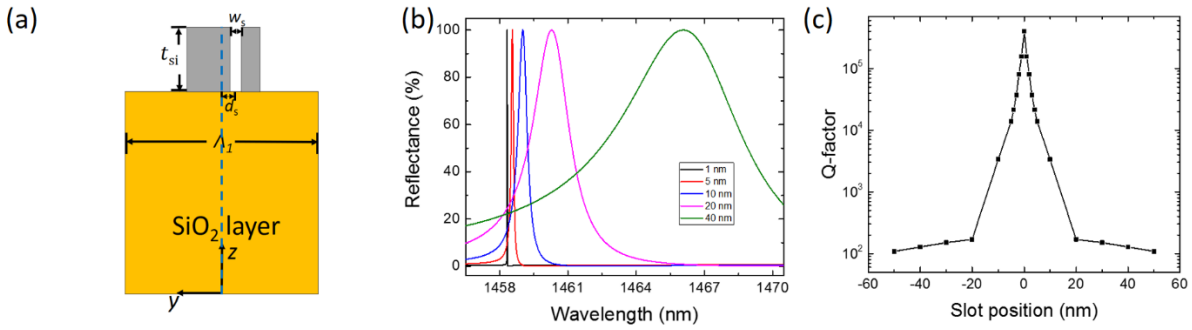

Figure 2-5 Asymmetric sHCG structure. (a) Schematics of sHCG, where the position of slot is shifted from the ridge center by a distance of d_s. (b) The reflection spectra for the asymmetric grating with d_s = 1, 5, 10, 20, and 40 nm. (c) The Q factors are plotted as functions of d_s.

As shown in Figure 2-5(a), we shift the slot from the center of the ridge to the right (or left) side with an offset of d_s. The shift of the slot results in an asymmetric sHCG structure. As a result, the symmetry-protected BIC mode disappears, and all the eigenvalues are complex. The resonant wavelength and the Q-factor are associated with the shift distance. Using the RCWA simulation, we studied the reflection characteristics of the asymmetric sHCG with the slot at off-center positions. Figure 2-5(b) shows the reflection spectra for d_s = 1, 5, 10, 20, and 40 nm, respectively, for the TM_{10} mode. The incident angle is kept at $\theta_i = 0°$ and the slot width is set as w_s = 50 nm. The resonant wavelength increases while the position of slot moves. It is clear that the resonant linewidth significantly increases as the slot approaches edge of the ridge. The device with the d_s as small as 1 nm exhibit the linewidth of 0.004 nm and the Q-factor of 3.6×10^5. Increasing d_s to 5 nm broadens the resonant linewidth to 1 nm (Q-factor of 1451). To elaborate how the resonance characteristics of the asymmetric SHCG resonator can be tuned, we summarized the Q factor as a function of slot

position in Figure 2-5(c). As shown in the figure, the Q-factor decreases exponentially with the shifting of the slot towards the edge of the ridge.

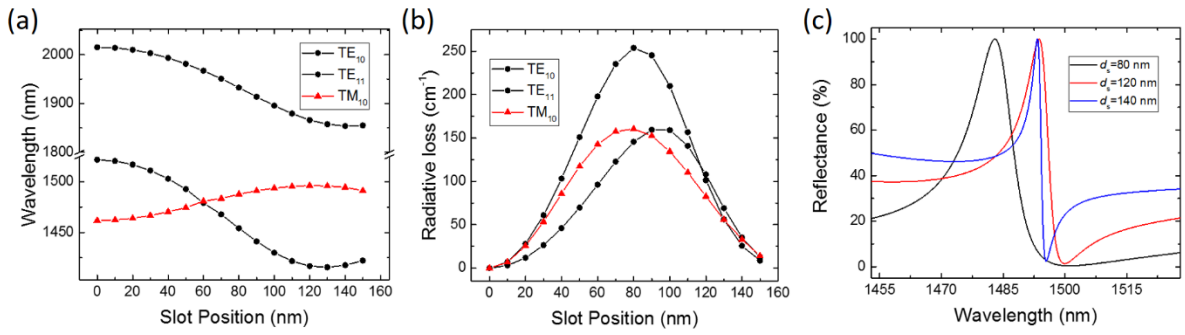

Figure 2-6 Resonant characteristics of the asymmetric sHCG structure. (a) and (b) Resonant wavelength and loss as a function of slot position for TE_{10}, TE_{11}, and TM_{10} modes, respectively. (c) Reflection spectra for the asymmetric sHCG devices with d_s = 80, 120, and 140 nm, respectively.

We also used the eigenvalue solver to study the resonant wavelength and loss of the asymmetric sHCG devices. In the case of $d_s \neq 0$, all the eigenvalues are complex numbers. The real part of the complex number is the resonant wavelength of the asymmetry sHCG. Figure 2-6(a) shows the calculated eigen-wavelength as a function of the slot position. The resonant wavelengths of both TE_{01} and TE_{11} modes decrease with the moving of the slot away from the center of the ridge. On the other hand, the resonant wavelength of the TM_{10} mode increases while increasing the d_s. The breaking of device symmetry introduces radiation loss, which depends on the position of the slot. The radiation loss can be calculated using the imaginary part of the eigenvalues when $d_s \neq 0$. Figure 2-6(b) shows the change of radiative loss as a function of the slot position. For all three modes, the loss is strong when the sHCG has the highest degree of asymmetry, which the center of the slot will be located at $w_g/4$ = 110 nm. Thus, the loss achieves maximum when d_s is approximately 85 nm. The BICs exist with zero radiative loss when the slot locates at the middle of the ridge

($d_s = 0$) and the boundary of the ridge ($d_s = 84.3$ nm). Figure 2-6(c) shows the reflection spectra when $d_s = 80$, 120, and 140nm, respectively. When d_s increases beyond 80 nm, the resonant linewidth starts to decrease.

2.7 **Conclusion**

Optical bound states and the associated high-Q resonant modes supported by silicon-based sHCG structures were studied numerically. Special attention was given to the FEM eigenvalue solver, which is capable of finding the resonant wavelength and the near-field distributions of the BICs. The results show that the number of bound states supported by a SHCG structure is determined by the silicon slab thickness. Using the calculated eigen-wavelengths, RCWA simulations were performed to characterize the resonant modes that are spectrally and angularly close to the BICs. The sHCG design investigated above displays one TM-polarized and two TE-polarized BICs. The TE- and TM-polarized resonances appear as narrowband peaks in the reflection spectra. Because the BICs are perfectly confined bound modes, they cannot be excited. The simulation of an asymmetric sHCG structure demonstrates that the BIC mode can be turned into a high-Q resonance, with the Q factor being controlled by the degree of asymmetry.

The BIC and neighboring resonant modes of the sHCG structure can be applied to the construction of high-Q optical resonators in the fields of optomechanics, nonlinear optics, and cavity QED with a tunable Q-factor by changing the coupling angle. They can also be used for refractive index-based biomolecule detection. The numerical techniques presented in this paper enable both source-excited and source-free assessments of BICs in slabs with a patterned grating. Understanding the phenomena above is an important step towards exploring more complex mechanisms involving the couplings between free-space fields, BICs, and high-Q modes.

2.8 **Appendix: Governing equations for the FEM eigenvalue solver**

The electric field in the sHCG structure satisfies the second-order wave equation

$$\nabla \times \mu_r^{-1}(\nabla \times \boldsymbol{E}) - k_0^2(\varepsilon_r + \frac{i\sigma}{\omega\varepsilon_0})\boldsymbol{E} = 0, \quad \text{in}\Omega \tag{2-3}$$

and is subject to the following condition for a perfect electric conductor and floquet boundaries:

$$\hat{n} \times \boldsymbol{E} = 0 \qquad \text{on}\Gamma_1 \tag{2-4}$$

$$\boldsymbol{E}_{F_l} = e^{i\phi}\boldsymbol{E}_{F_r} \qquad \text{on}\Gamma_2 \tag{2-5}$$

where Γ_1 and Γ_2 are the boundaries along the *z*- and *x*-axis, respectively. In equation 2-3, the relative permeability $\mu_r = 1$, and σ and ε_r denote the relative permittivity and conductivity. In equation 2-5 $\boldsymbol{E}_{F_r}$and $\boldsymbol{E}_{F_l}$are the fields at $x = 0$ and Λ, respectively, and the phase shift is given by $\phi = k_x\Lambda = k_0 \sin\theta_i\Lambda$. Perfect matching layers (PMLs) are applied along the *z*-direction to absorb the outgoing waves. In the PML regions, the anisotropic absorber model is used to create a reflection free interface [104]. Then, by applying the variational principle, the solution to the problem defined by equation 2-3 - 2-5 is equivalent to

$$F(\boldsymbol{E}) = \iint_2^1 [\mu_r^{-1}(\nabla \times \boldsymbol{E}) \cdot (\nabla \times \boldsymbol{E}) - k_0^2 \bar{\varepsilon_r}\boldsymbol{E} \cdot \boldsymbol{E}]d\Omega \tag{2-6}$$

To solve equation 2-6, the electric field in the computation domain is discretized using the triangular elements,

$$E_t^e = \sum_{i=1}^n e_{ti}^e N_i^e \text{ and } E_z^e = \sum_{i=1}^n e_{zi}^e \zeta_i^e \tag{2-7}$$

whereN_i^e (ζ_i^e) and e_{ti}^e denote the vector expansion functions and the corresponding expansion coefficients. The final discretization of the variational problem equation 2-6 amounts to a generalized eigenvalue problem

$$\begin{bmatrix} \mathbf{A}_{tt} & \mathbf{A}_{tz} \\ \mathbf{A}_{zt} & \mathbf{A}_{zz} \end{bmatrix} \begin{Bmatrix} e_t \\ e_z \end{Bmatrix} = k_0^2 \begin{bmatrix} \mathbf{B}_{tt} & \mathbf{B}_{tz} \\ \mathbf{B}_{zt} & \mathbf{B}_{zz} \end{bmatrix} \begin{Bmatrix} e_t \\ e_z \end{Bmatrix} \quad \text{2-8}$$

where A and B are complex matrices. Once the eigenvalues of equation 2-8 are solved, the eigen-wavelengths are calculated as $\lambda_r = 2\pi/k_0$.

CHAPTER 3. AN OPTOFLUIDIC METASURFACE FOR LATERAL FLOW-THROUGH DETECTION OF BREAST CANCER BIOMARKER

3.1 Abstract

The rapid growth of point-of-care tests demands for biosensors with high sensitivity and small size. This paper demonstrates an optofluidic metasurface that combines silicon-on-insulator (SOI) nanophotonics and nanofluidics to realize a high-performance, lateral flow-through biosensor. The metasurface is made of a periodic array of silicon nanoposts on an SOI substrate, and functionalized with specific receptor molecules. Bonding of a polydimethylsiloxane slab directly onto the surface results in an ultracompact biosensor, where analyte solutions are restricted to flow only in the space between the nanoposts. No flow exists above the nanoposts. This sensor design overcomes the issue with diffusion-limited detection of many other biosensors. The lateral flow-through feature, in conjunction with high-Q resonance modes associated with optical bound states of the metasurface, offers an improved sensitivity to subtle molecule-bonding induced changes in refractive index. The device exhibits a resonance mode around 1550 nm wavelength and provides an index sensitivity of 720 nm/RIU. Biosensing is conducted to detect the epidermal growth factor receptor 2 (*ErbB2*), a protein biomarker for early-stage breast cancer screening, by monitoring resonance wavelength shifts in response to specific analyte-ligand binding events at the metasurface. The limit of detection of the device is 0.7 ng mL^{-1} for *ErbB2*.

3.2 Introduction

Optical label-free biosensors can detect biomolecules based on their intrinsic physical properties, such as Raman scattering, refractive index, and second harmonic generation [105-108]. In particular, many refractive index-based biosensors have been implemented to study analyte-ligand interactions without using labels [109-111]. In contrast to binding assays that

require fluorescent or enzymatic tags, label-free assays often eliminate the need for time-consuming labeling processes and can monitor binding kinetics in real time [112-114]. Therefore, label-free biosensors are gaining increasing attention in the fields of life sciences, pharmaceutics, and clinic diagnosis [115-124]. Recently, optical resonators using surface plasmon resonance, photonic crystal, and whispering gallery mode [53, 125-129] have been extensively studied and exploited for label-free biosensors. Owing to their strong ability to confine resonating fields, these biosensors are sensitive to the presence of biomaterials immobilized in the close vicinity of their surfaces [130].

While significant progress has been made to develop optical label-free biosensors, how to efficiently delivery samples to the sensor surface remains challenging. To address the issue with the mass transfer limitation, microfluidic systems have been developed and applied to label-free biosensors [131, 132]. To improve the integration between the sensing and fluidic elements, several optofluidic biosensors (e.g., liquid-core ring resonators [133] and anti-resonant reflecting optical waveguides [134]) have been used to facilitate the transport of analyte. Both the microfluidic and optofluidic approaches rely on a flow-over scheme, where liquid samples flow through a channel, during which the analytes diffuse from the sample stream onto the surface of the biosensor [135-138]. Recently, a vertical flow-through sensor design was implemented to label-free optical biosensing, where liquid samples flow through a horizontally placed, nanopatterned dielectric or metallic diaphragm with nanoholes that functions as both the sensing element and conduits [44, 46, 48, 139]. This sensor has enhanced the interaction between the sensing surface and analytes, thus reducing detection time.

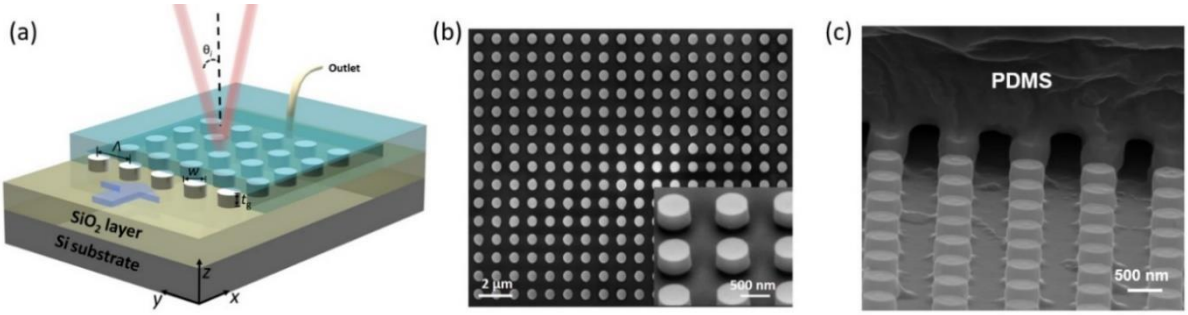

Figure 3-1 (a) Schematic illustration of the optofluidic metasurface with a 2D array of SNPs. (b) SEM image of the fabricated SNPs. The inset shows a perspective view of the SNPs. (c) SEM images of the nanofluidic channel where the SNPs are sandwiched between the buried oxide of an SOI substrate and a capped PDMS cover. A sample can laterally flow through the SNP region and be captured by the recognition biomolecules onto the metasurface.

This paper reports on a novel lateral flow-through biosensor, consisting of a metasurface with a two-dimensional (2D) periodic array of silicon nanoposts (SNPs), for the detection of cancer biomarker. The structure is manufactured in the thin top silicon layer of a silicon-on-insulator (SOI) substrate, coated with graphene oxide (GO) nanosheets, and biofunctionalized with specific antibody molecules. A polydimethylsiloxane (PDMS) slab with an inlet and an outlet is bonded to the top surface of the SNPs, thus restricting the flow of liquid analytes in between the PDMS and the buried oxide layer of the SOI substrate (Figure 3-1). It is worth noting that silicon or SOI-based metasurfaces have attracted increasing attention due to the flexibility in tuning of their optical properties [140-142], and the fabrication compatibility with complementary metal-oxide-semiconductor (CMOS) process. The high refractive index of silicon is favourable for light modulation [71, 143-146], e.g., to enhance optical fields. Our biosensor is featured with the lateral flow-through design for improved analyte-ligand interactions at the metasurface. Owing to a reduced diffusion length, the biosensor design will overcome the issue of mass transfer limit that occurs in

many existing label-free biosensors [147]. Therefore, the biosensor will have an improved sensitivity and a reduced assay time. In addition, the metasurface supports different optical resonance modes, such as the bound states in the continuum (BIC) mode, and leaky waveguide mode [97, 148, 149], to detect biomolecule absorptions. In this work, the guided mode resonance (GMR) mode, whose linewidth depends on the coupling angle, is utilized and exhibits a high sensitivity to a change in refractive index at the surface of SNPs. The sensor design emphasizes both analyte delivery and sensitivity. The key figure of merit of the device and its ability to detect cancer biomarkers are demonstrated.

3.3 **Experimental section**

3.3.1 Fabrication of the optofluidic metasurface

An SOI wafer is used to fabricate the SNPs. First, 200 nm-thick PMMA is coated onto the substrate at 2000 rpm for 45 sec. Subsequently, e-beam lithography is used to pattern the nanoholes array in the PMMA. Next, a 15 nm-thick Al_2O_3 layer is evaporated using electron-beam evaporation, and then patterned using lift-off process, to form a protection layer during the following deep reactive-ion etching of Si (Figure 3-1(b)). After the SNPs are formed, the Al_2O_3 layer is removed via wet chemical etching. The overall size of the device is 1×1 mm^2. To enable laterally flowing liquid analytes through the SNP area, a 2 mm-thick PDMS slab with the pre-drilled inlet and outlet is bonded directly onto the top surface of the SNPs via oxygen plasma treatment. Figure 3-1(c) shows the formed nanofluidic channels embedded with the SNPs.

3.3.2 Setup for optical reflection measurement

A tunable laser (ANDO, AQ4321) is used as a light source providing a wavelength range from 1520 nm and 1620 nm with a central wavelength of 1570 nm. The light is collimated and incident onto the metasurface through a 50/50 beam splitter cube. The

biosensor is mounted on a rotation stage to adjust the angle of incidence. The reflection spectrum is measured in real time using an InGaAs photodetector synchronized through an oscilloscope.

3.3.3 ErbB2 detection assay

The biosensor is used to quantify a well-established breast cancer biomarker, *ErbB2* [150]. The biofunctionalization of the surface begins with introducing an intermediate layer of GO to the surface. The GO layer allows enhancing the loading capability of *anti-ErbB2* molecules. In this step, the metasurface is treated with oxygen plasma for 50 sec to make the SNPs hydrophilic. Next, a well-dispersed solution of single-layer GO nanosheets (0.4 mg mL^{-1}) is prepared in DI water, followed by thorough sonication for 1 hr. 50 μL of this solution is drop-cast onto the metasurface and then dried at room temperature (25 °C) for 2 hr. 20 µL of PBS (pH = 7.4) solution containing *anti-ErbB2* molecules (0.24 µM) is drop-cast onto the GO-coated metasurface, followed by treating a mixed solution of EDC (1-ethyl-3-(3-dimethylaminopropyl) carbodiimide hydrochloride, 0.2 M) and NHS (N-hydroxysuccinimide, 0.05 M) at a 1:1 ratio [151]. The abundant oxygenated groups such as -COOH and -CHO at GO are activated and utilized to make covalent binding with *anti-ErbB2* using the EDC-NHS coupling chemistry [150, 152]. To immobilize antibody molecules, the metasurface is kept in a humidity chamber for 12 hr, and then is washed with PBS to remove unbound antibody molecules. The resulting primary amine groups present at *anti-ErbB2* bind with carboxyl groups at GO to form strong CH-NH amide bonds. Finally, 2.0 mg/mL of bovine serum albumin molecules is used to block non-specific sites of anti-*ErbB2* on the metasurface.

3.4 **Results and Discussion**

3.4.1 Nanophotonic and nanofluidic simulations

The SNP array (350 nm thickness) is designed on the top of a 3 μm-thick oxide layer to provide an optical resonance around 1550 nm wavelength. The silicon device layer is transparent around this wavelength and has a negligible extinction coefficient $\kappa < 0.001$ and a large refractive index $n = 3.477$. The geometric parameters of the SNPs include the array period (Λ), nanopost width (w), device layer thickness (t_g), and duty cycle ($\eta = w/\Lambda$). The basic principle of the SNPs and corresponding optical characteristics have been discussed in our previous work [148]. The SNPs exhibit a BIC mode and a GMR mode, depending on the angle of incidence. As illustrated in Figure 3-1(a), the angle of incidence is defined in terms of a standard spherical coordinate system, with the polar angle θ_i being measured from the z-axis. Because of the symmetry, the optical responses of the device are polarization-independent when $\theta_i = 0$.

Rigorous coupled wave analysis (RCWA) is used to study optical resonances and evaluate their performances for detecting biomolecules (Figure 3-2). The details of the RCWA simulation method are described in Supplementary Information. Figure 3-2(a) presents the obtained photonic band diagram of the SNPs obtained by plotting the calculated reflection spectra as a function of θ_i. The wavelength and the incident angle change from 1450 nm to 1650 nm, and from -15° to 15°, respectively. The region indicated by the black box (Figure 3-2(a)) contains a BIC mode, which appears at $\lambda_r = 1536$ nm and $\theta_i = 0$. For the angles near the BIC mode, the strong reflection regions accommodate high-sensitivity resonance features. Figure 3-2(b) compares the simulated reflection spectra for $\theta_i = 0°$, 1°, 2°, 3°, and 4°. Since the characteristics of these two modes are similar to the transverse magnetic (TM)-polarized modes of the one-dimensional grating based metasurface demonstrated

previously [148], these modes can be named TM-like resonance modes. The obtained resonant linewidth decreases as the incidence angle approaches 0°. For example, the resonance linewidth at θ_i = 4° is found to be 30 nm, corresponding to a Q-factor of 52. In comparison, the Q-factor significantly increases to 900 when θ_i is reduced to 1°. The vanishing of the linewidth at θ_i = 0° implies the existence of BIC.

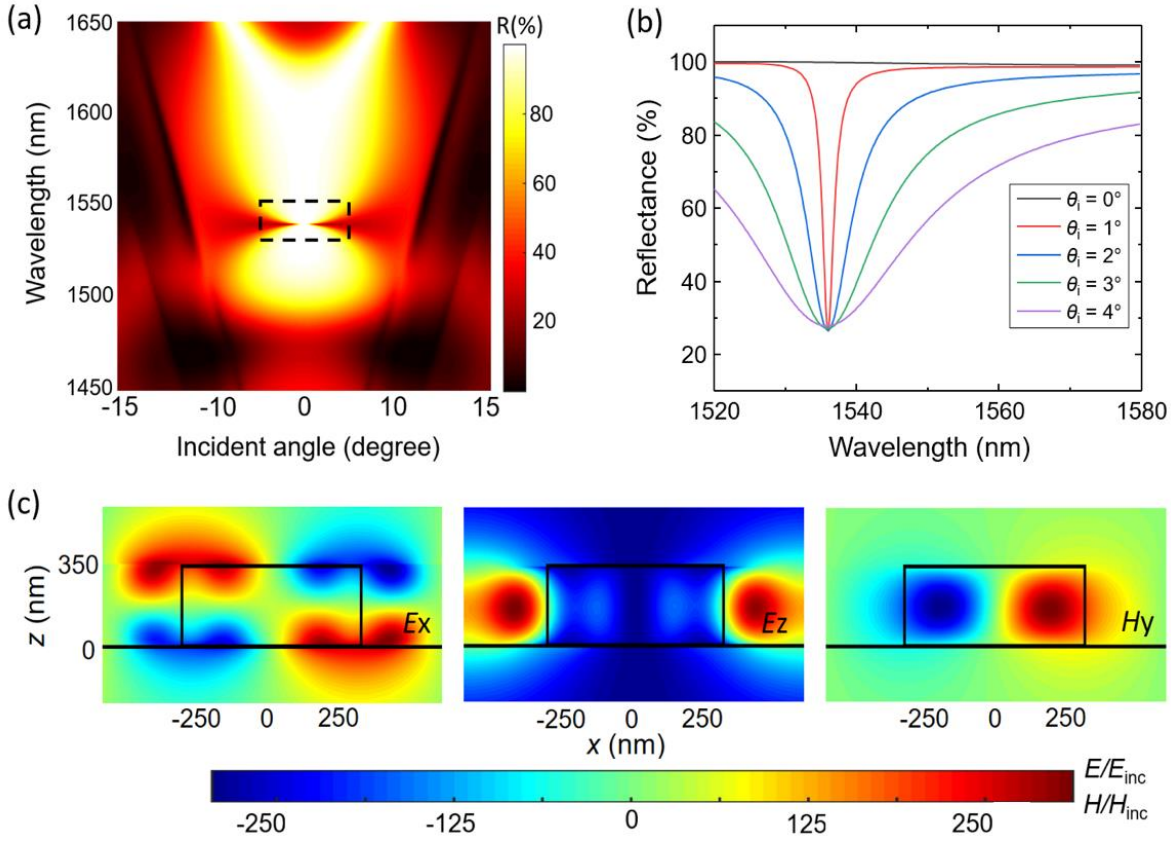

Figure 3-2 Simulated optical characteristics of the 2D array of SNPs. a) Calculated reflection spectra over the wavelength range 1450 to 1650 nm, incident angle (θ_i) in the range of -15° to 15°. The region indicated by the black box contains a one BIC mode appears at λ_r = 1536 nm at θ_i = 0. b) Calculated reflection spectra calculated for θ_i = 0°, 1°, 2°, 3°, 4°, and 5°. c) Near-field distributions of the E_x, E_z, and H_y components when λ_r = 1536 nm and θ_i = 1°

The near-field distributions of the resonance mode in the *xz*-plane (Figure 3-1) are calculated using the RCWA method (Figure 3-2(c)). The distributions of the E_x, E_z, and H_y components are associated with the resonance (Q-factor = 900) at λ_r = 1536 nm and θ_i = 1°.

The colour scale represents the amplitudes of the electric and magnetic fields normalized to the amplitude of the incident field. As seen from the field distributions, the maximum field enhancement factor is as high as 300. The enhancement factor of the field intensity is calculated by averaging the electric field intensities within the sensor area ($-\Lambda/2 < x < \Lambda/2$ and $0 < z < 350$ nm). As a result, the averaged enhancement factor of the field strength (intensity or amplitude) is ~2.7 x 10^5. The distributions of the tangential components (E_x and H_y) appear asymmetric. The mode can be excited because of the asymmetric nature of the incident wave at $\theta_i = 1°$. Figure 3-3(a) shows the normalized near-field distribution of E_x in the *xy*-plane at the center of SNPs ($z = 175$ nm). The plot shows five periods of the SNPs along both the *x*- and *y*- directions.

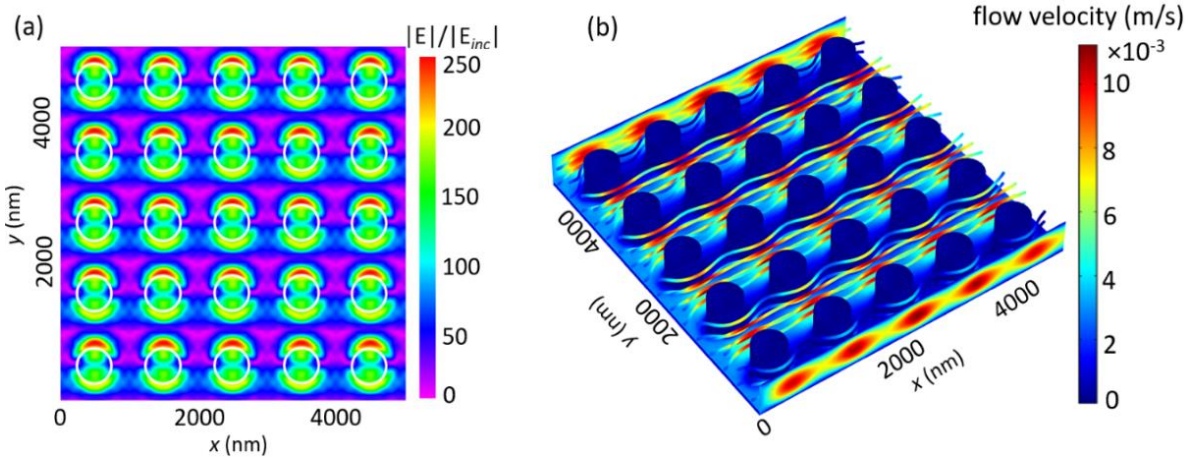

Figure 3-3 (a) Calculated near-field distribution of Ex for five periods of the SNPs in the x-y plane. (b) Simulated distribution of flow rate when the liquid sample passes through the lateral flow-through biosensor.

Fluid dynamics simulations are carried out to illustrate the flowing of an aqueous sample through the SNP area (see the details in Supplementary Information). Figure 3-3(b) displays the flow velocity distribution at the steady state. The sample solution is infused into the channel from the inlet (left boundary) and exits from the outlet (right boundary). The

analytes in the sample are not only brought to the sensor surface by the steams, but also diffuse to the sensor surface for the analyte-ligand interactions. To ensure high output signals, we chose the optical resonance, at which the localized optical field (Figure 3-3(a)) well overlaps with the region of analyte absorption. As shown in the following section, the biosensor is characterized at θ_i = 1° to obtain an optimized response.

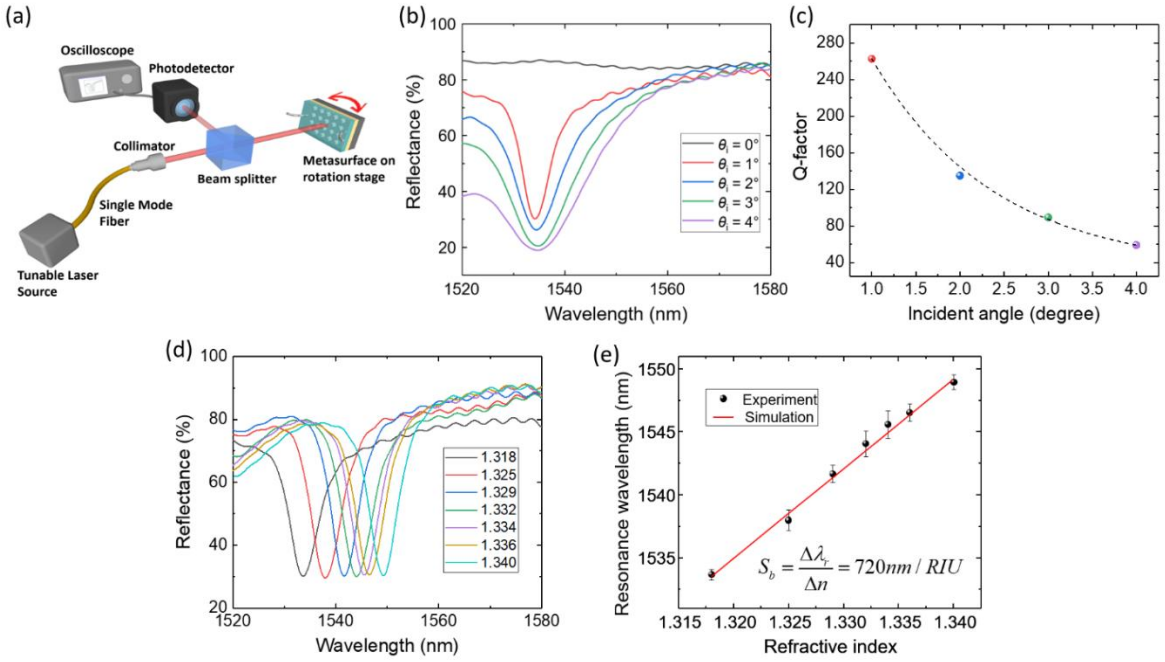

Figure 3-4 (a) Schematic diagram of the reflection measurement setup (b) Measured reflection spectra of the biosensor at five different angles of incidence. (c) Q-factor of the resonances as a function of θ_i. The data is fitted to demonstrate the exponential decrease of the Q-factor when θ_i. increased from 0° to 4° (d) Reflection spectra of the device with the sample surface immersed in DI water and solutions of ethanol-water mixtures. The spectra were measured at θ_i. = 1°. (e) Simulation (red line) and experiment (black dots) results of the resonance wavelength as a function of the refractive index.

3.4.2 Characterization of metasurface

3.4.2.1 Optical characterization

The fabricated metasurface was characterized by measuring the reflectance from the metasurface using the setup shown in Figure 3-4(a). The reflection at a specific angle of incidence was measured in the near infrared range. A tunable laser, whose emission

wavelength ranging from 1520 nm to 1620 nm, was used as the excitation. The reflected laser beam was measured using an InGaAs photodetector.

Figure 3-4(b) compares the measured reflection spectra when θ_i = 0°, 1°, 2°, 3°, and 4°. The black curve represents the reflectance at θ_i = 0° where the BIC mode resides. Because the BIC mode is completely bound, there is no signature of resonance in the spectrum. When θ_i increases, the optical resonances appear as the narrowband dips in the reflection spectra. At θ_i = 1°, the BIC mode turns into a radiative resonance at λ_r = 1534 nm with a linewidth of $\delta\lambda_r$ = 5.8 nm. Further increasing θ_i from 1° to 4° results in a significant increase of the resonance linewidth, while the resonance wavelength remains near λ_r = 1537.2 nm. The measured spectra agree well with the simulated results (Figure 3-2(b)). To illustrate how to tune the resonance strength by changing θ_i, the Q-factor is plotted as a function of θ_i (Figure 3-4(c)). The Q-factor decreases exponentially from 270 to 57 with increasing θ_i from 1° to 4°. It is worth noting that the resonance features a flat angular dispersion, which can be exploited to realize refractive index-based sensing with a focused excitation.

3.4.2.2 Refractometric sensing

Figure 3-4(d) compares the measured reflection spectra when the metasurface is covered with different index solutions. The solutions are prepared by mixing deionized (DI) water and ethanol at different ratios of 1:2, 4:5, 1:1, 4:3, 2:1, 4:1, and 1:0, to produce the refractive indices of n = 1.340, 1.336, 1.334, 1.332, 1.329, 1.325, and 1.318, respectively. The black curve in Figure 3-4(d) shows the case when the channel is filled with DI water (n = 1.318). The resonance dips are found to shift toward longer wavelengths with increasing the value of n. These reflection spectra are measured, all at θ_i = 1°. To calculate the index

sensitivity (S_b), the resonance wavelength of the device is plotted as a function of surrounding refractive index (Figure 3-4(e)). The resonance wavelengths are found by fitting the data in the vicinity of minimal reflection using a 2nd order polynomial function. The slope of the linear fit in Figure 3-4(e) is calculated as the index sensitivity $S_b = \Delta\lambda_r/\Delta n$ = 720 nm/RIU.

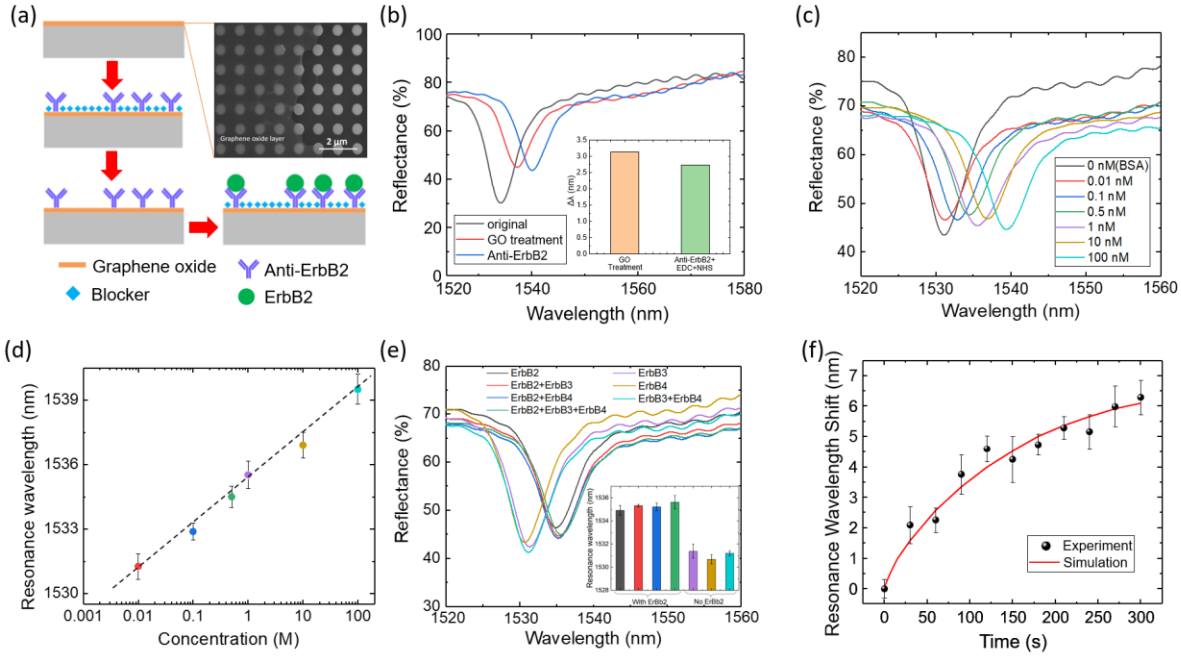

Figure 3-5 (a) Schematics of the label-free assay and SEM of the SNPs with (left half) and without (right half) the GO coating. (b) Reflection spectra of the bare sensor, GO layer, and anti-*ErbB2* antibody coating. Inset: $\Delta\lambda_r$ after each step of the surface functionalization. (c) Reflection spectra measured in the present of *ErbB2* at a series of concentrations ranging from 0.01 to 100nM. (d) Dose response curve for the detection of *ErbB2* by plotting the resonance wavelength as a function of the *ErbB2* concentration. (e) Reflection spectra measured for seven different combinations of *ErbB2*, *ErbB3*, and *ErbB4* antigens. Inset: sensor outputs in the presence of interfering molecules. (f)Simulation (red) and experiment (black) results of the kinetic binding of *ErbB2* and anti-*ErbB2* antibody.

3.4.3 Detection of breast cancer biomarker

The SNP-based biosensor can be utilized to detect biomolecules, such as DNA, protein, or small molecules, in real time. As an example, the device is used to quantify a

well-established breast cancer biomarker, *ErbB2*. As a label-free technology, the SNP-based biosensor measures the refractive index change caused by the immobilization of the *ErbB2* molecules. The target *ErbB2* molecules are captured by the anti-*ErbB2* antibodies on the sensor surface. The details of this label-free assay are described in the Experimental section. Figure 3-5(a) summarizes the major assay steps, including subsequent deposition of GO, anti-*ErbB2* antibody, and blocker, and the detection of *ErbB2* antigen. The SEM image in Figure 3-5(a) show the SNPs with and without the GO coating. The thickness of the GO layer is about 30 nm. Figure 3-5(b) presents the measured reflection spectra of the device when the SNPs is bared (black), coated with a GO layer (red), and functionalized with anti-*ErbB2* molecules.

Figure 3-5(c) shows the reflectance spectra recorded when the samples containing *ErbB2* are injected into the nanofluidic channel. The sample solution is prepared by dissolved *ErbB2* in a phosphate-buffered saline (PBS; pH = 7.4) solution at six concentrations (0.01 nM, 0.1 nM, 0.5nM, 1 nM, 10 nM, and 100nM). As the concentration of *ErbB2* increases, the resonance dip in the reflection spectrum red shifts to longer wavelengths. The total shift of the resonance wavelength is approximately 6 nm when the *ErbB2* concentration increases from 0.01 nM to 100 nM. The dose response for the detection of *ErbB2* biomarker is shown in Figure 3-5(d). The experiment with a specific *ErbB2* concentration repeats five times and the error bars represent the standard deviation of resonance wavelength for each concentration. The sensitivity of optical sensors can be estimated using $S_s = \Delta\lambda_r / \Delta c$, where Δc is the corresponding concentration difference. The SNP-based biosensor exhibits a sensitivity of 2 nm/nM for *ErbB2*.

Table 1 compares the key performance of this biosensor with some recently reported label-free biosensors for the detection of *ErbB2* [112, 113, 153-156]. With regards to the sensitivity, the SNP-based biosensor outperforms the reported ring resonator biosensor (S_s = 0.12 nm/nM) and distributed feedback grating ($S_s = 2x10^{-3}$ nm/nM) biosensor [153, 154]. The limit of detection (LOD) of the SNP-based biosensor is found to be 0.7 ng mL^{-1} using the 3*s* criterion (expressed in concentration units), where *s* represents the standard deviation of five-time measurements for the PBS solution. Compared to the other two optical biosensors, the SNP-based biosensor provides a lower LOD. In addition to the high refractive index sensitivity of the metasurface, the lateral flow-through design contributes significantly to the increased sensitivity and the lowered LOD by offering a useful platform for realizing the syngeneic interaction between minute amounts of *ErbB2* proteins available in the sample and the capture molecules on the surface of SNPs. Although some of the reported electrochemical biosensors exhibit lower LOD values, our device presents a wider dynamic range.

Table 1 Performance comparison of the lateral flow-through biosensor with other devices for the detection of *ErbB2*

Device	Detection type/mode	Sensitivity	Detection range (nM)	Limit of detection (ng mL^{-1})
Optofluidic silicon metasurface	Guided mode resonance	2 nm nM^{-1}	0.01 – 10	0.7
Optofluidic ring resonator	Whispering gallery mode	0.12 nm nM^{-1}	0.14 – 3.45	13
1D distributed feedback grating	1st-order diffraction mode	2×10^{-3} nm nM^{-1}	0.028 – 138	14
Hydrazine-Au nanoparticle-aptamer bioconjugate	Electrochemical	15×10^{-3} μA nM^{-1}	$1x10^{-6}$ – 1.381	37
Sandwich magnetoimmunosensor	Electrochemical	1.4×10^{-4} μA nM^{-1}	$1.4x10^{-3}$ – 0.4	0.026
Capacitance based aptasensor	Electrochemical	1.7×10^{-3} pF nM^{-1}	$2.7 x10^{-3}$ – $2.7 x10^{-2}$	0.2

To study the selectivity of the label-free biomarker detection assay, samples containing *ErbB2*, *ErbB3,* and *ErbB4* antigens were measured using the anti-*ErbB2* antibody-coated metasurface. These antigens belong to the *ErbB* receptor tyrosine kinase family, but the *ErbB3* and *ErbB4* antigens are nonspecific to the anti-*ErbB2* antibody[152]. Figure 3-5(e) shows the measured reflection spectra of seven samples with different combinations of *ErbB2*, *ErbB3,* and *ErbB4* antigens (1nM). The inset of Figure 3-5(e) summarizes the resonance wavelength measured for these samples. The samples with the *ErbB2* antigen and interfering molecules result in a resonance wavelength shift of 6 nm. In contrast, the samples without *ErbB2* molecules show very small shift (<1 nm) of the resonance wavelength. The results indicate that the SNP-based biosensor is selective to the target *ErbB2* antigen when the SNPs is functionalized using the anti-*ErbB2* antibody. As a label-free detection method, the biosensor can monitor the analyte-ligand binding process in real time. In this experiment, the reflection spectra were recorded when the *ErbB2* bound to the *ErbB2* antibody-coated sensor surface. Figure 3-5(f) shows the temporal change of the resonance wavelength when the *ErbB2* sample (0.01 nM) passes through at a flow rate of 0.3 μL/min. The simulated and experimental results for *ErbB2* and anti-*ErbB2* binding are compared in Figure 3-5(f). The error bars show the standard deviation of resonance wavelength shift for three replicated tests. The simulation of the binding process is performed using a finite element method (FEM) model that includes the fluid dynamics of the sample inside the nanofluidic channel, the diffusion of analyte from the solution to the sensor surface, and the surface reaction process. The details of the simulation are described in the Experiment section. The binding of the *ErbB2* to the surface results in an increase of λ_r around 6 nm.

3.5 **Conclusion**

In summary, this paper demonstrates a label-free, lateral flow-through biosensor that combines both biomolecule detection and sample delivery functions using the SOI-based metasurface. The SNPs provide numerous nanoscale flow channels to facilitate rapid delivery of analyte to the sensor surface. The device utilizes the GMR mode of the metasurface and operates in the telecom optical wavelength band. The linewidth of the resonance is tuned by changing the angle of incidence. The biosensor exhibits the refractive index sensitivity of 720 nm/RIU. The biosensor is studied for its ability to detect the *ErbB2* breast cancer biomarker. Because the SNP-based biosensor can be fabricated using the CMOS-compatible process, the device is amendable to integration with a wide variety of lab-on-a-chip components. We envision that the biosensor will enable rapid and quantitative analysis in point-of-care applications, such as disease diagnosis, drug test, and pathogen detection.

3.6 **Supplementary information**

3.6.1 Electromagnetic modeling

Optical simulations are carried out using a commercial Rigorous coupled wave analysis (RCWA) software package (DiffractMOD, Synopsis). The simulation is set up to analyze a unit volume of the metasurface, where periodic boundary conditions are applied to define the calculation domain. Ten harmonics are used to expand the permittivity and fields along the *x*-direction. The dispersive and complex refractive indices of crystalline silicon, $n(\lambda) = n_{si}(\lambda) + i\kappa_{si}(\lambda)$, where $n_{si} = 3.486 + i0.001$ at $\lambda = 1550$ nm. The reflection and transmission spectra are calculated in the near-infrared wavelength range.

3.6.2 Fluid dynamic simulation

Finite element method (FEM) is used to simulate how molecules in the bulk solution transported to the sensor surface and react with the capture molecules. This dynamic process

includes laminar flow transport, diffusion of diluted specious, and surface reaction. Stationary laminar flow with no-slip boundary condition and periodic flow condition are used in the model. The Navier-Stokes equation governs the motion of fluidics and can be seen as Newton's second law of motion for fluids:

$$\boldsymbol{\rho}\left(\frac{\partial \vec{\boldsymbol{u}}}{\partial \boldsymbol{t}} + \vec{\boldsymbol{u}} \cdot \boldsymbol{\nabla}\vec{\boldsymbol{u}}\right) = -\boldsymbol{\nabla p} + \boldsymbol{\nabla} \cdot \left(\boldsymbol{\mu}\left(\boldsymbol{\nabla}\vec{\boldsymbol{u}} + (\boldsymbol{\nabla}\vec{\boldsymbol{u}})^{\boldsymbol{T}}\right) - \frac{\mathbf{2}}{\mathbf{3}}\boldsymbol{\mu}(\boldsymbol{\nabla} \cdot \vec{\boldsymbol{u}})\boldsymbol{I}\right) + \boldsymbol{F} \quad 3\text{-}1$$

where $\vec{u}$is the fluid velocity, $p$is the fluid pressure, $\rho$is the fluid density, and $\mu$is the fluid dynamic viscosity. At the sensor surface, the kinetic sensor response as analyte molecules in the bulk solution is transported and diffused to bind with the capture molecules. The governing differential equation used for the analyte concentration in the bulk solution is the convection-diffusion equation listed below as

$$\frac{\partial c_A}{\partial t} + \nabla \cdot (-D\nabla c_A + c\vec{u}) = 0 \quad 3\text{-}2$$

where c_A, D, and $\vec{u}$ are the bulk analyte concentration, the bulk diffusion constant, and fluid flow velocity vector, respectively. At the sensor surface, the boundary condition is represented by coupling of the rate of reaction at the surface with the flux of the reacting species and the concentration of the adsorbed species and bulk species as

$$N = k_a c_A(\theta_0 - c_{AB}) - k_d c_{AB} \quad 3\text{-}3$$

where N is the adsorption and desorption of analyte at the reactive surfaces give rise to a net flux represented as $\vec{n} \cdot (-D\nabla c_A + c\vec{u})$. At the inlet of the channel where analyte solution is introduced, the boundary condition used here is $c = c_0$.

3.7 **Acknowledgements**

This work was supported by the United States National Science Foundation under Grant Nos. ECCS 17-11839 and ECCS 16-53673. The authors thank the Nano Fabrication Centre at the University of Minnesota for the support of device fabrication.

CHAPTER 4. RAPID DIFFERENTIATION OF HOST AND PARASITIC EXOSOME VESICLES USING MICROFLUIDIC PHOTONIC CRYSTAL BIOSENSOR

4.1 **Abstract**

Parasite extracellular vesicles (EVs) are potential biomarkers that could be exploited for the diagnosis of infectious disease. This paper reports a rapid bioassay to discriminate parasite and host EVs. The EV detection assay utilizes a label-free photonic crystal (PC) biosensor to detect the EVs using a host-specific transmembrane protein (CD63), which is present on EV secreted by host cells (modeled by murine macrophage cell line J774A.1) but is not expressed on EV secreted by parasitic nematodes such as the gastrointestinal nematode *Ascaris suum*. The surface of PC is functionalized to recognize CD63, and is sensitive to the changes in refractive index caused by the immobilization of EVs. The biosensor demonstrates a detection limit of 2.18×10^9 EVs/mL and a capability to characterize the affinity constants of antibody-host EV bindings. The discrimination of murine host EVs from parasite EVs indicates the capability of the sensor to differentiate EVs from different origins. The label-free, rapid EV assay could be used to detection parasite infection and facilitate the exosome-based clinic diagnosis and exosome research.

4.2 **Introduction**

Recently, membranous extracellular vesicles (EVs), including nanoscale exosomes and other vesicles derived from cancer cells, have also been found in the blood of cancer patients[157-159]. These membrane-bound phospholipid nanovesicles are actively secreted by both prokaryotic and eukaryotic cells, including mammalian cells and pathogens like parasitic helminths[160-162]. EVs secreted from helminths contain effector molecules such as functional proteins and small RNAs, and as with other systems. There is emerging

evidence demonstrating that EVs released from helminths could traffic within the host's body fluid and interact with the immune system to modulate the host immune response[163-165]. EVs have also been considered as an important mediator of the cell to cell communication; because of the membrane-based structure, they are more stable than proteins and nucleotides biomarkers that are secreted alone, which arouses the potential of using EVs to diagnose infectious diseases and other human diseases like cancer.

Rapid, multiplexed exosome analysis can be used to detect minute amounts of various biomarkers for diseases that are currently difficult to diagnose and monitor such as cancer, infectious, autoimmune and degenerative diseases. Fluorescence-based approaches, such as bead-based assays, have the multiplexing capability and high sensitivity but require excessive volumes of serum[166, 167]. Compare to conventional methods based on immunoblotting or enzyme-linked immunosorbent assay (ELISA) assays[168-171], the PC-based label-free assay eliminates the labeling step. The outputs of PC-based devices can be measured in real time and the assay time can be significant reduced[25, 109, 172-174]. Recently, several biosensors have been reported for the analysis of exosomes[111, 175-180], using surface plasmonic resonance[111], nuclear magnetic resonance[179], and electrochemical aptasensor[180].

The paper reports the discrimination of EVs derived from murine macrophages and parasites using a photonic crystal (PC) biosensor. The PC biosensor, consisting of a sub-wavelength grating, is essentially a narrowband optical reflector that reflects a particular wavelength of a broadband excitation. The capture of EVs on the biosensor increases the refractive index on the sensor surface and results in a change in the light reflectance of the PC. Using the PC biosensor, we have developed a label-free binding assay to detect EVs

according to their membrane-specific proteins, and distinguish EVs secreted by a murine macrophage cell line (J774A.1) and a parasitic nematode (*Ascaris suum*). In addition, the developed assay can measure the binding of EV to its ligand in real time, thus enabling characterization of the EV-antibody binding affinity.

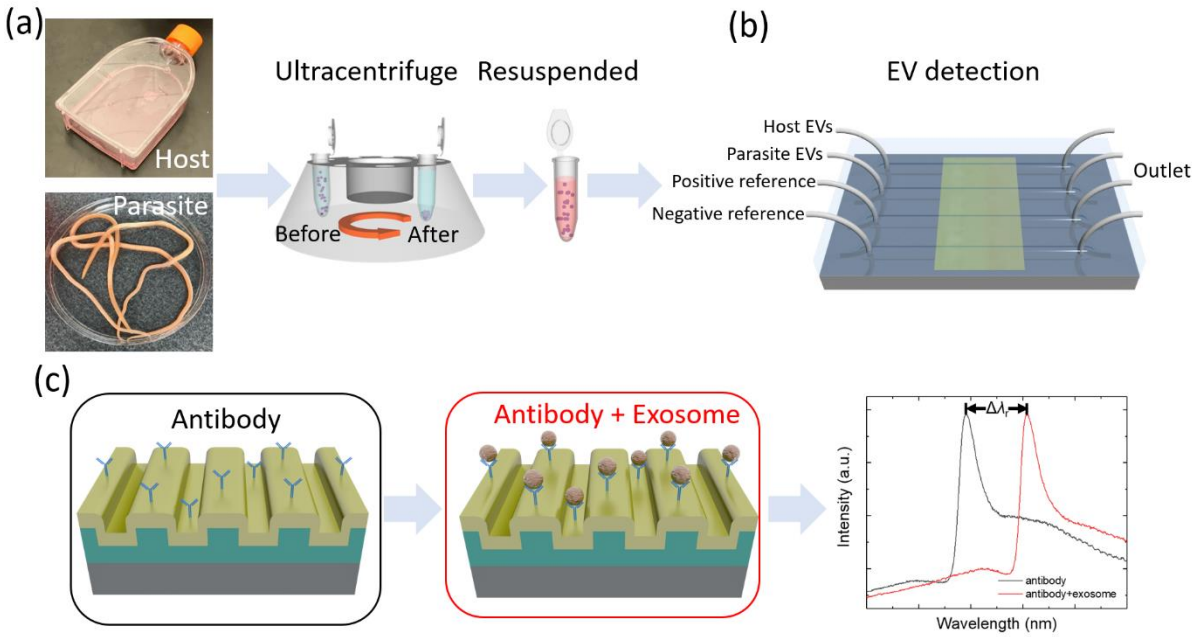

Figure 4-1 (a) Schematic diagram of the extraction of EVs from culture media. The EVs samples are centrifuged and re-suspended before being flowed into the microfluidic chip. (b) Illustration of the microfluidic PC biosensor chip. Four channels are designed for the host, parasitic, positive, and negative reference samples respectively. (c) Schematic structure of the PC grating and the label-free detection mechanism. The PC surface functionalized with the antibody (black box) exhibits resonant reflection (black curve in the reflection spectra). The binding of EVs to the antibody (red box) shift the narrowband reflection by a spectral shift of $\Delta\lambda_r$.

4.3 **Experimental section**

4.3.1 Preparation of host and parasite EV samples

The host and parasite EVs were isolated from spent murine macrophage and parasitic nematode culture media, respectively. Murine macrophage cell line (J774A.1) were cultured in DMEM containing 10% FBS (Thermo Fisher Scientific, Waltham, MA), 100 Units of

penicillin (Thermo Fisher Scientific, Waltham, MA), 100 μg/ml of streptomycin (Thermo Fisher Scientific, Waltham, MA), and 2 mM L-glutamine (Sigma-Aldrich, St. Louis, MO). Female adult *Ascaris suum* were collected from a local abattoir and maintained in *Ascaris* Ringer's solution at 37°C. Culture media was collected after 24 hr and filtered using 0.22-μm syringe filters (Millipore Sigma, Burlington, MA) to remove debris then EV were purified by differential centrifugation as previously described[161]; The EV pellets were re-suspended in 100-μL PBS solution and stored in a -80 °C freezer. The presence of EVs in these isolated preparations was confirmed using Nanoparticle Tracking Analysis (NanoSight LM10, Malvern Instruments, Malvern, UK). Figure 4-1(a) illustrates the process of preparing membranous extracellular vesicles, including nanoscale exosomes. The details of the materials and supplies are given in the supporting information.

4.3.2 PC biosensors embedded in microfluidic channels

The PC biosensor used in this study consists of a one-dimensional (1D) grating substrate, which is coated with a high-refractive-index thin film as shown in Figure 4-1(b). The high-refractive-index thin film acts as a light confinement layer and supports the resonance modes that are evanescently confined to the PC surface. The grating modulation allows the phase matching of excitation light to the PC resonances and results in the narrowband reflection[181].

The PC biosensors can detect chemicals and biomolecules via the biochemical interactions occurred on their surfaces. The adsorbed molecules on the sensor surface cause a change in the effective refractive index, which shifts the peak in the reflectance. The amount of spectral shift is proportional to the concentration of the target molecule as shown in Figure 4-1(c). Since its early demonstration[182], the PC biosensor has gained significant attentions

and been utilized for the analysis of various biomaterials, such as pathogens, DNA, proteins, enzymes, cells, and toxins[182-185].

The details of the PC fabrication and readout instrument are described in the supporting information. In brief, the sub-micron grating structure of the PC biosensor was fabricated inexpensively using the nano-replica molding method[186]. The molding silicon stamp (LightSmyth Technologies, Eugene, OR) carries a 1D grating with a period of 555.5 nm. The grating pattern was replicated on the surface of glass coverslip using UV curable epoxy (Norland Products, Cranbury, NJ). A titanium-oxide (TiO_2) was deposited on the replicated grating. To facilitate the detection of EVs, the fabricated PC structures were incorporated with microfluidic channels as shown in Figure 4-1(b). Four microfluidics channels were created, and each channel contained the PC grating (0.5 mm × 4 mm) in the middle. A broadband white light (Ocean Optics, Largo, FL) was used as the excitation and the light reflected off the PC grating was analyzed using a compact spectrometer (Ocean Optics, Largo, FL)[187]. The measured reflection spectra were analyzed to find the peak reflection wavelength (λ_r). The optical readout system was positioned below the microfluidic chip and aligned to the PC regions one at a time.

Before the sensors are used for the EV analysis, we functionalized the sensor surface using the EV specific antibody. The PC biosensor with the antibody coating is illustrated in the Figure 4-1(b). When the EVs bind to the antibodies (red box in Figure 4-1(b)), the reflection peak wavelength will redshift (Figure 4-1(c)) and the amount of wavelength shift ($\Delta\lambda_r$) will correspond to the concentration of EVs.

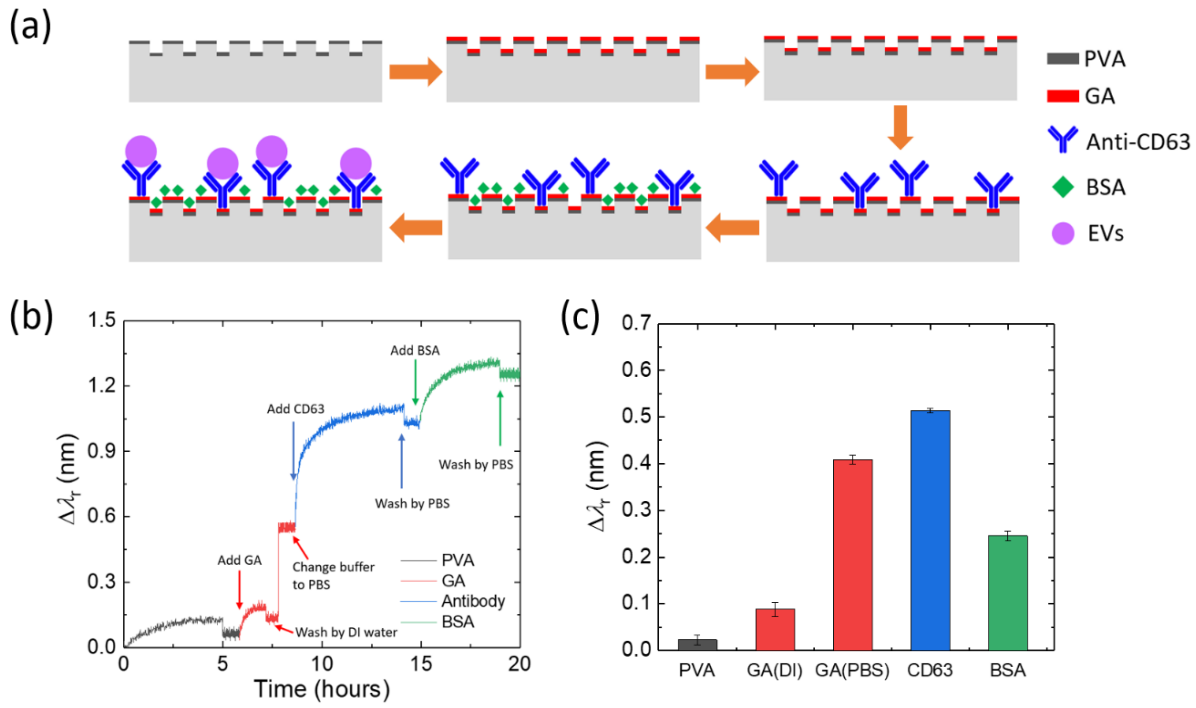

Figure 4-2 (a) Flow chart for the functionalization of the PC biosensor. (b) Measured wavelength shift as a function of time during the functionalization process. The black, red, blue, and green portions of the curve denote the PVA, GA, antibody, and BSA coating. (c) Resonant wavelength shift of the sensor after each step of the real-time measurement shown in (b).

4.4 **Results and discussion**

4.4.1 Surface functionalization for the PC biosensor

Before the PC biosensor was used for the analysis of EVs, we functionalized the sensor surface using a four-step process[188]. Figure 4-2(a) summarizes the major steps of the functionalization process (see details in the supporting information). During the process, the resonant wavelength shift was recorded every two seconds and plotted in Figure 4-2(b). The initial step (black line in Figure 4-2(b)) was the coating of a porous polymer layer (Polyvinylamine, PVA) that can provide a high-density amine group. The PVA coating process lasted 5 hours and was followed by a wash using DI water. Then, a bifunctional linker, glutaraldehyde (GA), was pumped into the channels. After 1.5 hours incubation (red line in Figure 4-2(b)), the channels were washed using DI water. Before the solution of

capture antibody, anti-CD63, was introduced into the channels, the buffer solution was changed to the PBS (pH = 7.4) and the resonance wavelength was measured. The anti-CD63 solution (0.1 mg/mL) was incubated inside the channels for overnight and then washed using the PBS solution. The final step was using the bovine serum albumin (BSA) solution (0.5% in 0.85% sodium chloride) to block the unoccupied aldehyde groups on the GA layer for four hours. The results of the anti-CD63 coating and BSA blocking are shown in Figure 4-2(b) as the blue and green portions, respectively. After the BSA blocking, the biosensors wereready for the analysis of EVs. The 4-steps functionalization process took less than 20 hours, which can be future optimized.

Figure 4-2(c) summarizes the resonant wavelength shift after each step of the process based on the real-time measurement shown in Figure 4-2(b). The first two columns in Figure 4-2(c) represent the sensor signals after PVA and GA coatings. The wavelength shifts are approximately $\Delta\lambda_r$ = 0.15 nm and 0.2 nm, respectively. The third column shows ~0.4 nm wavelength shift owing to the change of buffer from DI water to PBS. The absorption of the anti-CD63 and BSA blocker results in $\Delta\lambda_r$ = ~0.5 nm and ~0.25 nm, respectively. The measured resonance wavelength shift for each step was calculated based on the previous step. In each column, the error bar was the standard deviation calculated using nine independent measurements from nine PC sensors.

4.4.2 Detection of EVs secreted by murine macrophages

As a label-free detection approach, the PC biosensor can monitor the analyte-ligand binding process by recording the sensor output in real time. The host EVs were extracted from the murine macrophage cell culture and prepared to obtain a concentration of 2×10^{11} EVs/mL. Figure 4-3(a) shows the sensor output over time when the host and parasite EV solution was flowed through the microfluidic channel at a flow rate 30 µL/min. The

reflection spectrum was measured every two seconds and the $\Delta\lambda_r$ values were calculated. After 180 minutes, the ligand-analyte binding reached an equilibrium. Then, we washed the channels using PBS to remove the unbounded EVs and let the binding process enter the dissociate phase. After the PBS wash, the EVs binding results in a $\Delta\lambda_r$ of approximately 0.7nm. The positive and negative reference experiments were tested using the biosensor. For the positive reference experiment, the GA-coated PC biosensors were used to capture EVs without targeting a specific membrane protein. The positive reference experiment exhibited an output of $\Delta\lambda_r$ = 1.8 nm. In contrast, the negative reference experiments were carried out on the BSA-blocked PC surface without anti-CD63 antibody. The sensor output is nearly zero for the negative reference experiment. The details of the reference experimental processes are given in supporting information. As shown in the sensorgrams in Fig 3(a), the label-free signals still slowly increase at the saturation region. According to the pervious study[189] on the label-free sensorgrams, our dynamic response curves in Figure 4-3(a) include both the binding reaction and the EV diffusion processes. To identify the limit of detection (LOD), we measured host EV samples at a dilution serial of six concentrations ranging from 2×10^9 EVs/mL to 2×10^{11} EVs/mL. The samples were diluted consecutively by a factor of two in PBS. Figure 4-3(b) shows the dose-response curve, $\Delta\lambda_r$ versus EV concentration, in logarithmic scale. At 2×10^{11} EVs/mL, the sensor output starts to saturate with $\Delta\lambda_r$ = 0.7 nm. The dose-response data was fitted with a sigmoidal curve (the red line in Figure 4-3(b)) with a reduced chi-squared (R^2) value of 0.854. The error bar in the dose-response curve represents the standard deviation (σ) of $\Delta\lambda_r$ measured using nine different PC biosensors. The LOD of this sensor was calculated by the summation of the noise signal arising from the negative reference and the 3σ of the EV sample at the lowest concentration. The LOD is

found to be 2.18×10^{9} EVs/mL that falls in the range of the clinically relevant concentration of EVs from 1×10^{8} to 3×10^{12} exosomes/mL[190-192]. Therefore, the presented sensor will find it useful in applications of clinic diagnosis. The value of the equilibrium dissociation constant, K_D, can be determined by the ligand half maximal effective concentration (EC_{50}) based on the Michaelis-Menten equation[193, 194]. In our case, based on the obtained dose response in Figure 4-3(b), the value of K_D was found to be $EC_{50} = 2.36\times10^{10}$ EVs/mL using the fitted curve (see red dashed curve).

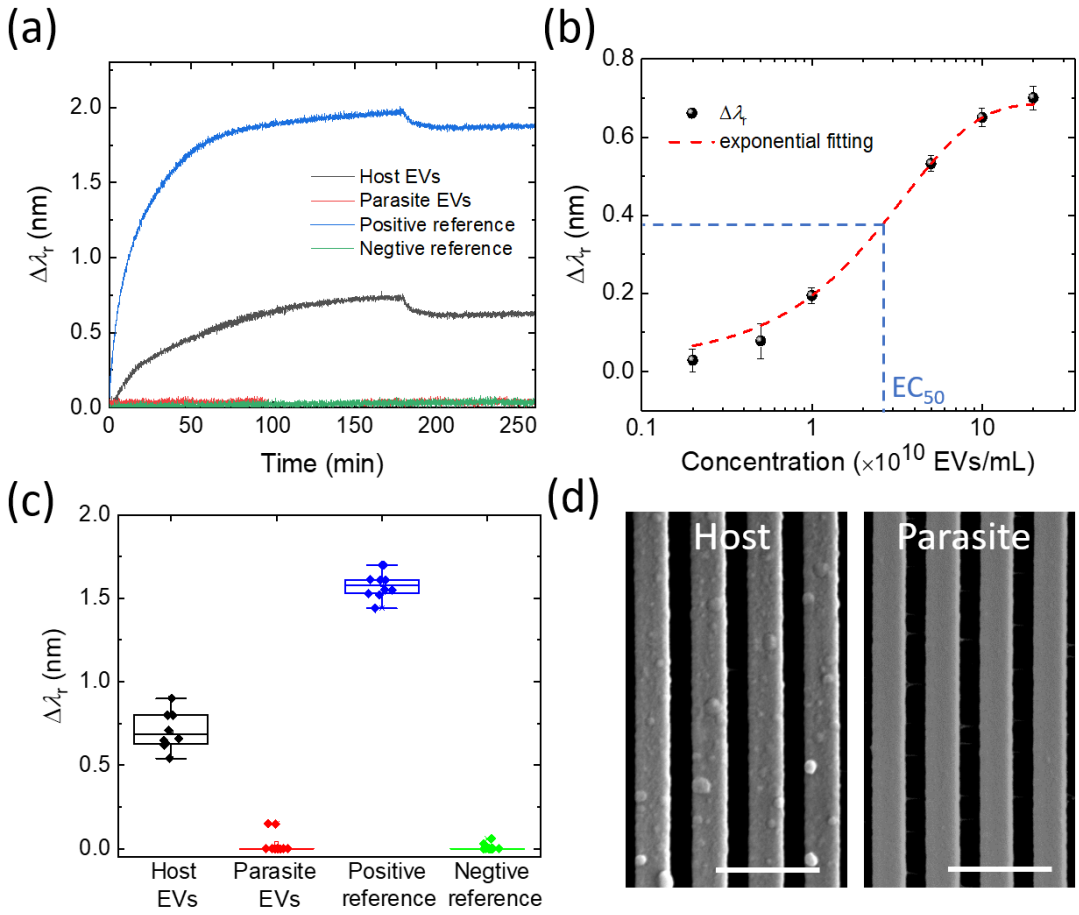

Figure 4-3 (a) Kinetic binding of anti-CD63 with host and parasite EVs at the concentration of c =2×10^{11} EVs/mL. (b) Measured resonance wavelength shifts as a function of 6 different concentrations of EVs from 2×10^{9} EVs/mL to 2×10^{11} EVs/mL. The experiment data is fitted (red dash curve) and the EC_{50} is determined by the blue dash lines. (c) Box plot of the $\Delta\lambda_r$ for host and parasite EVs at 2×10^{11} EVs/mL in comparison to the results of positive and negative references. (d) SEM images of the host and parasite EVs immobilized on the PC surface at the concentrations of 2×10^{11} EVs/mL. Scale bar: 1 μm.

4.4.3 Differentiation of host and parasite EVs

In the present study, the surface protein chosen to distinguish the EVs that are released by the host and the helminth is CD63, which is a well-established exosome marker[195]. Recent studies showed that CD63 presents on the surface of other vesicles too[195]. However, ongoing proteomic analysis by our group demonstrates that the EVs released from *Ascaris suum* do not contain the homologue of CD63, and that CD63 homologues are not found in the *Ascaris* genome. The absence of these proteins strongly suggests that the composition of *Ascaris suum* EVs is different to that from the host cells. Indeed, recent analysis by our group suggests parasite-derived EVs have widespread species- and stage-specific protein composition[196]. Such differences in surface protein expression allows us to develop the EV differentiation assay.

The box plot in Figure 4-3(c) shows the resonance wavelength shift for host and parasite exosome detection with the positive reference and negative reference. Bars indicate mean and 25th and 75th percentiles and lines indicate mean±1.5 times the interquartile range. From the box plot in Figure 4-3(c), the exosome vesicles from the host with a concentration of 2×10^{11} EVs/mL have around 0.7 nm resonance wavelength shift, which this value between the positive reference and negative reference experiment. The detection of the parasite EVs using the anti-CD63 antibody-coated PC sensor generated a nearly zero output. For the positive reference experiment, the EVs were captured regardless of the type of transmembrane proteins. The positive reference experiment shows a signal of 1.6 nm shift. Figure 4-3(c) demonstrate the capability to discriminate EVs from host cells and parasites. Compared to the host EVs, the parasite EVs do not carry CD63 antigens. The details of the PC sensor outputs of the parasite EVs, its positive reference, and negative reference experiments are shown in supporting documentation. The reference experiment can be used

to estimate the noise level of our sensor system. As shown in Figure 4-3(c), the overall system noise level is 0.03 nm, which can be calculated using the standard deviation of the negative reference test. The label-free assay can be utilized to diagnose infectious disease using EVs. Figure 4-3(d) shows the scanning electron microscope (SEM) image of the host EVs and parasite EVs immobilized on the PC surface at the concentrations of 2×10^{11} EVs/mL. The average size of the EVs is approximately 100 nm. The PC-based label-free assay can be used for the rapid differentiation of exosome vesicles from host and parasite in 2 hours.

4.5 **Conclusion**

In summary, we have demonstrated the use of the PC biosensor for rapid and specific discrimination of EVs extracted from the culture media; furthermore, incorporation of the PC biosensor into microfluidic channels allows for parallel quantification of EVs from different sources. The advantages of the PC-based label-free assay include the low-cost and disposable sensor, short assay time, and improved spectral sensitivity. The PC biosensors are less expensive than the gold coated nanohole array used in work of H. Im *et al.*[22] Compared with the SPR device, the narrower linewidth of the PC resonance enables the detection of EVs without using a signal enhancer. Simplicity of the PC-based EV assay would permit detection in non-laboratory settings, thus eliminating the use of additional label reagents. The obtained LOD for pre-cleaned EV samples is 2.18×10^{9} EVs/mL. We expect that the detection limit may be further improved through the use of nanoparticles to enhance the sensor signal or by optimizing the PC structure to achieve resonances with reduced spectral linewidth[197],[148]. This work focused on a single exosomal protein marker but EVs membrane carries more than one markers. The analysis of multiple exosomal markers simultaneously will allow tracking the origin of EVs in complex samples such as blood. Our

future work will utilize the PC-based microarray technology[198] to generate a profile of surface protein markers on the target EVs. With minimal sample processing, simple assay, and high throughput, the implementation of PC biosensor will enable EV analysis in point-of-care applications, such as diagnosis of parasite infections in near future.

4.6 **Supporting information**

4.6.1 Materials and supplies

Phosphate buffered saline (PBS 10×) and bovine serum albumin (BSA) were purchased from Fisher Scientific (Hampton, NH, USA). Polyvinylamine (PVA, Lupamin® 9095) was purchased from BASF (Ludwigshafen, Germany). Glutaraldehyde (GA) solution (25% in H_2O) was purchased from Sigma-Aldrich (St. Louis, MO, USA). Anti-CD63 Antibody, clone RFAC4 is an antibody against CD63 and was purchased from Merck Millipore (Billerica, MA, USA). The host and parasite exosome vesicles (EVs) were isolated from spent murine macrophage and parasitic nematode culture media, respectively. Murine macrophage cell line (J774A.1) was cultured in DMEM containing 10% FBS, 100 units of penicillin, 100 μg/mL of streptomycin, and 2 mM L-glutamine, which were purchased from Sigma-Aldrich (St. Louis, MO, USA). Syringe filters were purchase from MilliporeSigma (Burlington, MA, USA).

4.6.2 Fabrication of photonic crystal (PC) and microfluidic channel

A nano-replica molding technique was used to fabricate the PC structure[186], where a nanopatterned silicon stamp was purchased from LightSmyth Technologies (SNS-C18-2009). This silicon mold carriers a linear grating or PC structure (period: 555.5 nm; depth: 140 nm; ridge width: 340 nm). To transfer the PC structure onto the surface of polymer, a drop of liquid ultraviolet (UV)-curable polymer (NOA-88, Norland Products, Cranbury, NJ) was injected into an air gap formed between the mold and a glass coverslip (24 mm × 60 mm

× 0.1 mm; Fisher Scientific, Hampton, NH). Subsequently, the UV curable polymer was exposed to UV light at room temperature. As a result, the UV-curable polymer was polymerized and the PC was formed at the surface of polymer. After curing, the silicon mold was separated from the replica. The separation was facilitated by pretreatment of the mold with an anti-adhesion saline (Trichloro(1H,1H,2H,2H-perfluorooctyl) silane, Sigma-Aldrich). Next, a TiO_2 layer was deposited over the PC by electron beam evaporation (BJD-1800, Temescal). The thickness and refractive index of the TiO_2 layer were measured using a spectral reflectometer (F20, Filmetrics). To tune the resonance wavelength near 850 nm, the thickness of the TiO_2 layer was chosen as 150 nm. The refractive index of the deposited TiO_2 was 2.2. Figure 4-4(a) shows the fabrication process of the polymer-based PC sensor structure formed on the glass slide.

To form microfluidic channels for the PC sensor (Figure 4-4(b)), a slit was first cut through a 100 µm-thick parafilm sheet (Parafilm® M) by a laser engraving cutting machine. Subsequently, the engraved parafilm was placed between the glass slide with the PC structure and a new glass slide with pre-drilled holes. Finally, the three layers were bonded using a hot press under ~15 kg pressure at 85°C.

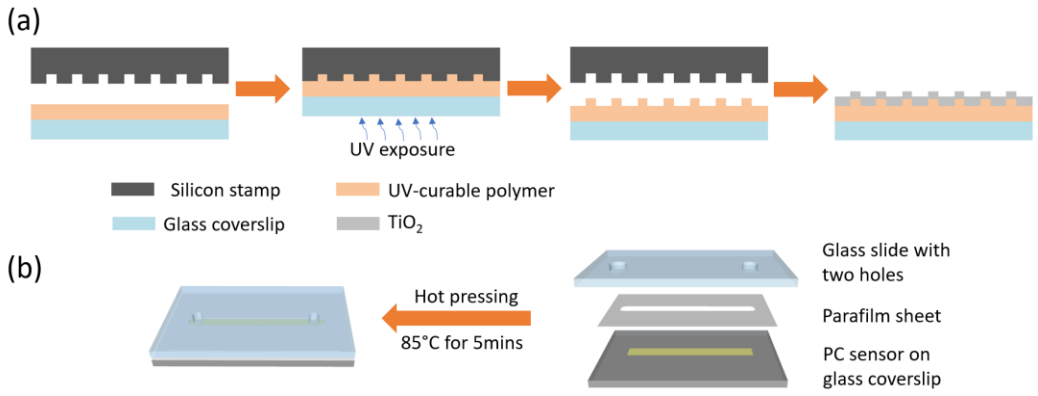

Figure 4-4 Schematics of the fabrication processes for (a) manufacturing of a PC surface and (b) integration of a microfluidic channel with the PC surface.

4.6.3 Sensor surface functionalization

The microfluidic channel with the embedded PC was filled with a diluted PVA solution (1:50 volume ratio in water) and soaked for 12 h, followed by washing with deionized (DI) water for five times. The shift of resonance wavelength was measured. The PVA was attached to the PC surface via non-covalent interactions, providing high-density amine groups. Next, the microfluidic channel was filled with GA solution (25% in water; Sigma-Aldrich) and incubated for 4 h, followed by five times washing with DI water. The GA treatment enabled subsequent covalent attachment of antibody molecules with exposed amine moieties. The GA-induced wavelength resonance shift was measured relative to the PVA coating. Because the binding of antibody to exosome vesicles occur at pH = 7.4, the DI water in the channel was replaced by PBS. The wavelength resonance shift to the solution replacement was also monitored.

4.6.4 Detection setup

The reflection spectra of the sensor were obtained using the setup shown in Figure 4-5. An incident light came from a broadband white light source (HL-2000, Ocean Optics) and coupled into a bifurcated fiber. A linear polarizer was placed between a collimator and the sensor so that only the TM-polarized guided mode resonance (GMR) mode was measured. A ~3 mm-diameter spot in the sensing area was illuminated at normal incidence. The reflected light from the sensor was collected using the bifurcated fiber connected to a spectrometer (USB 2000, Ocean Optics).

When we process the data, we collect the lowest point with ±10 points to do the polynomial fitting. Using this method, we can measure the resonance shift as low as 0.05nm. We will clarify this in the supporting information.

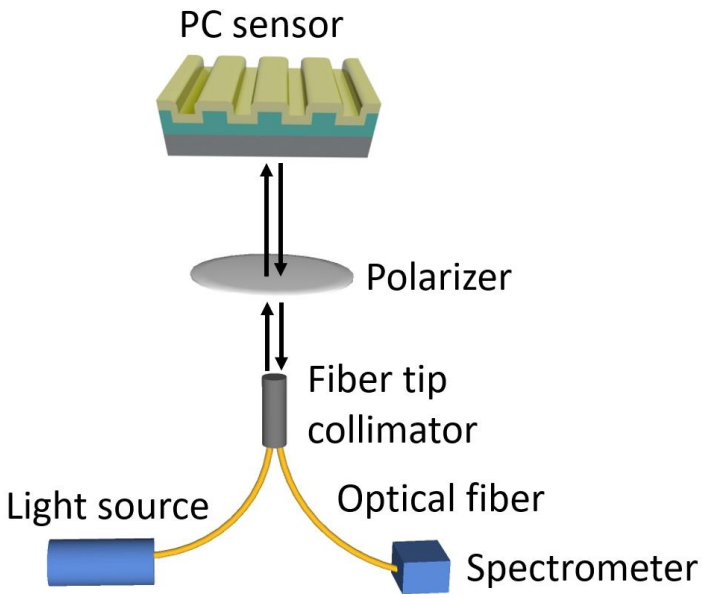

Figure 4-5 Schematic of the optical measurement setup for the sensor

4.6.5 Label-free assay protocol for EVs

The response of the sensor to the EVs extracted from the host cells (J774A.1) is shown in Figure 4-6(a). The results of corresponding positive and negative control experiments are shown in Figure 4-6(b) and Figure 4-6(c), respectively. The first three columns (from left to right) in each panel of Figure 4-6 show the responses of the sensor to the sequential surface treatments with PVA and GA, and surface washing using DI water, and then PBS buffer. The fourth and fifth columns in Figure 4-6(a) show ~0.5 nm and ~0.25 nm resonance wavelength shifts in response to the immobilization of anti-CD63 antibody and BSA blocker, respectively. The sixth column in Figure 4-6(a) shows ~0.7 nm resonance wavelength shift due to the presence of EVs secreted from the host cells. The concentration of the host EVs in Figure 4-6 was 2×10^{11} EVs/mL.

As a positive control, the sensor surface could capture almost all host EVs because it was not functionalized with specific antibody molecules. In this experiment, the sensor surface was treated sequentially using PVA and GA and then washed using PBS buffer.

Because of nonspecific binding, the host EVs were captured onto the GA-treated sensor surface. The last column (from left to right) in Figure 4-6(b) shows a 1.6 nm resonance wavelength shift due to the nonspecific binding of the host EVs onto the sensor surface.

During a negative control experiment, the sensor surface was first functionalized using PVA and GA, and washed using PBS buffer, and then treated with BSA to block the aldehyde groups on the GA layer. Therefore, when CD63 antibody molecules and EVs came to the sensor surface, no responses were observed (Figure 4-6(c)).

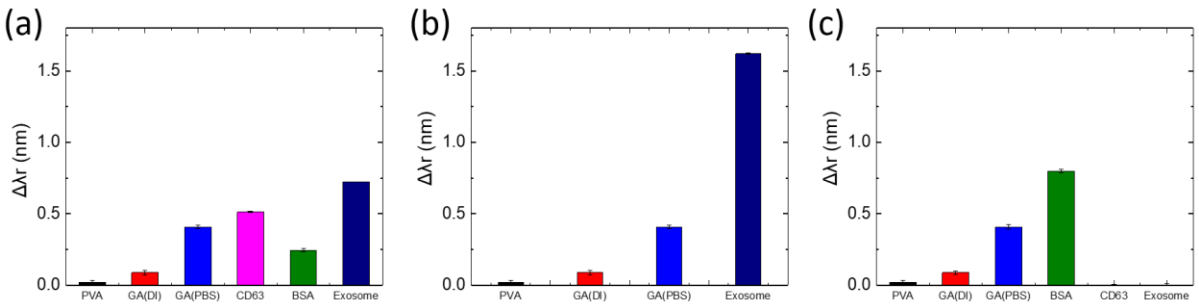

Figure 4-6 Resonance wavelength shifts of the sensor during the assays for (a) the EVs from the host cell (J774A.1) culture, (b) a positive control, and (c) a negative control.

The responses of the sensor to the EVs secreted from parasitic nematodes (*Ascaris suum*) are presented in Figure 4-7(a). The results of corresponding positive and negative control experiments are shown in Figure 4-7(b) and Figure 4-7(c), respectively. Compared to the host EVs, the parasite EVs do not carry CD63 antigen molecules. As a result, almost no resonance wavelength shift was observed from the sensor responding to the presence of the parasite EVs (Figure 4-7(a)). In the positive control experiment, because the EVs could be captured regardless of the type of transmembrane proteins, there exhibited a 1.6 nm resonance wavelength shift.

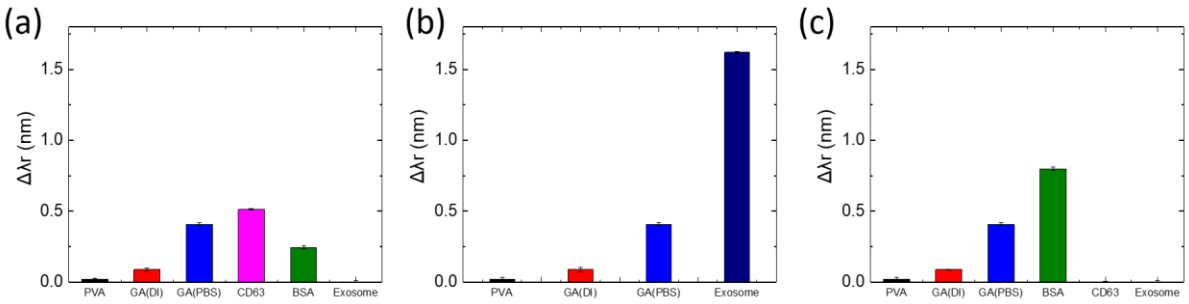

Figure 4-7 Resonance wavelength shifts of the sensor during the assays for (a) the EVs extracted from the parasites (*Ascaris suum*), (b) a positive control, and (c) a negative control.

The results presented in Figure 4-6 and Figure 4-7 demonstrate the ability of the sensor to discriminate the EVs secreted from host cells and parasites. Figure 4-8 shows the scanning electron microscopic (SEM) images of the sensor surfaces with the host EVs (concentration: 2×10^{11} EVs/mL; Figure 4-8(a)), after the positive control experiment (Figure 4-8(b)), and after the negative control experiment (Figure 4-8(c)). These SEM photos were taken after the sensor surface was washed using DI water for three times. Then the photonic crystal biosensor was removed from microfluidics channel, coated with a discharge metal film, and measured using the SEM. The results indicate that the non-specific binding of the positive control results in the highest density of the host EVs presented on the sensor surface, while the BSA blockers led to the lowest density (almost zero) of the host EVs.

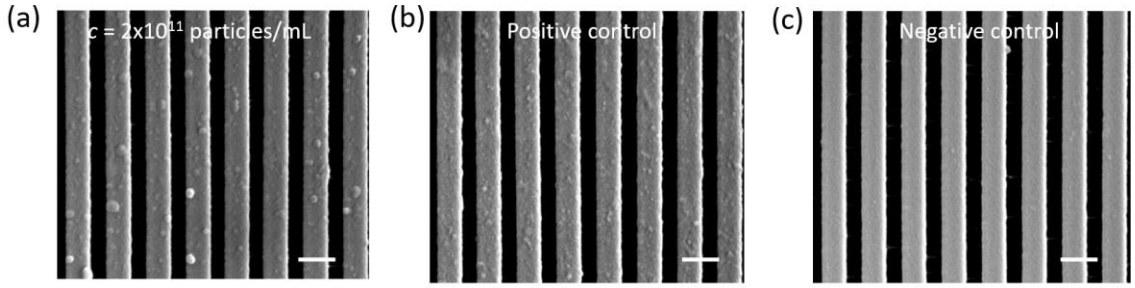

Figure 4-8 SEM images of the host EVs captured by the sensor surface: (a) the original EVs with a concentration of 2×10^{11} EVs/mL, (b) after the positive control, and (c) after the negative control. Scale bars represent 1 μm.

4.6.6 Kinetic binding curve

Figure 4-9 illustrates the kinetic binding of anti-CD63 with host EVs at the concentration of c =2×10^{11} EVs/mL, 5×10^{10} EVs/mL, 1×10^{10} EVs/mL, 5×10^{9} EVs/mL, and 2×10^{9} EVs/mL, respectively. From the kinetic binding curve, the label-free signals still slowly increase at the saturation region. According to the pervious study on the label-free sensorgrams[189, 199-201], our dynamic response curves in Figure 4-9 include both the binding reaction and the EV diffusion processes. In another word, the label-free detection of EVs via CD-63 is not a perfect reaction-limited process.

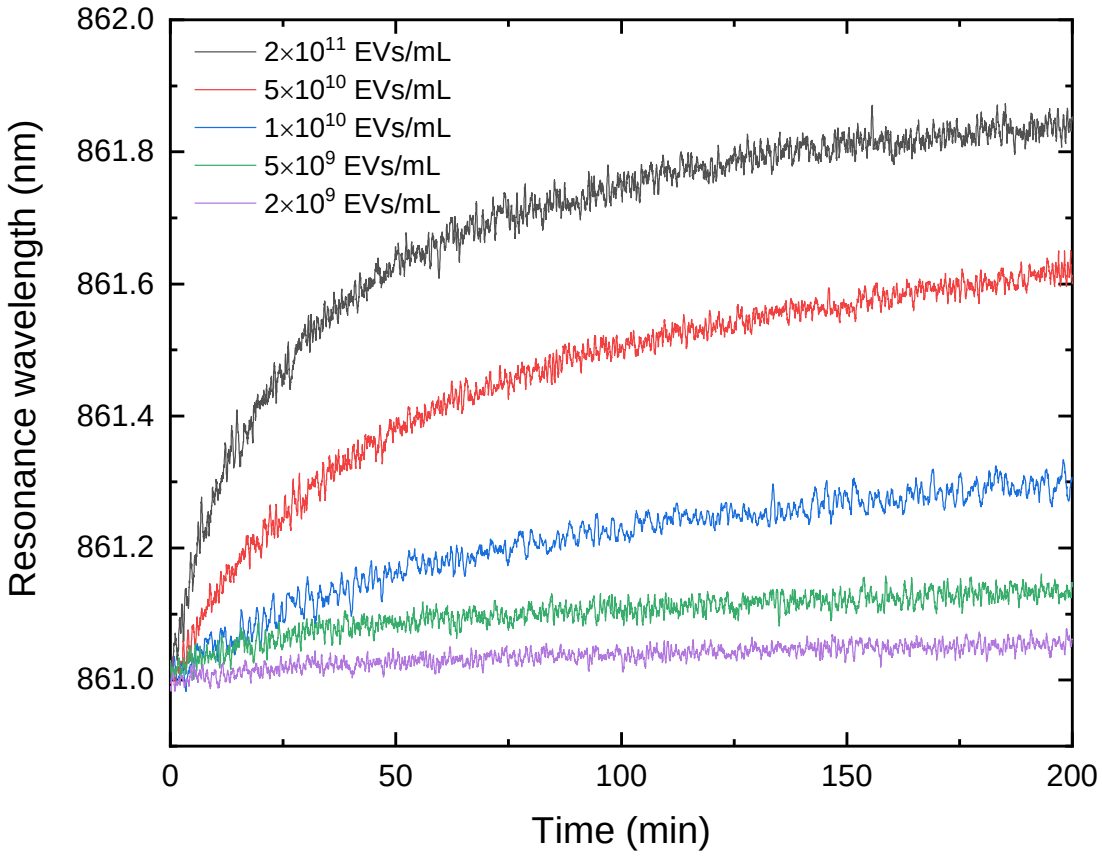

Figure 4-9 Kinetic binding of anti-CD63 with host EVs at the concentration of c =2×10^{11} EVs/mL, 5×10^{10} EVs/mL, 1×10^{10} EVs/mL, 5×10^{9} EVs/mL, and 2×10^{9} EVs/mL, respectively.

4.6.7 Receiver operator characteristic (ROC) analysis

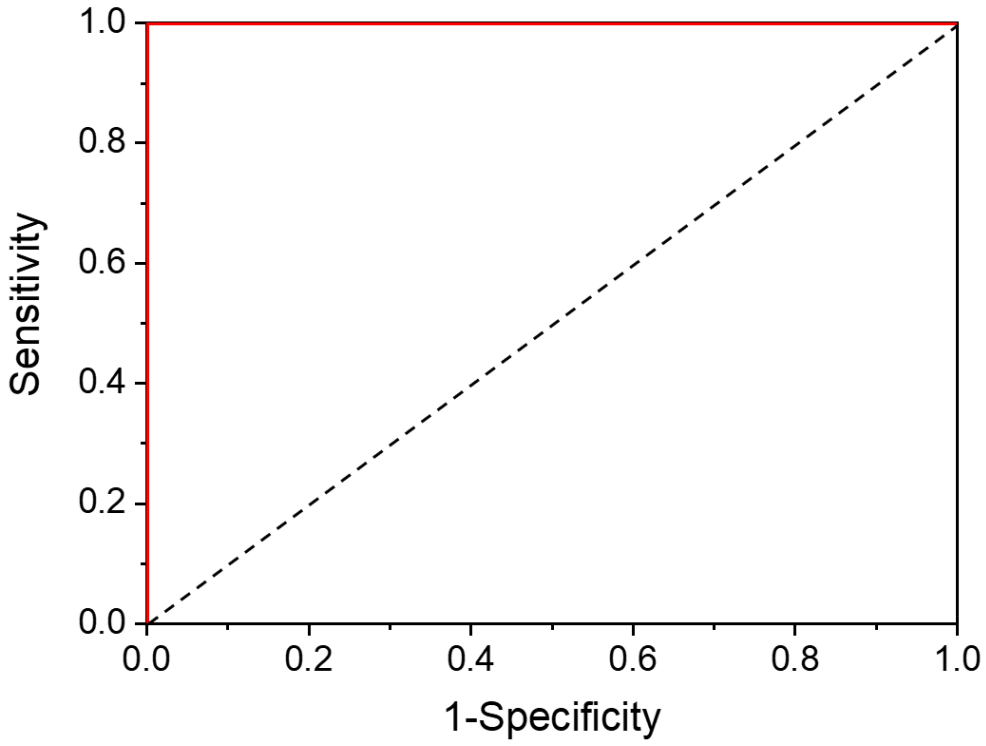

Figure 4-10 Statistical analyses of differentiation of host and parasitic exosome vesicles based on experiment data in Figure 3(c) (main text). According to the ROC curve, the PC-based label-free assay can effectively distinguish these two different types of EVs by setting the threshold signal range from 0.25 nm to 0.5 nm.

4.6.8 ELISA analysis results

To confirm the presence of EVs and compare the LOD of our technology with the gold starndard, we performed the ELISA assay using a commercial CD63 ELISA kit (LifeSpan BioSciences, Inc., Seattle, WA). The dose-response curve of the ELISA assay is shwon in FigureS8. Although the LOD of the label-free EV assay (2.18×10^{9} EVs/mL) is not good as the LOD of the ELISA assay (~1.07×10^{7} EVs/mL), the label-free assay still provides sufficient sensitivity to distinguish different EVs. In particular, the EV samples were extract from cell media and re-suspended in a buffer solution at a relatively high concentration fo 2×10^{11} EVs/mL.

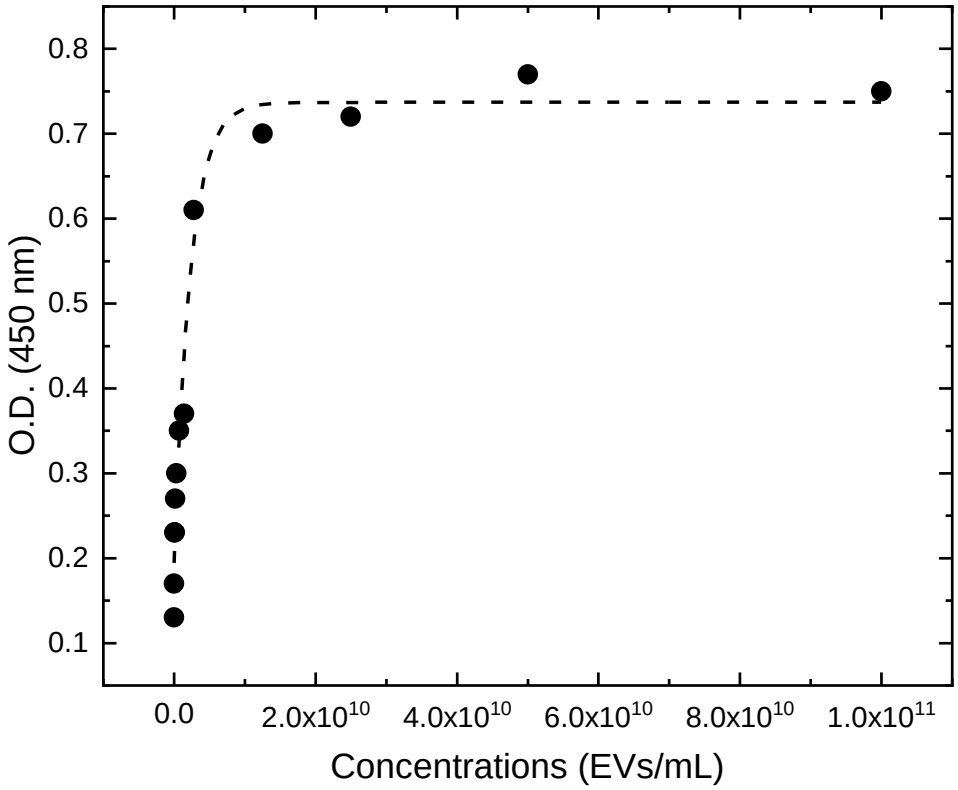

Figure 4-11 Dose response curve of the ELISA assay

4.7 **Acknowledgment**

This work was supported by the United States National Science Foundation under Grant Nos. ECCS 17-11839 and ECCS 16-53673. Any opinions, findings, and conclusions or recommendations expressed in this material are those of the authors and do not necessarily reflect the views of National Science Foundation. This work was supported by an HIH R21 award (AI117204) to MJK. The authors thank the Nano Fabrication Centre at the University of Minnesota for the support of device fabrication. YW acknowledges the Catron Center for Solar Energy Research for the Carton Graduate Fellowship.

CHAPTER 5. EXOSOME MICROARRAY BASED ON LABEL-FREE IMAGING BIOSENSOR

5.1 **Abstract**

Exosome vesicles (EVs) released by macrophages are potential biomarkers for the analysis of immune responses. This study reports a high-throughput EV detection assay developed using a label-free EV microarray. The EV microarray consists of a panel of seven antibodies that are specific to multiple membrane receptors of the target EVs. The EV microarray was fabricated on a photonic crystal (PC) biosensor surface. The hyperspectral imaging approached was implemented to quantify the antibody and EV absorptions on the PC-based microarray. The label-free EV microarray enables low-cost, rapid, and high-throughput characterization of macrophage EVs with a significantly reduced sample volume of 5 μL.

5.2 **Introduction**

Cancer cells secrete cytokines, chemokines and nucleic acids that have traditionally served as biomarkers for disease diagnosis and prognosis. Profoundly, membranous extracellular vesicles, including nanoscale exosomes (~100 nm) and other vesicles actively secreted from cancer cells, have also been found in the blood of cancer patients [157-159]. In particular, exosomes carry molecular constituents of their originating cells, including transmembrane and cytosolic proteins, mRNA, DNA, and microRNA (miRNA), and thus can serve as cellular surrogates [202, 203]. Exosome analysis is minimally invasive and less affected by the scarcity of samples or intratumorally heterogeneity [204]. Recent studies showed that exosomes vesicles (EVs) can transport a variety of molecular constituents, such as proteins, mRNA, and microRNAs, from their originating cells [205]. The analysis of circulating EVs in body fluids has emerged as a promising non-invasive molecular diagnostic

method [17, 206]. The EVs secreted by macrophages are particularly interesting since the macrophage-derived EVs may play a role in immune system responses that can influence the inflammatory response [83, 207]. The objective of the present research is to investigate the effect of exosomes released by lipopolysaccharide (LPS), -induced macrophages on gene expression and cell metabolism of adipocytes, focusing on the differential exosomal miRNA pattern between native and LPS-induced macrophages [207, 208]. LPS, an outer membrane component of Gram-negative bacteria, is a potent activator of monocytes and macrophages. Induced macrophages undergo many changes which allow them to kill invading bacteria or infected cells. They release toxic chemicals and proteins which have toxic effects on other cells.

Existing comprehensive molecular profiling of exosomes is time-consuming and low-throughput [205, 209, 210]. Currently, analyzing extracellular vesicles requires large quantities of vesicles to be prepared and concentrated for immunoblotting or enzyme-linked immunosorbent assay (ELISA) assays [168, 170]. Fluorescence-based approaches, such as bead-based assay, have the multiplexing capability and high sensitivity, but require excessive volumes of serum. In contrast, in order to overcome the challenges of current exosome analysis paradigms exosome analyses, label-free EV analysis have been demonstrated as effective tools for measuring an increasingly diverse range of cellular because they can offer simplified assays by reducing time-consuming labeling processes. The label-free EV microarray is built upon a photonic crystal (PC) biosensor in conjunction with the hyperspectral imaging approach[28, 58, 60, 80].

To analyze the transmembrane receptors carried by EVs, this study demonstrates the EV microarray assay based on the label-free PC biosensor. The PC biosensor, consisting of a

sub-wavelength grating, is essentially a narrowband optical reflector that reflects a particular wavelength of a broadband excitation. The capture of EVs on the biosensor increases the refractive index on the sensor surface and results in a change in the light reflectance of the PC. Our microarray assay is designed to simultaneously measure seven membrane proteins of the macrophage-derived EVs using their corresponding antibodies printed on the EV microarray.

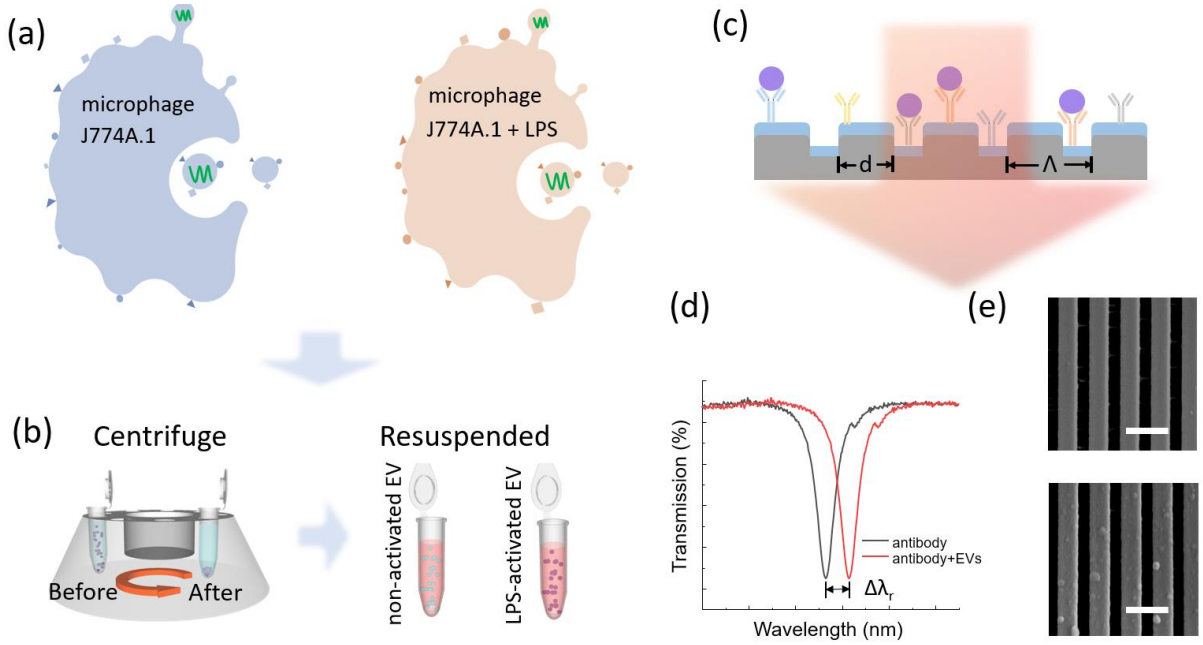

Figure 5-1 Schematic flowchart of the isolation and detection of EVs using the PC biosensor. (a) Secretion of EVs from microphages. (b) EVs are separated from cell culture of macrophages using centrifuge. The extracted EVs are re-suspended in buffer for the subsequent label-free EV analysis. (c) Schematic diagram of the label-free detection of EVs using the PC biosensor that is functionalized with antibody to recognize the target EV (purple dots). (d) Measured transmission spectra before and after the binding of EVs. The spectral position of the minimal transmission represents the resonance wavelength. (e) SEM images of the PC surface before (top) and after (bottom) the immobilization. Scale bar: 800 nm.

5.3 **Results**

5.3.1 EV samples extracted from macrophages

This study developed the label-free EV microarray to investigate two different types of EVs that were secreted by the native microphage and lipopolysaccharide (LPS)-induced macrophage as illustrated in Figure 5-1(a). Macrophages play a key role in LPS-induced sepsis. However, the molecular comparison of exosomes derived from LPS-induced macrophage has not been well analyzed. The macrophage-derived EV (EV_{nat}) is featured with CD63 antigen on its surface. The LPS-treated macrophage-EVs (EV_{LPS}) carries different antigens compared with the control EV_{nat}. Figure 5-1(b) shows the process of EV isolation from the culture medium by centrifugation and resuspension. The details of the materials and supplies are given in the Methods and Material section.

5.3.2 Label-free EV microarray built on PC biosensor

The PC biosensor used in this study consists of a one-dimensional (1D) plastic grating substrate coated with a thin film of titanium oxide (TiO_2). The cross section of a PC biosensor is schematically shown in Figure 5-1(c). Illuminated by a broadband source, the PC substrate exhibits narrowband optical resonances owing to the guided mode resonance effect[38, 211]. The resonances present as the dips in the transmission spectra (Figure 5-1(d)). The spectral signatures, including the resonance wavelength (λ_r) and linewidth, have been exploited for the detection of chemicals and biomolecules[16, 17, 55, 127, 188, 198, 212, 213]. On the surface of a PC biosensor, the absorption of the analyte, such as DNAs, proteins, EVs, or cells, can result in a resonance wavelength shift ($\Delta\lambda_r$) and the shift is proportional to the analyte concentration[182, 214-216].

Details of the PC fabrication are described in the Methods and Material section. In brief, the plastic 1D grating structure was fabricated using the nano-replica molding

method[217]. Following the replica molding, the 100-nm-thick TiO_2 thin film was deposited on the plastic grating by electron beam evaporation. To be specific to a target analyte, the sensor surface needs to be functionalized using the corresponding ligand. For the detection of EVs, the PC biosensors were coated using the antibodies that bind specifically to the EV membrane antigens. Figure 5-1(e) and Figure 5-1(f) shows the scanning electron microscope (SEM) images of the PC surface without (top) and with (bottom) absorbing EVs. The average size of EV is approximately 100 nm. The binding of EV and antibody can redshift the transmission dip by the amount of $\Delta\lambda_r$ as shown in Figure 5-1(d).

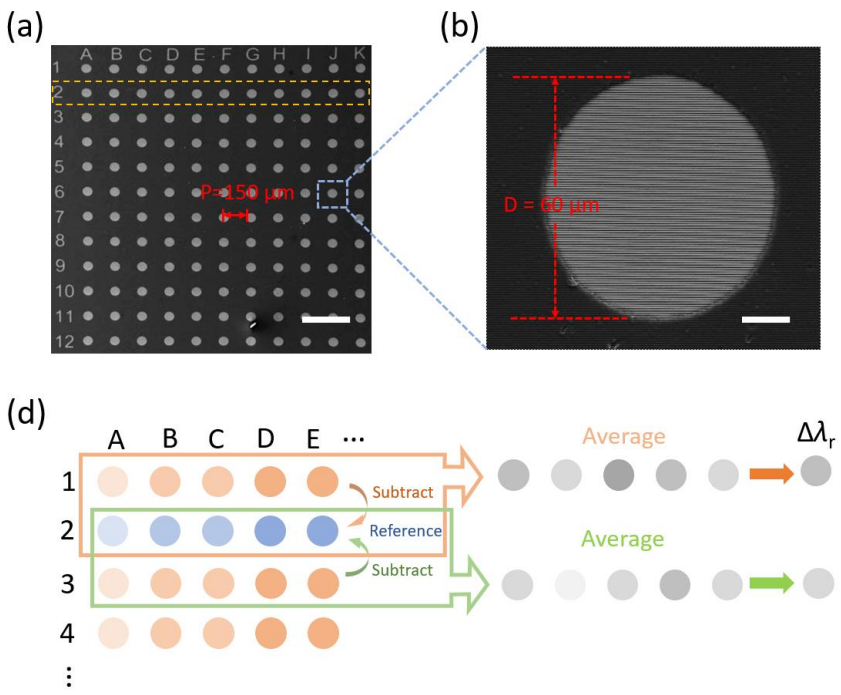

Row #	Printing solutions
1	Anti-CD9
2	Anti-CD63
3	Reference
4	Anti-CD68
5	Anti-CD80
6	Reference
7	Anti-CD81
8	Anti-CD86
9	Reference
10	Anti-I-A/I-E
11	Reference
12	Reference

Figure 5-2 Fabricated EV microarray. (a) SEM image of the array of 60-µm-diameter microwells patterned on the PC substrate using photolithography. Scale bar: 300 µm (b) SEM image of a single microwell with the grating pattern at the bottom. Scale bar: 15 µm (c) List of the printed antibodies and references with the corresponding row numbers. (d) Method to calculate the resonance wavelength shift for the antibodies.

To achieve the simultaneous measurement of multiple membrane proteins carried by the EVs, the microarray was designed and fabricated on the PC substrate. The EV microarray was prepared in two steps. Firstly, the array of microwells was patterned in a layer of photoresist on the PC substrate by photolithography. Figure 5-2(a) shows the EV microarray with 11 × 12 microwells. The diameter and period of the microwell array are 60 μm and 150 μm, respectively. One microwell of the microarray is zoomed in and shown in Figure 5-2(b). The inset SEM image elaborates the PC grating at the bottom of a microwell. Secondly, a molecular printer was used to print antibodies into the microwells [218, 219]. Before printing, the sensor surface inside the microwells was coated using aldehyde functional group to immobilize antibodies. The printings of antibodies were carried out inside an environmental chamber with the constant humidity of 60%. The detailed processes of the microarray fabrication, surface functionalization, and printing are described in the Methods and Material section. Figure 5-2(c) lists the materials printed at different rows (from Row 1 to 12) of the microarray. For each row, the same material was printed. The capture antibodies anti-CD9, anti-CD63, anti-CD68, anti-CD80, anti-CD81, anti-CD86, and anti-I-A/I-E were chosen based on prior studies [220]. Between the nearby rows of antibodies, there was one blank row, which functioned as the reference spots. Figure 5-2(d) shows the method of how the antibody-induced resonance wavelength shift was calculated. For the row of an antibody, the λ_r value of each microwell was calculated by subtracting the λ_r value of the nearby reference microwell. For example, the λ_r values of microwells A2 and B2 were subtracted from the λ_r value of microwells A1 and B1, respectively. Then, the mean value of 11 referenced microwells in the row was calculated to represent the $\Delta\lambda_r$ of the specific antibody.

Later on, the resonance wavelength shifts caused by the blocking and EV detection steps were found using the λ_r value in the same microwell as the baseline.

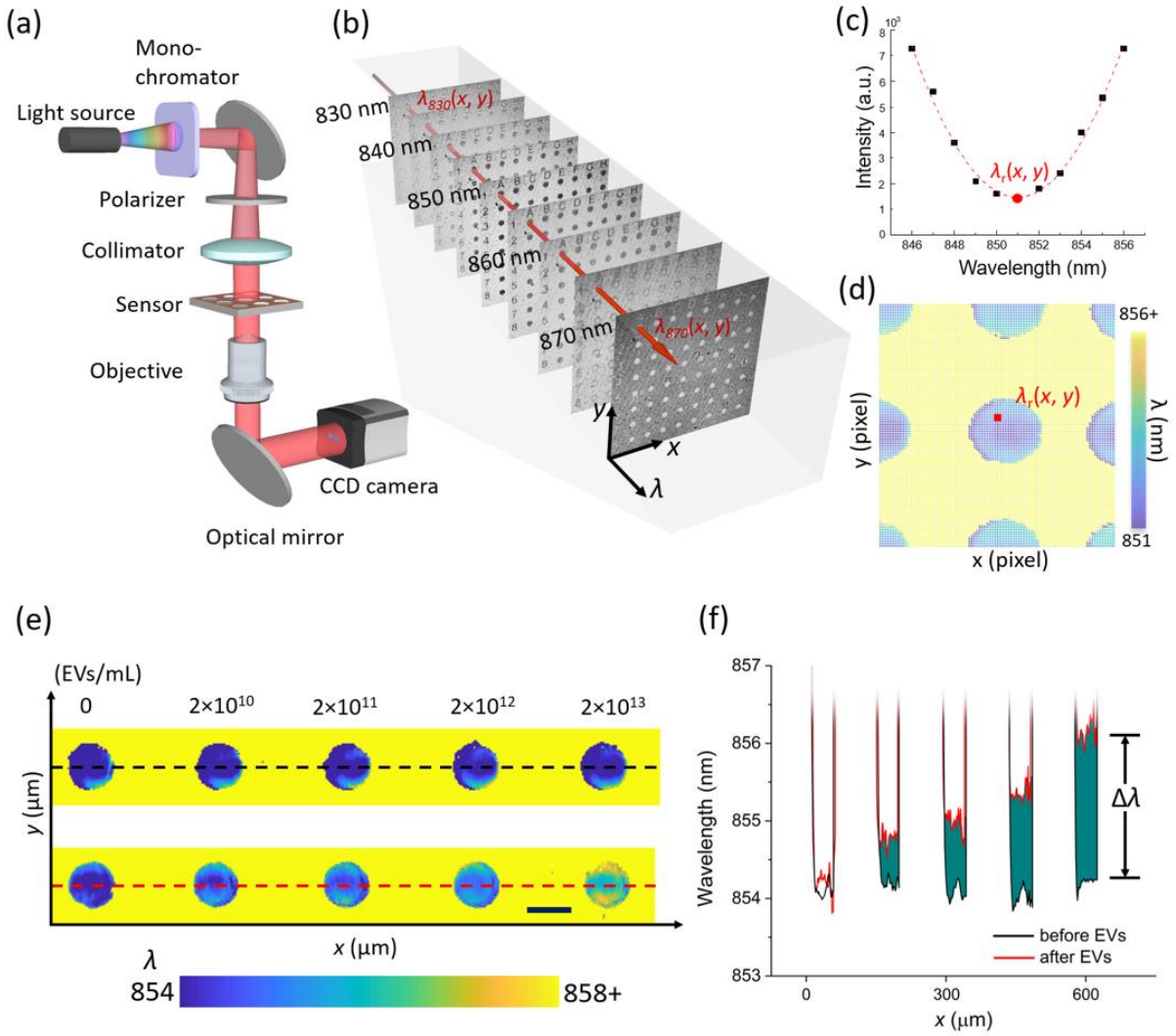

Figure 5-3 Hyperspectral imaging of the label-free EV microarray. (a) Schematic diagram of the hyperspectral imaging-based detection setup. (b) Intensity images captured at nine different wavelengths ranging from 830 nm to 870 nm. Each image consists of 1000 × 1000 pixels with the spatial pixel resolution of 1.8 μm. (c) Reconstructed transmission spectrum at a given pixel in the area of interest. The resonance wavelength of this pixel, $\lambda_r(x, y)$, is determined by a curve fitting algorithm. (d) Label-free image around one microwell. (e) Label-free images of EV microarray. The top panel shows the microarray before print EVs. The lower panel shows the microarray after printing different concentrations of EVs. Scale bar: 60 μm. (f) The profile plot before and after EVs treatment (black dash line and red dash line in (e)). $\Delta\lambda$ represents the wavelength shift induced by the binding of EVs.

5.3.3 Hyperspectral imaging setup

To measure λ_r values of all microwells rapidly, a hyperspectral imaging scheme was adopted. Figure 5-3(a) shows the hyperspectral microscopic imaging setup, whose details are given in the Methods and Material section. In brief, the hyperspectral imaging system was built on an inverted microscope and a tunable monochromatic light source. The wavelength of the monochromatic illumination was selected using a fiber-coupled monochromator. The illumination light was collimated and polarized before it passed through the EV microarray. During a measure, the wavelength was scanned in the vicinity of the PC resonance from 830 nm to 870 nm with the incremental of 1 nm. For each wavelength, the transmission image of the EV microarray was recorded by a CCD camera.

Figure 5-3(b) shows the serial of monochromatic images captured to assemble a hyperspectral image data cube, which contains the spectrally dispersed intensity maps of the entire EV microarray. Following the data acquisition, the data cube was processed to create a label-free resonance image for the microarray, where a single image pixel represents an area on the PC biosensor and its value corresponds to the resonance wavelength shift. Figure 5-3(c) plots the transmission intensity as a function of wavelength for a given single image pixel at (x, y) of the EV microarray from $\lambda_{830}(x, y)$ to $\lambda_{870}(x, y)$. The resonance wavelength $\lambda_r(x, y)$ was determined by fitting the transmission curve as shown by the red dashed line in Figure 5-3(c). There were 1000 × 1000 pixels in each EV microarray image and the resonance wavelength for all these pixels were calculated to build the label–free image. Figure 5-3(d) illustrates the pixelized label–free image consisting of $\lambda_r(x, y)$ values around a single microwell. The blue spot and yellow area represent the regions inside the microwell and photoresist layer, respectively.

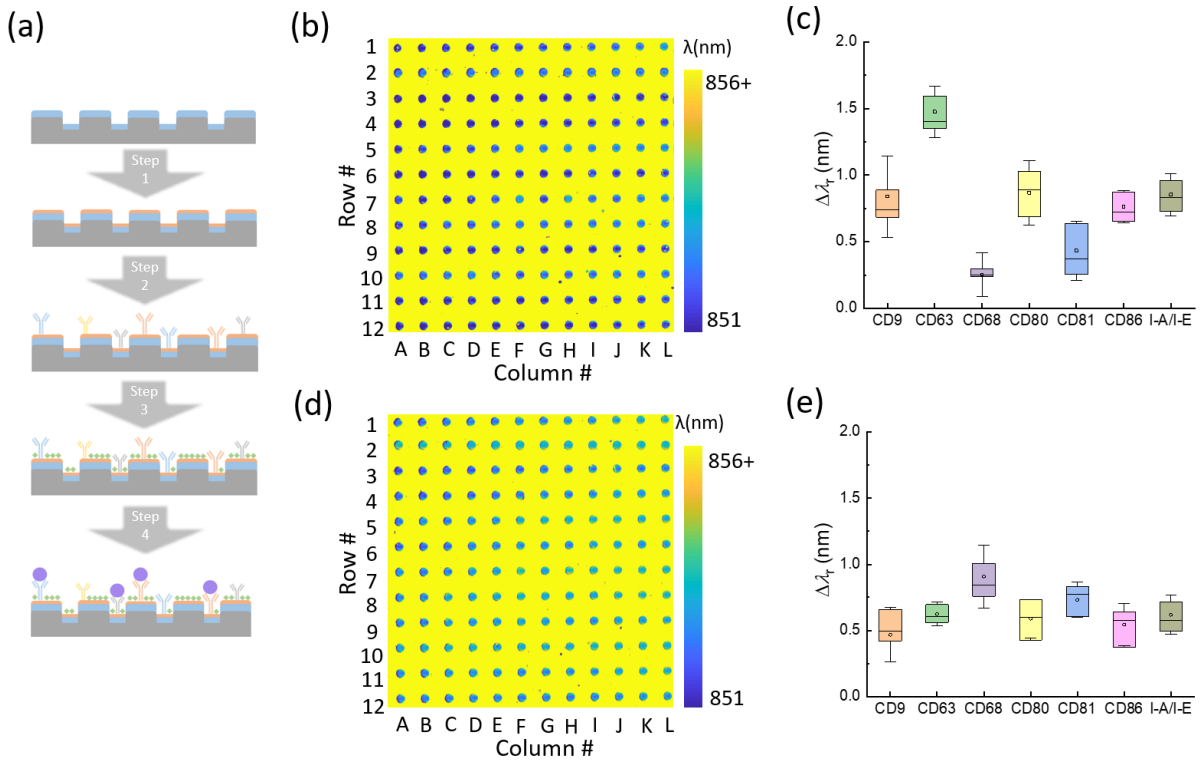

Figure 5-4 Preparation of the label–free microarray for multiplexed EV analysis. (a) Major steps of the label–free EV assay. The surface functionalization, printing of multiple antibodies, and blocking processes are summarized in Step 1–3. Step 4 illustrates the analysis of EVs using the printed microarray. (b) Label–free image of the EV microarray after the printing of seven antibodies. Rows # 3, 6, 9, 11, and 12 are the reference spots without antibody. (c) Box plot of the average resonance wavelength shifts for each antibody. (d) Label–free image obtained after the BSA blocking. This image serves as the baseline to calculate the wavelength shifts induced by the binding of EVs. (e) Resonance wavelength shifts calculated by subtracting the resonance wavelengths before from after the BSA blocking.

To characterize and calibrate the PC sensor, we measured LPS-induced EV samples at a dilution serial of four concentrations ranging from 2×10^{10} particles/mL to 2×10^{13} particles/mL. The samples were diluted consecutively by a factor of ten in PBS. The PC sensor was functionalized using the 0.5 mg/mL CD-63 antibody. Figure 5-3(e) demonstrate the method we calculate the resonance wavelength shift, $\Delta\lambda$. The top panel shows the label–free images for the control experiment, which not print the EVs. The bottom panel shows the label–free images of four concentrations of EVs from 2×10^{10} EVs/mL to 2×10^{13} EVs/mL

with control experiment which contain zero EVs. Each resonance images have the high resonance shift at the boundary because the high refractive index of photoresist with influence the index at the boundary, so the average of the index at the boundary will higher itself. Figure 5-3(f) shows the profile plot before and after EVs treatment. The black line and red line indicate the wavelength profile of the black dash line and red dash line in Figure 5-3(e), respectively. The difference area (green area) between the black and red line illustrate the resonance shift caused by EVs. The PC sensor can measure the lowest concentration at 2×10^{10} that falls in the range of the clinically relevant concentration of EVs from 1×10^{8} to 3×10^{12} particles mL^{-1}[210, 221, 222].

5.3.4 Label–free EV microarray assay

Before the PC biosensor was used for the analysis of EVs, the sensor surface was functionalized using a four-step process reported in our previous work[223]. Major steps of the label-free EV detection assay are summarized in Figure 5-4(a). The initial step (step 1 in Figure 5-4(a)) was the coating of a porous polymer layer (Polyvinylamine, PVA) and a bifunctional linker, glutaraldehyde (GA), on the cleaned blank PC microarray that can provide a high–density amine group. The PVA and GA coating process lasted 5 hours for each process and was followed by a wash using DI water. Before print solution of capture antibodies, the buffer solution was changed to the PBS (pH = 7.4). The capture antibodies were printed at the concentration of at 0.5 mg mL^{-1} (step 2 in Figure 5-4(a)) and were incubated for 4 hours. After the incubation, the microarray was washed in a phosphate buffered saline (PBS) solution to remove the excessive antibodies. Next, the microarray was blocked the unoccupied aldehyde groups on the GA layer for four hours by using the bovine serum albumin (BSA) solution (0.5% in 0.85% sodium chloride) to prevent non–specific

binding (step 3 in Figure 5-4(a)). After the BSA blocking, the PC microarray were ready for the measuring EV binding to the antibodies.

During the EV detection experiment, label–free images of the array were measured after each step shown in Figure 5-4(a). Figure 5-4(b) shows the label–free microarray image measured after the printing of antibodies and before the BSA blocking step. The pseudo–color plot represents the resonance wavelength for the pixels inside the microwells. Since the region out of the microwave was covered by the photoresist, the resonance wavelength of the region was manually set at 1000 nm. The box plot in Figure 5-4(c) shows the resonance wavelength shifts for the panel of antibodies, including CD–9, CD–63, CD–68, CD–80, CD–81, CD–86, and I–A/I–E. Bars indicate mean and 25th and 75th percentiles and lines indicate mean ±1.5 times the interquartile range. For each antibody, the $\Delta\lambda_r$ values were calculated by subtracting of the reference spot from the nearby sample spot to the and averaging the row of 12 spots. Figure 5-4(d) shows the label–free microarray image measured after the BSA blocking step and before the EV binding step. The box plot in Figure 5-4(c) shows the resonance wavelength shifts for the BSA blocking step of the panel of antibodies. For the BSA blocking step, the $\Delta\lambda_r$ values were calculated by subtracting of the spots by previous step (λ_r of antibodies) and averaging the row of 12 spots.

5.3.5 Characterization of EVs from different microphages

Two type of the macrophage–derived EVs sample was added and incubated on the EV microarray for 3 hours. The LiterSlip™ cover glass (Electron Microscope Sciences) with approximate 7.55 µL volume and humidity control environment system was used to incubate the exosome solution in order to reduce the solution evaporation. The concentration and volume of both the EV samples were 2×10^{13} particles mL^{-1} and 5 µL, respectively. Figure 5-5(a) is the label–free image after the EV_{non} absorption. Figure 5-5(b) compares the

resonance wavelength shifts of EV bindings with regard to each antibody. The label–free image measured after the BSA blocking step was used as the baseline to calculate the resonance wavelength shifts. The $\Delta\lambda_r$ for anti–CD68 is highest and anti–CD80 is lowest, which the value is 1.75 nm and 0.32 nm, respectively. Figure 5-5(c) is the label–free image after the EV_{LPS} incubation and binding. The box plot in Figure 5-5(d) shows the resonance wavelength shifts of EV bindings for the antibodies panel. For the EV_{LPS}, the resonance wavelength shift of anti–CD80 is around 1.5 nm and anti-CD9 is 0.3 nm. By compare with the resonance wavelength shift of the EV binding for each antibody, the $\Delta\lambda_r$ of the EV_{non} present the lowest shift but the EV_{LPS} shows the largest. According to the trend of the $\Delta\lambda_r$, it can easily differentiation whether the EV has LPS induced. Figure 5-5(e) shows the antibodies profiling of non-induced macrophage-derived EV and LPS-induced macrophage-derived EV. The radar chart in Figure 5-5(f) display the EV_{non} and EV_{LPS} observations with seven different antibodies. The red area represents the EV_{non} and the blue area shows the EV_{LPS}. The data length of a spoke is proportional to the resonance wavelength shift of the antibody for the data point relative to the maximum magnitude of the antibody across all data points. Based on the radar chart, we can differential the EV_{non} and EV_{LPS} without the same concentrations.

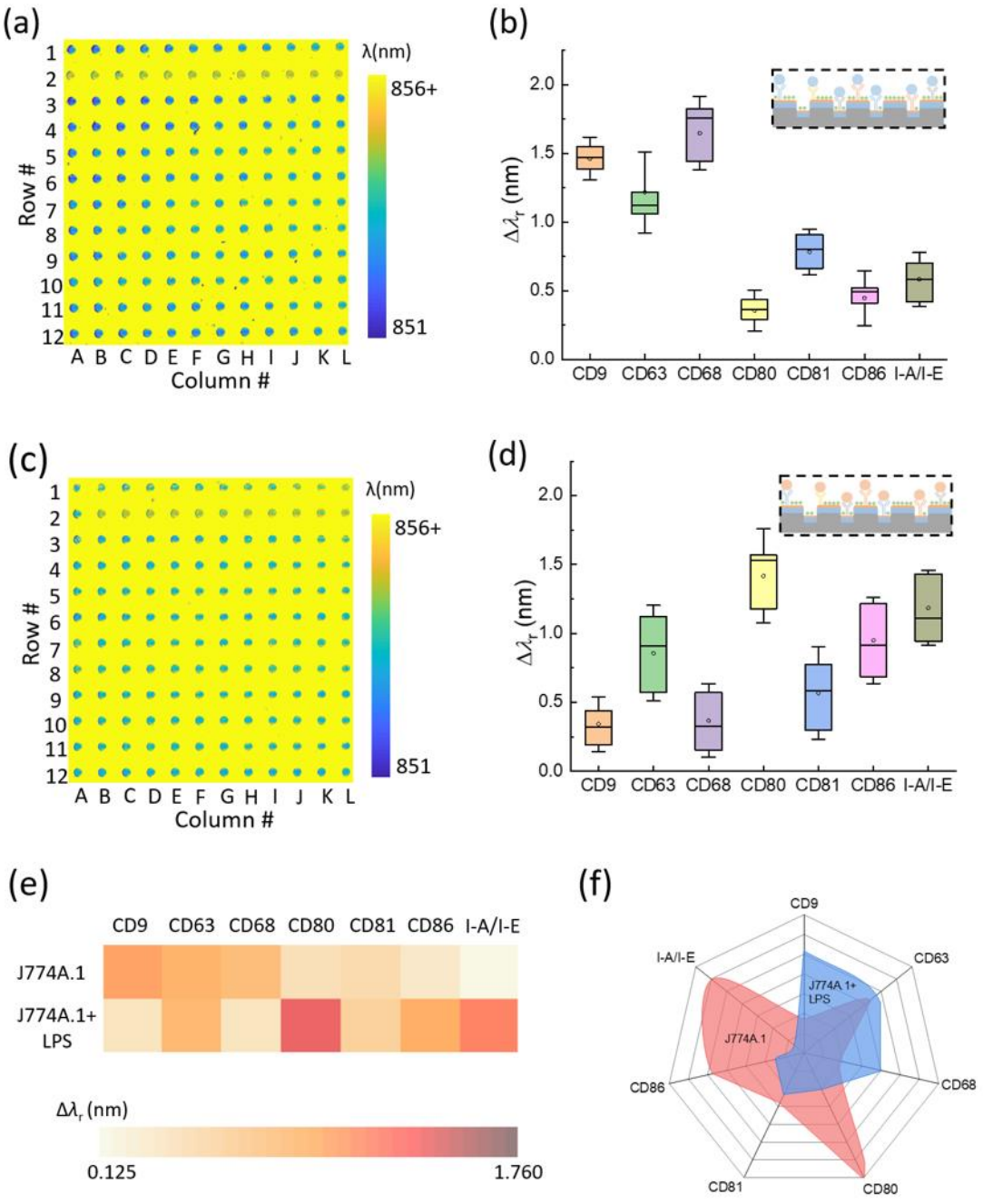

Figure 5-5 Characterization of multiple membrane proteins of EVs secreted by native and LPS-induced macrophages. (a) Label-free image of the bindings of murine macrophage-derived EVs. (b) Box plot of the average resonance wavelength shifts caused by the binding of EV_{nat} to the panel of seven antibodies. (c) Label-free image of the bindings of EVs from the LPS-induced macrophages. (d) Statistical analysis of the binding results of EV_{LPS}. (e) Distribution profiles of membrane proteins on the EVs from native and LPS-induced macrophages, respectively. (f) Radar chart of wavelength shifts measured for the bindings between antibodies and two different types of EVs (EV_{nat} and EV_{LPS}).

5.4 **Methods and Materials**

5.4.1 Preparation of EV samples

Murine macrophage cell line J774A.1 (TIB-67, ATCC) were cultured in Dulbecco's Modified Eagle Medium (DMEM) containing 10% FBS, 100 Units of penicillin, 100 µg/ml of streptomycin, and 2 mM L-glutamine (Sigma-Aldrich, St. Louis, MO). After being cultured at 37 °C with 5% CO_2 for 24 hr, gently rotate the flask with the remaining medium to wash off the dead cells, then aspirate the medium. Wash the cells with 8-10 ml cold DPBS (Dulbecco's Phosphate Buffered Saline, Thermo Fisher Scientific, Waltham, MA), then gently rotate the flask to wash off the dead cells, then aspirate the DPBS. Add 10 ml cold DPBS and leave the flask in 4℃ for 3 min. Then use cell scraper to gently detach the cells. Collect the cells in the DPBS to a 15 ml sterile tube. Centrifuge at 1000 rpm/min for 5 min in a swing bucket centrifuge. Aspirate the DPBS, resuspend the cell pellet with 600 ul culture medium. Transfer 100 ul of the cell suspension to a new T-75 flask with 8-10 ml culture medium. Usually, the cells will reach to ~90 % confluency on day 3 of sub-culturing.

The culture medium was collected and filtered through 0.22 µm filter to remove macrophage and debris, and then loaded on ultracentrifuge tube. To separate EVs from the culture media, EV samples were centrifuged again at 120000g/min for 90 min to collect EVs. Then the pellet was resuspended with PBS and transferred into 1.5 ml Beckman ultracentrifuge tube. Then they were spinned at 55,000 rpm/min for 2 hours and the pellet was resuspended with PBS. All the samples were centrifuged at 4℃. The harvested EVs were stored in a -80 °C freezer for future use.

The concentrations of the resuspended EV samples were measured using a Nanoparticle Tracking Analysis system (NanoSight LM10, Malvern Instruments, Malvern, UK). For EVs concentration measurement, EVs from J774 or worms were diluted 100 times

with PBS and loaded into the nanoparticle analyzer followed the instructions. In brief, three videos were recorded from each sample, each video lasts for 30 sec. Mean concentration were calculated based on the three videos.

5.4.2 Fabrication of PC-based EV microarray

The nano-replica molding technique was used to generate the sub-micron grating pattern. The silicon replication mold stamp was purchased from LightSmyth Technologies (SNS-C18-2009). This silicon stamp carriers a linear grating with the period, depth, and ridge width of 555.5 nm, 140 nm, and 340 nm, respecitvely. To transfer the grating pattern, a drop of liquid ultraviolet (UV)-curable polymer (NOA-88, Norland Products, Cranbury, NJ) was injected into an air gap formed between the mold and a 0.18 mm-thick glass coverslip. Subsequently, the UV curable polymer was crosslinked using UV light at room temperature. As a result, the UV-curable polymer was polymerized and the grating was formed on the surface of polymer. After curing, the silicon mold was carefully separated from the silicon stamp. The separation was facilitated by pretreatment of the mold with an anti-adhesion saline (Trichloro(1H,1H,2H,2H-perfluorooctyl), Sigma-Aldrich). Next, the TiO_2 layer was deposited on the polymer grating using an electron beam evaporation (BJD-1800, Temescal). The thickness and refractive index of the TiO_2 layer were measured using a spectral reflectometer (F20, Filmetrics). To tune the resonance wavelength near 850 nm, the thickness of the TiO_2 layer was chosen as 150 nm and the refractive index of the TiO_2 film was 2.2.

The array of microwells was patterned in a 1.5-μm-thick layer of photoresist (AZ 5214E, MicroChemicals) on the fabricated PC substrate by photolithography. Before the printing of antibodies, the exposed PC surface was coated with aldehyde functional group to immobilize antibodies. To do so, the PC sensor was treated with a diluted polyvinylamine solution (1:50 volume ratio in water) and soaked for 12 h, followed by washing with

deionized (DI) water. The PVAm was attached to the PC surface via non-covalent interactions, providing high-density amine groups. Next, the PC was immersed with GA solution (25% in water; Sigma-Aldrich) and incubated for 4 h, followed by washing with DI water. The GA treatment enabled subsequent covalent attachment of antibody molecules with exposed amine moieties. Because the binding of antibody to exosome vesicles occur at pH = 7.4, then the PC sensors was raised by PBS solutions and ready to use. The antibodies were printed into the microwells using a contact printer (Nano eNabler, BioForce Nanosciences)[218, 219]. The antibodies were mixed with the printing buffer (Spotting Buffer Kit, BioForce Nanosciences) at a ratio of 50:50% (v/v). In each microwell, the sample volume was approximately 6 pL.

5.4.3 Hyperspectral imaging setup

The setup is built based on the body of a standard microscope, but in addition to ordinary bright field imaging, another illumination path is provided from a fiber-coupled broadband high-power tungsten halogen light (OceanOptics HL-2000-HP). A monochromator (Mini-Chrom, Optometrics Corp.) was used to scan the wavelength of the collimated excitation. The bandwidth of the monochromatic light was controlled using the slit size. The monochromatic excitation split to two light paths, one of the light paths coupled in a fiber and connect to a spectrometer (USB2000, OceanOptics) to get the spectra of the light after the monochromator. From the spectra, we can accurate find the wavelength of the monochromator excitation. Another light path is collimated and filtered by a polarizer to illuminate the PC-based EV microarray with light that is polarized with its electric field vector oriented perpendicular to the grating lines. The transmission image was captured using a microscope (IX-81, Olympus) with a 4× objective (Zeiss) and an EMCCD camera (C9100, Hamamatsu) with 1000 × 1000 pixel. The monochromator was tuned from 830 nm to 870 nm

with the increment of 0.5 nm. For each wavelength, the transmission image of the EV microarray was recorded by the CCD to build a data cube. The data cube can be processed to create a label-free resonance image for the microarray, where a single image pixel represents an area on the PC biosensor and its value corresponds to the resonance wavelength shift.

5.5 **Acknowledgment**

This work was supported by the United States National Science Foundation under Grant Nos. ECCS 17-11839 and ECCS 16-53673. Any opinions, findings, and conclusions or recommendations expressed in this material are those of the authors and do not necessarily reflect the views of the National Science Foundation. This work was supported by an HIH R21 award (AI117204) to MJK. YW acknowledges the Catron Center for Solar Energy Research for the Carton Graduate Fellowship.

CHAPTER 6. CONCLUSION

In summary, optical label-free biosensors serve as a powerful detection tool to analyze biomolecular interactions. This type of biosensor can eliminate the effect of the labels on the molecular conformations and can simplify the time and effort required for assay development. This dissertation seeks a novel and efficient modality able to overcome the limitations of low detection sensitivity, slow molecules mass transfer, and poor throughput, that occur in the current optical label-free biosensors.

First, we investigate the optical bound states in the continuum (BIC) of the slotted high-contrast grating (sHCG) structures to increase the sensitivity of the sHCG-based biosensors. The sHCG support BICs and high-Q resonant modes and the slot position can be utilized to tune the linewidth of the high-Q resonances. The eigenvalue solver can directly determine the BICs for different designs of the sHCG structure, and the rigorous coupled-wave analysis is performed to investigate the high-Q resonance phenomena for both TE- and TM-polarized cases.

Then, we propose a lateral flow-through optofluidic biosensor that can overcome the mass-transfer limitation for rapid detection of biomarkers. The HCG-based biosensor is fabricated using the silicon-on-insulator technology. Bonding of a polydimethylsiloxane slab directly onto the surface results in an ultracompact biosensor, where analyte solutions are restricted to flow only in the space between the nanoposts. No flow exists above the nanoposts. The lateral flow-through feature, in conjunction with high-Q resonance modes associated with optical bound states of the sHCG, offers an improved sensitivity to subtle molecule-bonding induced changes in refractive index. The device exhibits a resonance mode around 1550 nm wavelength and provides an index sensitivity of 720 nm/RIU. Biosensing is

conducted to detect the epidermal growth factor receptor 2 (*ErbB2*), a protein biomarker for early-stage breast cancer screening, by monitoring resonance wavelength shifts in response to specific analyte-ligand binding events at the metasurface. The limit of detection of the device is 0.7 ng mL^{-1} for *ErbB2*.

Finally, we develop a high-throughput exosome vesicles (EVs) detection assay by combining the hyperspectral imaging and photonic crystal-based label-free microarray techniques. The EV microarray consists of a panel of seven antibodies that are specific to multiple membrane receptors of the target EVs. The EV microarray is fabricated on a photonic crystal (PC) biosensor surface. The hyperspectral imaging approached is implemented to quantify the antibody and EV absorptions on the PC-based microarray. The label-free EV microarray enables low-cost, rapid, and high-throughput characterization of macrophage EVs with a significantly reduced sample volume of 5 μL.

REFERENCES

[1] E. Crowley, F. Di Nicolantonio, F. Loupakis, and A. Bardelli, "Liquid biopsy: monitoring cancer-genetics in the blood," *Nature Reviews Clinical Oncology,* vol. 10, pp. 472-484, Aug 2013.

[2] K. Pantel and C. Alix-Panabieres, "Real-time Liquid Biopsy in Cancer Patients: Fact or Fiction?," *Cancer Research,* vol. 73, pp. 6384-6388, Nov 1 2013.

[3] L. A. Diaz and A. Bardelli, "Liquid Biopsies: Genotyping Circulating Tumor DNA," *Journal of Clinical Oncology,* vol. 32, pp. 579-+, Feb 20 2014.

[4] E. Heitzer, P. Ulz, and J. B. Geigl, "Circulating Tumor DNA as a Liquid Biopsy for Cancer," *Clinical Chemistry,* vol. 61, pp. 112-123, Jan 2015.

[5] S. Harz, M. Schimmelpfennig, B. T. S. Bui, N. Marchyk, K. Haupt, and K. H. Feller, "Fluorescence optical spectrally resolved sensor based on molecularly imprinted polymers and microfluidics," *Engineering in Life Sciences,* vol. 11, pp. 559-565, Dec 2011.

[6] Y. J. Li, W. H. Xie, and G. J. Fang, "Fluorescence detection techniques for protein kinase assay," *Analytical and Bioanalytical Chemistry,* vol. 390, pp. 2049-2057, Apr 2008.

[7] J. Ma, M. K. Sengupta, D. X. Yuan, and P. K. Dasgupta, "Speciation and detection of arsenic in aqueous samples: A review of recent progress in non-atomic spectrometric methods," *Analytica Chimica Acta,* vol. 831, pp. 1-23, Jun 11 2014.

[8] C. P. Toseland and M. R. Webb, "Fluorescence tools to measure helicase activity in real time," *Methods,* vol. 51, pp. 259-268, Jul 2010.

[9] W. J. Xu, X. Zhao, W. Lv, H. R. Yang, S. J. Liu, H. Liang, *et al.*, "Rational Design of Phosphorescent Chemodosimeter for Reaction-Based One-and Two-Photon and Time-Resolved Luminescent Imaging of Biothiols in Living Cells," *Advanced Healthcare Materials,* vol. 3, pp. 658-669, May 2014.

[10] U. S. Akshath, L. S. Selvakumar, and M. S. Thakur, "Detection of formaldehyde in food samples by enhanced chemiluminescence," *Analytical Methods,* vol. 4, pp. 699-704, Mar 2012.

[11] C. B. Ma, E. S. Yeung, S. D. Qi, and R. Han, "Highly sensitive detection of microRNA by chemiluminescence based on enzymatic polymerization," *Analytical and Bioanalytical Chemistry,* vol. 402, pp. 2217-2220, Feb 2012.

[12] B. N. Wu, C. Y. Hu, X. Q. Hu, H. M. Cao, C. S. Huang, H. B. Shen, *et al.*, "Sensitive ECL immunosensor for detection of retinol-binding protein based on double-assisted signal amplification strategy of multiwalled carbon nanotubes and Ru(bpy)(3)(2+) doped mesoporous silica nanospheres," *Biosensors & Bioelectronics,* vol. 50, pp. 300-304, Dec 15 2013.

[13] N. Gibson, U. Holzwarth, K. Abbas, F. Simonelli, J. Kozempel, I. Cydzik, *et al.*, "Radiolabelling of engineered nanoparticles for in vitro and in vivo tracing applications using cyclotron accelerators," *Archives of Toxicology,* vol. 85, pp. 751-773, Jul 2011.

[14] Y. Qi, N. J. Li, Q. F. Xu, X. W. Xia, J. F. Ge, and J. M. Lu, "A cancer-targetable copolymer containing tyrosine segments for labeling radioactive halogens," *Reactive & Functional Polymers,* vol. 71, pp. 390-394, Apr 2011.

[15] Y. M. Shlyapnikov, E. A. Shlyapnikova, T. Y. Morozova, I. P. Beletsky, and V. N. Morozov, "Detection of microarray-hybridized oligonucleotides with magnetic beads," *Analytical Biochemistry,* vol. 399, pp. 125-131, Apr 1 2010.

[16] Y. Wang, M. A. Ali, E. K. C. Chow, L. Dong, and M. Lu, "An optofluidic metasurface for lateral flow-through detection of breast cancer biomarker," *Biosensors & Bioelectronics,* vol. 107, pp. 224-229, Jun 1 2018.

[17] Y. F. Wang, W. Yuan, M. Kimber, M. Lu, and L. Dong, "Rapid Differentiation of Host and Parasitic Exosome Vesicles Using Microfluidic Photonic Crystal Biosensor," *ACS Sensors,* vol. 3, pp. 1616-1621, Sep 2018.

[18] M. Citartan, S. C. B. Gopinath, J. Tominaga, and T. H. Tang, "Label-free methods of reporting biomolecular interactions by optical biosensors," *Analyst,* vol. 138, pp. 3576-3592, 2013.

[19] T. Liu, X. Chen, C. Y. Hong, X. P. Xu, and H. H. Yang, "Label-free and ultrasensitive electrochemiluminescence detection of microRNA based on long-range self-assembled DNA nanostructures," *Microchimica Acta,* vol. 181, pp. 731-736, Jun 2014.

[20] J. Musayev, Y. Adlguzel, H. Kulah, S. Eminoglu, and T. Akln, "Label-Free DNA Detection Using a Charge Sensitive CMOS Microarray Sensor Chip," *IEEE Sensors Journal,* vol. 14, pp. 1608-1616, May 2014.

[21] Y. Wang, J. Chen, H. P. Jiao, Y. Chen, W. Y. Li, Q. F. Zhang, *et al.*, "Polymer-Templated Perylene-Probe Noncovalent Self-Assembly: A New Strategy for Label-Free Ultrasensitive Fluorescence Turn-On Biosensing," *Chemistry-a European Journal,* vol. 19, pp. 12846-12852, Sep 16 2013.

[22] Y. N. Xia and G. M. Whitesides, "Soft lithography," *Annual Review of Materials Science,* vol. 28, pp. 153-184, 1998.

[23] M. A. Unger, H. P. Chou, T. Thorsen, A. Scherer, and S. R. Quake, "Monolithic microfabricated valves and pumps by multilayer soft lithography," *Science,* vol. 288, pp. 113-116, Apr 7 2000.

[24] A. Densmore, D. X. Xu, P. Waldron, S. Janz, P. Cheben, J. Lapointe, *et al.*, "A silicon-on-insulator photonic wire based evanescent field sensor," *IEEE Photonics Technology Letters,* vol. 18, pp. 2520-2522, Nov-Dec 2006.

[25] M. Lu, S. Choi, C. J. Wagner, J. G. Eden, and B. T. Cunningham, "Label free biosensor incorporating a replica-molded, vertically emitting distributed feedback laser," *Applied Physics Letters,* vol. 92, Jun 30 2008.

[26] C. J. Chang-Hasnain, Y. Zhou, M. C. Y. Huang, and C. Chase, "High-Contrast Grating VCSELs," *IEEE Journal of Selected Topics in Quantum Electronics,* vol. 15, pp. 869-878, May-Jun 2009.

[27] C. Chase, Y. Zhou, and C. J. Chang-Hasnain, "Impact of High Contrast Grating Size in Tunable VCSELs," *2009 Conference on Lasers and Electro-Optics and Quantum Electronics and Laser Science Conference (CLEO/Qels 2009), Vols 1-5,* pp. 431-432, 2009.

[28] W. L. Chen, K. D. Long, M. Lu, V. Chaudhery, H. Yu, J. S. Choi, *et al.*, "Photonic crystal enhanced microscopy for imaging of live cell adhesion," *Analyst,* vol. 138, pp. 5886-5894, 2013.

[29] Q. Guo, H. Zhu, F. Liu, A. Y. Zhu, J. C. Reed, F. Yi, *et al.*, "Silicon-on-Glass Graphene-Functionalized Leaky Cavity Mode Nanophotonic Biosensor," *ACS Photonics,* vol. 1, pp. 221-227, Mar 2014.

[30] T. B. Sun, S. Kan, G. Marriot, and C. Chang-Hasnain, "High-Contrast Grating Resonator for Label-Free Biosensors," *2015 Conference on Lasers and Electro-Optics (CLEO),* 2015.

[31] K. Narsaiah, S. N. Jha, R. Bhardwaj, R. Sharma, and R. Kumar, "Optical biosensors for food quality and safety assurance-a review," *Journal of Food Science and Technology-Mysore,* vol. 49, pp. 383-406, Aug 2012.

[32] R. G. Knobel and A. N. Cleland, "Nanometre-scale displacement sensing using a single electron transistor," *Nature,* vol. 424, pp. 291-293, Jul 17 2003.

[33] C. Nylander, B. Liedberg, and T. Lind, "Gas-Detection by Means of Surface-Plasmon Resonance," *Sensors and Actuators,* vol. 3, pp. 79-88, 1982.

[34] G. H. Yuan, L. Gao, Y. R. Chen, X. L. Liu, J. Wang, and Z. R. Wang, "Improvement of optical sensing performances of a double-slot-waveguide-based ring resonator sensor on silicon-on-insulator platform," *Optik,* vol. 125, pp. 850-854, 2014.

[35] I. M. White and X. D. Fan, "On the performance quantification of resonant refractive index sensors," *Optics Express,* vol. 16, pp. 1020-1028, Jan 21 2008.

[36] F. J. Blanco, M. Agirregabiria, J. Berganzo, K. Mayora, J. Elizalde, A. Calle, *et al.*, "Microfluidic-optical integrated CMOS compatible devices for label-free biochemical sensing," *Journal of Micromechanics and Microengineering,* vol. 16, pp. 1006-1016, May 2006.

[37] F. Cunin, T. A. Schmedake, J. R. Link, Y. Y. Li, J. Koh, S. N. Bhatia, *et al.*, "Biomolecular screening with encoded porous-silicon photonic crystals," *Nature Materials,* vol. 1, pp. 39-41, Sep 2002.

[38] S. S. Wang and R. Magnusson, "Theory and Applications of Guided-Mode Resonance Filters," *Applied Optics,* vol. 32, pp. 2606-2613, May 10 1993.

[39] Y. Zhou, M. C. Y. Huang, C. Chase, V. Karagodsky, M. Moewe, B. Pesala, *et al.*, "High-Index-Contrast Grating (HCG) and Its Applications in Optoelectronic Devices," *IEEE Journal of Selected Topics in Quantum Electronics,* vol. 15, pp. 1485-1499, Sep-Oct 2009.

[40] J. v. Neumann and E. P. Wigner, "Über das Verhalten von Eigenwerten bei adiabatischen Prozessen," *The Collected Works of Eugene Paul Wigner,* pp. 294-297, 1929.

[41] F. H. Stillinger and D. R. Herrick, "Bound states in the continuum," *Physical Review A,* vol. 11, p. 446, 1975.

[42] J. W. Yoon, S. H. Song, and R. Magnusson, "Critical field enhancement of asymptotic optical bound states in the continuum," *Scientific Reports,* vol. 5, Dec 17 2015.

[43] E. Anemogiannis, E. N. Glytsis, and T. K. Gaylord, "Determination of guided and leaky modes in lossless and lossy planar multilayer optical waveguides: Reflection pole method and wavevector density method," *Journal of Lightwave Technology,* vol. 17, pp. 929-941, May 1999.

[44] A. E. Cetin, A. F. Coskun, B. C. Galarreta, M. Huang, D. Herman, A. Ozcan, *et al.*, "Handheld high-throughput plasmonic biosensor using computational on-chip imaging," *Light-Science & Applications,* vol. 3, Jan 2014.

[45] F. Eftekhari, C. Escobedo, J. Ferreira, X. B. Duan, E. M. Girotto, A. G. Brolo, *et al.*, "Nanoholes As Nanochannels: Flow-through Plasmonic Sensing," *Analytical Chemistry,* vol. 81, pp. 4308-4311, Jun 1 2009.

[46] C. Escobedo, A. G. Brolo, R. Gordon, and D. Sinton, "Flow-Through vs Flow-Over: Analysis of Transport and Binding in Nanohole Array Plasmonic Biosensors," *Analytical Chemistry,* vol. 82, pp. 10015-10020, Dec 15 2010.

[47] A. A. Yanik, A. E. Cetin, M. Huang, A. Artar, S. H. Mousavi, A. Khanikaev, *et al.*, "Seeing protein monolayers with naked eye through plasmonic Fano resonances," *Proceedings of the National Academy of Sciences of the United States of America,* vol. 108, pp. 11784-11789, Jul 19 2011.

[48] A. A. Yanik, M. Huang, A. Artar, T. Y. Chang, and H. Altug, "Integrated nanoplasmonic-nanofluidic biosensors with targeted delivery of analytes," *Applied Physics Letters,* vol. 96, Jan 11 2010.

[49] E. M. Southern, "Detection of Specific Sequences among DNA Fragments Separated by Gel-Electrophoresis," *Journal of Molecular Biology,* vol. 98, pp. 503-+, 1975.

[50] S. P. A. Fodor, J. L. Read, M. C. Pirrung, L. Stryer, A. T. Lu, and D. Solas, "Light-Directed, Spatially Addressable Parallel Chemical Synthesis," *Science,* vol. 251, pp. 767-773, Feb 15 1991.

[51] Y. S. Sun, "Use of Microarrays as a High-Throughput Platform for Label-Free Biosensing," *Jala,* vol. 20, pp. 334-353, Aug 2015.

[52] M. E. Caldwell and E. M. Yeatman, "Surface-Plasmon Spatial Light Modulators Based on Liquid-Crystal," *Applied Optics,* vol. 31, pp. 3880-3891, Jul 10 1992.

[53] B. T. Cunningham, P. Li, S. Schulz, B. Lin, C. Baird, J. Gerstenmaier, *et al.*, "Label-free assays on the BIND system," *Journal of Biomolecular Screening,* vol. 9, pp. 481-490, Sep 2004.

[54] B. Lin, P. Li, and B. T. Cunningham, "A label-free biosensor-based cell attachment assay for characterization of cell surface molecules," *Sensors and Actuators B-Chemical,* vol. 114, pp. 559-564, Apr 26 2006.

[55] B. Cunningham, B. Lin, J. Qiu, P. Li, J. Pepper, and B. Hugh, "A plastic colorimetric resonant optical biosensor for multiparallel detection of label-free biochemical interactions," *Sensors and Actuators B-Chemical,* vol. 85, pp. 219-226, Jul 25 2002.

[56] E. A. Lidstone, V. Chaudhery, A. Kohl, V. Chan, T. Wolf-Jensen, L. B. Schook, *et al.*, "Label-free imaging of cell attachment with photonic crystal enhanced microscopy," *Analyst,* vol. 136, pp. 3608-3615, 2011.

[57] P. Y. Li, L. Bo, J. Gerstenmaier, and B. T. Cunningham, "A new method for label-free imaging of biomolecular interactions," *Sensors and Actuators B-Chemical,* vol. 99, pp. 6-13, Apr 15 2004.

[58] Y. Zhuo, H. Hu, W. L. Chen, M. Lu, L. M. Tian, H. J. Yu, *et al.*, "Single nanoparticle detection using photonic crystal enhanced microscopy," *Analyst,* vol. 139, pp. 1007-1015, 2014.

[59] B. Cunningham, J. Qiu, P. Li, and B. Lin, "Enhancing the surface sensitivity of colorimetric resonant optical biosensors," *Sensors and Actuators B-Chemical,* vol. 87, pp. 365-370, Dec 10 2002.

[60] Y. Zhuo and B. T. Cunningham, "Label-Free Biosensor Imaging on Photonic Crystal Surfaces," *Sensors,* vol. 15, pp. 21613-21635, Sep 2015.

[61] D. Fattal, J. J. Li, Z. Peng, M. Fiorentino, and R. G. Beausoleil, "Flat dielectric grating reflectors with focusing abilities," *Nature Photonics,* vol. 4, pp. 466-470, Jul 2010.
[62] F. L. Lu, F. G. Sedgwick, V. Karagodsky, C. Chase, and C. J. Chang-Hasnain, "Planar high-numerical-aperture low-loss focusing reflectors and lenses using subwavelength high contrast gratings," *Optics Express,* vol. 18, pp. 12606-12614, Jun 7 2010.
[63] M. C. Y. Huang, Y. Zhou, and C. J. Chang-Hasnain, "A surface-emitting laser incorporating a high-index-contrast subwavelength grating," *Nature Photonics,* vol. 1, pp. 119-122, Feb 2007.
[64] V. Karagodsky, F. G. Sedgwick, and C. J. Chang-Hasnain, "Theoretical analysis of subwavelength high contrast grating reflectors," *Optics Express,* vol. 18, pp. 16973-16988, Aug 2 2010.
[65] Y. Zhou, M. Moewe, J. Kern, M. C. Y. Huang, and C. J. Chang-Hasnain, "Surface-normal emission of a high-Q resonator using a subwavelength high-contrast grating," *Optics Express,* vol. 16, pp. 17282-17287, Oct 27 2008.
[66] Y. H. Ko, M. Niraula, K. J. Lee, and R. Magnusson, "Properties of wideband resonant reflectors under fully conical light incidence," *Optics Express,* vol. 24, pp. 4542-4551, Mar 7 2016.
[67] J. N. Liu, M. V. Schulmerich, R. Bhargava, and B. T. Cunningham, "Optimally designed narrowband guided-mode resonance reflectance filters for mid-infrared spectroscopy," *Optics Express,* vol. 19, pp. 24182-24197, Nov 21 2011.
[68] K. O. Hill, B. Malo, F. Bilodeau, D. C. Johnson, and J. Albert, "Bragg Gratings Fabricated in Monomode Photosensitive Optical Fiber by Uv Exposure through a Phase Mask," *Applied Physics Letters,* vol. 62, pp. 1035-1037, Mar 8 1993.
[69] R. Slavik, J. Homola, and J. Ctyroky, "Single-mode optical fiber surface plasmon resonance sensor," *Sensors and Actuators B-Chemical,* vol. 54, pp. 74-79, Jan 25 1999.
[70] J. C. Knight, T. A. Birks, P. S. Russell, and D. M. Atkin, "All-silica single-mode optical fiber with photonic crystal cladding," *Optics Letters,* vol. 21, pp. 1547-1549, Oct 1 1996.
[71] D. Taillaert, F. Van Laere, M. Ayre, W. Bogaerts, D. Van Thourhout, P. Bienstman, *et al.*, "Grating couplers for coupling between optical fibers and nanophotonic waveguides," *Japanese Journal of Applied Physics Part 1-Regular Papers Brief Communications & Review Papers,* vol. 45, pp. 6071-6077, Aug 2006.
[72] R. G. Mote, S. F. Yu, W. Zhou, and X. F. Li, "Design and analysis of two-dimensional high-index-contrast grating surface-emitting lasers," *Optics Express,* vol. 17, pp. 260-265, Jan 5 2009.
[73] M. Lu, B. T. Cunningham, S. J. Park, and J. G. Eden, "Vertically emitting, dye-doped polymer laser in the green (lambda similar to 536 nm) with a second order distributed feedback grating fabricated by replica molding," *Optics Communications,* vol. 281, pp. 3159-3162, Jun 1 2008.
[74] N. A. R. Bhat and J. E. Sipe, "Optical pulse propagation in nonlinear photonic crystals," *Physical Review E,* vol. 64, Nov 2001.
[75] M. Soljacic and J. D. Joannopoulos, "Enhancement of nonlinear effects using photonic crystals," *Nature Materials,* vol. 3, pp. 211-219, Apr 2004.

[76] T. Uesugi, B. S. Song, T. Asano, and S. Noda, "Investigation of optical nonlinearities in an ultra-high-Q Si nanocavity in a two-dimensional photonic crystal slab," *Optics Express,* vol. 14, pp. 377-386, Jan 9 2006.

[77] L. Alloatti, D. Korn, C. Weimann, C. Koos, W. Freude, and J. Leuthold, "Second-order nonlinear silicon-organic hybrid waveguides," *Optics Express,* vol. 20, pp. 20506-20515, Aug 27 2012.

[78] Y. Sakurai and F. Koyama, "Control of group delay and chromatic dispersion in tunable hollow waveguide with highly reflective mirrors," *Japanese Journal of Applied Physics Part 1-Regular Papers Short Notes & Review Papers,* vol. 43, pp. 5828-5831, Aug 2004.

[79] E. Chow, A. Grot, L. W. Mirkarimi, M. Sigalas, and G. Girolami, "Ultracompact biochemical sensor built with two-dimensional photonic crystal microcavity," *Optics Letters,* vol. 29, pp. 1093-1095, May 15 2004.

[80] V. Chaudhery, S. George, M. Lu, A. Pokhriyal, and B. T. Cunningham, "Nanostructured Surfaces and Detection Instrumentation for Photonic Crystal Enhanced Fluorescence," *Sensors,* vol. 13, pp. 5561-5584, May 2013.

[81] A. C. Tasolamprou, B. Bellini, D. C. Zografopoulos, E. E. Kriezis, and R. Beccherelli, "Tunable optical properties of silicon-on-insulator photonic crystal slab structures," *Journal of the European Optical Society-Rapid Publications,* vol. 4, 2009.

[82] C. F. R. Mateus, M. C. Y. Huang, Y. F. Deng, A. R. Neureuther, and C. J. Chang-Hasnain, "Ultrabroadband mirror using low-index cladded subwavelength grating," *IEEE Photonics Technology Letters,* vol. 16, pp. 518-520, Feb 2004.

[83] M. Shokooh-Saremi and R. Magnusson, "Properties of two-dimensional resonant reflectors with zero-contrast gratings," *Optics Letters,* vol. 39, pp. 6958-6961, Dec 15 2014.

[84] D. C. Marinica, A. G. Borisov, and S. V. Shabanov, "Bound states in the continuum in photonics," *Physical Review Letters,* vol. 100, May 9 2008.

[85] E. N. Bulgakov and A. F. Sadreev, "Bloch bound states in the radiation continuum in a periodic array of dielectric rods," *Physical Review A,* vol. 90, Nov 3 2014.

[86] E. N. Bulgakov and A. F. Sadreev, "Light trapping above the light cone in a one-dimensional array of dielectric spheres," *Physical Review A,* vol. 92, Aug 10 2015.

[87] P. Paddon and J. F. Young, "Two-dimensional vector-coupled-mode theory for textured planar waveguides," *Physical Review B,* vol. 61, pp. 2090-2101, Jan 15 2000.

[88] V. Pacradouni, W. J. Mandeville, A. R. Cowan, P. Paddon, J. F. Young, and S. R. Johnson, "Photonic band structure of dielectric membranes periodically textured in two dimensions," *Physical Review B,* vol. 62, pp. 4204-4207, Aug 15 2000.

[89] T. Ochiai and K. Sakoda, "Dispersion relation and optical transmittance of a hexagonal photonic crystal slab," *Physical Review B,* vol. 63, Mar 15 2001.

[90] S. H. Fan and J. D. Joannopoulos, "Analysis of guided resonances in photonic crystal slabs," *Physical Review B,* vol. 65, Jun 15 2002.

[91] S. G. Tikhodeev, A. L. Yablonskii, E. A. Muljarov, N. A. Gippius, and T. Ishihara, "Quasiguided modes and optical properties of photonic crystal slabs," *Physical Review B,* vol. 66, Jul 15 2002.

[92] S. P. Shipman and S. Venakides, "Resonant transmission near nonrobust periodic slab modes," *Physical Review E*, vol. 71, Feb 2005.
[93] C. W. Hsu, B. Zhen, J. Lee, S. L. Chua, S. G. Johnson, J. D. Joannopoulos, *et al.*, "Observation of trapped light within the radiation continuum," *Nature*, vol. 499, pp. 188-191, Jul 11 2013.
[94] F. Monticone and A. Alu, "Embedded Photonic Eigenvalues in 3D Nanostructures," *Physical Review Letters*, vol. 112, May 29 2014.
[95] H. Jansen, H. Gardeniers, M. deBoer, M. Elwenspoek, and J. Fluitman, "A survey on the reactive ion etching of silicon in microtechnology," *Journal of Micromechanics and Microengineering*, vol. 6, pp. 14-28, Mar 1996.
[96] S. Tibuleac and R. Magnusson, "Narrow-linewidth bandpass filters with diffractive thin-film layers," *Optics Letters*, vol. 26, pp. 584-586, May 1 2001.
[97] C. J. Chang-Hasnain and W. J. Yang, "High-contrast gratings for integrated optoelectronics," *Advances in Optics and Photonics*, vol. 4, pp. 379-440, Sep 2012.
[98] R. Magnusson, "Wideband reflectors with zero-contrast gratings," *Optics Letters*, vol. 39, pp. 4337-4340, Aug 1 2014.
[99] J.-M. Jin, *The finite element method in electromagnetics*, 2nd ed. New York: John Wiley & Sons, 2002.
[100] E. D. Palik, *Handbook of optical constants of solids*. Orlando: Academic Press, 1985.
[101] H. Kogelnik and C. V. Shank, "Stimulated Emission in a Periodic Structure," *Applied Physics Letters*, vol. 18, pp. 152-&, 1971.
[102] Y. Wang, L. Dong, and M. Lu, "Optical Bound States of 2D High-Contrast Grating for Refractometric Sensing," presented at the Conference on Lasers and Electro-Optics, OSA Technical Digest.
[103] B. Zeng, A. Majumdar, and F. Wang, "Tunable dark modes in one-dimensional "diatomic" dielectric gratings," *Optics Express*, vol. 23, pp. 12478-12487, May 18 2015.
[104] Z. S. Sacks, D. M. Kingsland, R. Lee, and J. F. Lee, "A perfectly matched anisotropic absorber for use as an absorbing boundary condition," *IEEE Transactions on Antennas and Propagation*, vol. 43, pp. 1460-1463, Dec 1995.
[105] H. Y. Wu, C. J. Choi, and B. T. Cunningham, "Plasmonic Nanogap-enhanced Raman Scattering Using a Resonant Nanodome Array," *2012 Conference on Lasers and Electro-Optics (CLEO)*, 2012.
[106] J. S. Salafsky, "Detection of protein conformational change by optical second-harmonic generation," *Journal of Chemical Physics*, vol. 125, Aug 21 2006.
[107] M. Celebrano, X. Wu, M. Baselli, S. Grossmann, P. Biagioni, A. Locatelli, *et al.*, "Mode matching in multiresonant plasmonic nanoantennas for enhanced second harmonic generation," *Nature Nanotechnology*, vol. 10, pp. 412-417, May 2015.
[108] C. J. Choi, Z. Xu, H. Y. Wu, G. L. Liu, and B. T. Cunningham, "Surface-enhanced Raman nanodomes," *Nanotechnology*, vol. 21, Oct 15 2010.
[109] L. Liu, Z. Xu, L. Dong, and M. Lu, "Angular spectrum detection instrument for label-free photonic crystal sensors," *Optics Letters*, vol. 39, pp. 2751-2754, May 1 2014.
[110] W. Zhang, N. Ganesh, I. D. Block, and B. T. Cunningham, "High sensitivity photonic crystal biosensor incorporating nanorod structures for enhanced surface area," *Sensors and Actuators B-Chemical*, vol. 131, pp. 279-284, Apr 14 2008.

[111] H. Im, H. Shao, Y. I. Park, V. M. Peterson, C. M. Castro, R. Weissleder, *et al.*, "Label-free detection and molecular profiling of exosomes with a nano-plasmonic sensor," *Nature Biotechnology*, vol. 32, pp. 490-U219, May 2014.
[112] D. Diaz-Diestra, B. Thapa, J. Beltran-Huarac, B. R. Weiner, and G. Morell, "L-cysteine capped ZnS:Mn quantum dots for room-temperature detection of dopamine with high sensitivity and selectivity," *Biosensors & Bioelectronics*, vol. 87, pp. 693-700, Jan 15 2017.
[113] M. A. Ali, K. Mondal, C. Singh, B. D. Malhotra, and A. Sharma, "Anti-epidermal growth factor receptor conjugated mesoporous zinc oxide nanofibers for breast cancer diagnostics," *Nanoscale*, vol. 7, pp. 7234-7245, 2015.
[114] M. A. Ali, C. Singh, S. Srivastava, P. Admane, V. V. Agrawal, G. Sumana, *et al.*, "Graphene oxide-metal nanocomposites for cancer biomarker detection," *RSC Advances*, vol. 7, pp. 35982-35991, 2017.
[115] I. Navratilova and A. L. Hopkins, "Emerging role of surface plasmon resonance in fragment-based drug discovery," *Future Medicinal Chemistry*, vol. 3, pp. 1809-1820, Oct 2011.
[116] R. L. Rich and D. G. Myszka, "Spying on HIV with SPR," *Trends in Microbiology*, vol. 11, pp. 124-133, Mar 2003.
[117] N. J. de Mol, "Surface Plasmon Resonance for Proteomics," *Chemical Genomics and Proteomics: Reviews and Protocols*, vol. 800, pp. 33-53, 2012.
[118] M. Fivash, E. M. Towler, and R. J. Fisher, "BIAcore for macromolecular interaction," *Current Opinion in Biotechnology*, vol. 9, pp. 97-101, Feb 1998.
[119] A. A. Bergwerff and F. Van Knapen, "Surface plasmon resonance biosensors for detection of pathogenic microorganisms: Strategies to secure food and environmental safety," *Journal of Aoac International*, vol. 89, pp. 826-831, May-Jun 2006.
[120] P. Thillaivinayagalingam, J. Gommeaux, M. McLoughlin, D. Collins, and A. R. Newcombe, "Biopharmaceutical production: Applications of surface plasmon resonance biosensors," *Journal of Chromatography B-Analytical Technologies in the Biomedical and Life Sciences*, vol. 878, pp. 149-153, Jan 15 2010.
[121] J. M. McDonnell, "Surface plasmon resonance: towards an understanding of the mechanisms of biological molecular recognition," *Current Opinion in Chemical Biology*, vol. 5, pp. 572-577, Oct 2001.
[122] T. Xue, X. Cui, W. Guan, Q. Wang, C. Liu, H. Wang, *et al.*, "Surface plasmon resonance technique for directly probing the interaction of DNA and graphene oxide and ultra-sensitive biosensing," *Biosensors & Bioelectronics*, vol. 58, pp. 374-379, Aug 15 2014.
[123] T. Xue, Z. Wang, W. Guan, C. Hou, Z. Shi, W. Zheng, *et al.*, "Investigating the interaction of dye molecules with graphene oxide by using a surface plasmon resonance technique," *RSC Advances*, vol. 4, pp. 50789-50794, 2014.
[124] S. S. Sridharamurthy, L. Dong, and H. R. Jiang, "A microfluidic chemical/biological sensing system based on membrane dissolution and optical absorption," *Measurement Science and Technology*, vol. 18, pp. 201-207, Jan 2007.
[125] X. Fan, I. M. White, S. I. Shopova, H. Zhu, J. D. Suter, and Y. Sun, "Sensitive optical biosensors for unlabeled targets: A review," *Analytica Chimica Acta*, vol. 620, pp. 8-26, Jul 14 2008.

[126] S. Arnold, M. Khoshsima, I. Teraoka, S. Holler, and F. Vollmer, "Shift of whispering-gallery modes in microspheres by protein adsorption," *Optics Letters,* vol. 28, pp. 272-274, Feb 15 2003.
[127] J. T. Heeres, S. H. Kim, B. J. Leslie, E. A. Lidstone, B. T. Cunningham, and P. J. Hergenrother, "Identifying Modulators of Protein-Protein Interactions Using Photonic Crystal Biosensors," *Journal of the American Chemical Society,* vol. 131, pp. 18202-18203, Dec 30 2009.
[128] F. Vollmer and S. Arnold, "Whispering-gallery-mode biosensing: label-free detection down to single molecules," *Nature Methods,* vol. 5, pp. 591-596, Jul 2008.
[129] Y. Z. Sun and X. D. Fan, "Optical ring resonators for biochemical and chemical sensing," *Analytical and Bioanalytical Chemistry,* vol. 399, pp. 205-211, Jan 2011.
[130] T. Sun, S. Kan, G. Marriott, and C. Chang-Hasnain, "High-contrast grating resonators for label-free detection of disease biomarkers," *Scientific Reports,* vol. 6, Jun 6 2016.
[131] C. J. Choi and B. T. Cunningham, "A 96-well microplate incorporating a replica molded microfluidic network integrated with photonic crystal biosensors for high throughput kinetic biomolecular interaction analysis," *Lab on a Chip,* vol. 7, pp. 550-556, 2007.
[132] C. J. Choi and B. T. Cunningham, "Single-step fabrication and characterization of photonic crystal biosensors with polymer microfluidic channels," *Lab on a Chip,* vol. 6, pp. 1373-1380, Oct 2006.
[133] I. M. White, H. Oveys, and X. Fan, "Liquid-core optical ring-resonator sensors," *Optics Letters,* vol. 31, pp. 1319-1321, May 1 2006.
[134] D. Yin, H. Schmidt, J. P. Barber, and A. R. Hawkins, "Integrated ARROW waveguides with hollow cores," *Optics Express,* vol. 12, pp. 2710-2715, Jun 14 2004.
[135] A. G. Brolo, R. Gordon, B. Leathem, and K. L. Kavanagh, "Surface plasmon sensor based on the enhanced light transmission through arrays of nanoholes in gold films," *Langmuir,* vol. 20, pp. 4813-4815, Jun 8 2004.
[136] D. Sinton, R. Gordon, and A. G. Brolo, "Nanohole arrays in metal films as optofluidic elements: progress and potential," *Microfluidics and Nanofluidics,* vol. 4, pp. 107-116, Jan 2008.
[137] Y. Wang, A. Kar, A. Paterson, K. Kourentzi, H. Le, P. Ruchhoeft, *et al.*, "Transmissive Nanohole Arrays for Massively-Parallel Optical Biosensing," *ACS Photonics,* vol. 1, pp. 241-245, Mar 2014.
[138] N. C. Lindquist, A. Lesuffleur, H. Im, and S. H. Oh, "Sub-micron resolution surface plasmon resonance imaging enabled by nanohole arrays with surrounding Bragg mirrors for enhanced sensitivity and isolation," *Lab on a Chip,* vol. 9, pp. 382-387, 2009.
[139] F. Eftekhari, C. Escobedo, J. Ferreira, X. Duan, E. M. Girotto, A. G. Brolo, *et al.*, "Nanoholes As Nanochannels: Flow-through Plasmonic Sensing," *Analytical Chemistry,* vol. 81, pp. 4308-4311, Jun 1 2009.
[140] L. Zhu, W. Yang, and C. J. Chang-Hasnain, "Optical Multiplexer using Vertical Coupler Based on High Contrast Metastructure," *High Contrast Metastructures Ii,* vol. 8633, 2013.
[141] L. Zhu, J. Kapraun, J. Ferrara, and C. J. Chang-Hasnain, "Flexible photonic metastructures for tunable coloration," *Optica,* vol. 2, pp. 255-258, Mar 20 2015.

[142] M. Sun, T. Sun, Y. Liu, L. Zhu, F. Liu, Y. Huang, *et al.*, "Integrated Plasmonic Refractive Index Sensor based on Grating/Metal Film Resonant Structure," *In Proceeding of SPIE*, vol. 9757, pp. 97570Q-1, 2016.
[143] W. Fang, Y. Huang, X. Duan, K. Liu, J. Fei, and X. Ren, "High-reflectivity high-contrast grating focusing reflector on silicon-on-insulator wafer," *Chinese Physics B*, vol. 25, Nov 2016.
[144] S. T. S. Cheung, B. Guan, S. S. Djordjevic, K. Okamoto, and S. J. B. Yoo, "Low-loss and High Contrast Silicon-on-Insulator (SOI) Arrayed Waveguide Grating," *2012 Conference on Lasers and Electro-Optics (CLEO)*, 2012.
[145] J. Ferrara, W. Yang, L. Zhu, P. Qiao, and C. J. Chang-Hasnain, "Heterogeneously integrated long-wavelength VCSEL using silicon high contrast grating on an SOI substrate," *Optics Express*, vol. 23, pp. 2512-2523, Feb 9 2015.
[146] F. Van Laere, T. Claes, J. Schrauwen, S. Scheerlinck, W. Bogaerts, D. Taillaert, *et al.*, "Compact focusing grating couplers for silicon-on-insulator integrated circuits," *IEEE Photonics Technology Letters*, vol. 19, pp. 1919-1921, Nov-Dec 2007.
[147] C. J. Choi, A. R. Belobraydich, L. L. Chan, P. C. Mathias, and B. T. Cunningham, "Comparison of label-free biosensing in microplate, microfluidic, and spot-based affinity capture assays," *Analytical Biochemistry*, vol. 405, pp. 1-10, Oct 1 2010.
[148] Y. Wang, J. Song, L. Dong, and M. Lu, "Optical bound states in slotted high-contrast gratings," *Journal of the Optical Society of America B-Optical Physics*, vol. 33, pp. 2472-2479, Dec 1 2016.
[149] Y. Wang, L. Dong, and M. Lu, "Optical Bound States of 2D High-Contrast Grating for Refractometric Sensing," *2016 Conference on Lasers and Electro-Optics (CLEO)*, 2016.
[150] M. A. Ali, C. Singh, S. Srivastava, P. Admane, V. V. Agrawal, G. Sumana, *et al.*, "Graphene oxide-metal nanocomposites for cancer biomarker detection," *Rsc. Advances.*, vol. 7, pp. 35982-35991, 2017.
[151] M. A. Ali, W. Hong, S. Oren, Q. Wang, Y. Wang, H. Jiang, *et al.*, "Tunable bioelectrodes with wrinkled-ridged graphene oxide surfaces for electrochemical nitrate sensors," *RSC Advances*, vol. 6, pp. 67184-67195, 2016.
[152] M. A. Ali, K. Mondal, Y. Y. Jiao, S. Oren, Z. Xu, A. Sharma, *et al.*, "Microfluidic Immuno-Biochip for Detection of Breast Cancer Biomarkers Using Hierarchical Composite of Porous Graphene and Titanium Dioxide Nanofibers," *ACS Applied Materials & Interfaces*, vol. 8, pp. 20570-20582, Aug 17 2016.
[153] J. T. Gohring, P. S. Dale, and X. Fan, "Detection of HER2 breast cancer biomarker using the opto-fluidic ring resonator biosensor," *Sensors and Actuators B-Chemical*, vol. 146, pp. 226-230, Apr 8 2010.
[154] A. Retolaza, J. Martinez-Perdiguero, S. Merino, M. Morales-Vidal, P. G. Boj, J. A. Quintana, *et al.*, "Organic distributed feedback laser for label-free biosensing of ErbB2 protein biomarker," *Sensors and Actuators B-Chemical*, vol. 223, pp. 261-265, Feb 2016.
[155] Y. Zhu, P. Chandra, and Y. B. Shim, "Ultrasensitive and Selective Electrochemical Diagnosis of Breast Cancer Based on a Hydrazine-Au Nanoparticle-Aptamer Bioconjugate," *Analytical Chemistry*, vol. 85, pp. 1058-1064, Jan 15 2013.
[156] U. Eletxigerra, J. Martinez-Perdiguero, S. Merino, R. Barderas, R. M. Torrente-Rodriguez, R. Villaionga, *et al.*, "Amperometric magnetoimmunosensor for ErbB2

breast cancer biomarker determination in human serum, cell lysates and intact breast cancer cells," *Biosensors & Bioelectronics,* vol. 70, pp. 34-41, Aug 15 2015.

[157] M. P. Bard, J. P. Hegmans, A. Hemmes, T. M. Luider, R. Willemsen, L. A. A. Severijnen, *et al.*, "Proteomic analysis of exosomes isolated from human malignant pleural effusions," *American Journal of Respiratory Cell and Molecular Biology,* vol. 31, pp. 114-121, Jul 2004.

[158] S. Pant, H. Hilton, and M. E. Burczynski, "The multifaceted exosome: Biogenesis, role in normal and aberrant cellular function, and frontiers for pharmacological and biomarker opportunities," *Biochemical Pharmacology,* vol. 83, pp. 1484-1494, Jun 1 2012.

[159] R. J. Simpson, J. W. E. Lim, R. L. Moritz, and S. Mathivanan, "Exosomes: proteomic insights and diagnostic potential," *Expert Review of Proteomics,* vol. 6, pp. 267-283, Jun 2009.

[160] A. H. Buck, G. Coakley, F. Simbari, H. J. McSorley, J. F. Quintana, T. Le Bihan, *et al.*, "Exosomes secreted by nematode parasites transfer small RNAs to mammalian cells and modulate innate immunity," *Nature Communications,* vol. 5, Nov 2014.

[161] M. Zamanian, L. M. Fraser, P. N. Agbedanu, H. Harischandra, A. R. Moorhead, T. A. Day, *et al.*, "Release of Small RNA-containing Exosome-like Vesicles from the Human Filarial Parasite Brugia malayi," *Plos Neglected Tropical Diseases,* vol. 9, Sep 2015.

[162] C. Thery, M. Ostrowski, and E. Segura, "Membrane vesicles as conveyors of immune responses," *Nature Reviews Immunology,* vol. 9, pp. 581-593, Aug 2009.

[163] R. M. Anthony, L. I. Rutitzky, J. F. Urban, M. J. Stadecker, and W. C. Gause, "Protective immune mechanisms in helminth infection," *Nature Reviews Immunology,* vol. 7, pp. 975-987, Dec 2007.

[164] J. P. Hewitson, J. R. Grainger, and R. M. Maizels, "Helminth immunoregulation: The role of parasite secreted proteins in modulating host immunity," *Molecular and Biochemical Parasitology,* vol. 167, pp. 1-11, Sep 2009.

[165] R. M. Maizels and H. J. McSorley, "Regulation of the host immune system by helminth parasites," *Journal of Allergy and Clinical Immunology,* vol. 138, pp. 666-675, Sep 2016.

[166] J. P. Nolan and F. Mandy, "Multiplexed and microparticle-based analyses: Quantitative tools for the large-scale analysis of biological systems," *Cytometry Part A,* vol. 69a, pp. 318-325, May 2006.

[167] M. G. Banigan, P. Kao, J. A. Kozubek, A. R. Winslow, J. Medina, J. Costa, *et al.*, "Differential Expression of Exosomal microRNAs in Prefrontal Cortices of Schizophrenia and Bipolar Disorder Patients," *PLOS One,* vol. 8, Jan 30 2013.

[168] R. M. Lequin, "Enzyme Immunoassay (EIA)/Enzyme-Linked Immunosorbent Assay (ELISA)," *Clinical Chemistry,* vol. 51, pp. 2415-2418, Dec 2005.

[169] D. D. Taylor and C. Gercel-Taylor, "Tumour-derived exosomes and their role in cancer-associated T-cell signalling defects," *British Journal of Cancer,* vol. 92, pp. 305-311, Jan 31 2005.

[170] M. L. Alvarez, M. Khosroheidari, R. K. Ravi, and J. K. DiStefano, "Comparison of protein, microRNA, and mRNA yields using different methods of urinary exosome isolation for the discovery of kidney disease biomarkers," *Kidney International,* vol. 82, pp. 1024-1032, Nov 2012.

[171] M. M. Jorgensen, R. Baek, and K. Varming, "Potentials and capabilities of the Extracellular Vesicle (EV) Array," *Journal of Extracellular Vesicles,* vol. 4, 2015.
[172] W. Chen, K. Long, M. Lu, V. Chaudhery, H. Yu, J. S. Choi, *et al.*, "Photonic crystal enhanced microscopy for imaging of live cell adhesion," *Analyst,* vol. 138, pp. 5886-5894, 2013.
[173] T. Sun, S. Kan, G. Marriot, and C. Chang-Hasnain, "High-Contrast Grating Resonator for Label-Free Biosensors," *2015 Conference on Lasers and Electro-Optics (CLEO),* 2015.
[174] Y. Wang, A. Ali, E. Chow, L. Dong, and M. Lu, "An optofluidic metasurface for lateral flow-through detection of breast cancer biomarker," *Biosensors and Bioelectronics,* vol. 107, pp. 224-229, 2018.
[175] T. Goda, K. Masuno, J. Nishida, N. Kosaka, T. Ochiya, A. Matsumoto, *et al.*, "A label-free electrical detection of exosomal microRNAs using microelectrode array," *Chemical Communications,* vol. 48, pp. 11942-11944, 2012.
[176] L. Zhu, K. Wang, J. Cui, H. Liu, X. Bu, H. L. Ma, *et al.*, "Label-Free Quantitative Detection of Tumor-Derived Exosomes through Surface Plasmon Resonance Imaging," *Analytical Chemistry,* vol. 86, pp. 8857-8864, Sep 2 2014.
[177] I. Zubiri, M. Posada-Ayala, A. Sanz-Maroto, E. Calvo, M. Martin-Lorenzo, L. Gonzalez-Calero, *et al.*, "Diabetic nephropathy induces changes in the proteome of human urinary exosomes as revealed by label-free comparative analysis," *Journal of Proteomics,* vol. 96, pp. 92-102, Jan 16 2014.
[178] J. Su, "Label-Free Single Exosome Detection Using Frequency-Locked Microtoroid Optical Resonators," *ACS Photonics,* vol. 2, pp. 1241-1245, Sep 2015.
[179] K. Lee, H. Shao, R. Weissleder, and H. Lee, "Acoustic Purification of Extracellular Microvesicles," *ACS Nano,* vol. 9, pp. 2321-2327, Mar 2015.
[180] S. Wang, L. Zhang, S. Wan, S. Cansiz, C. Cui, Y. Liu, *et al.*, "Aptasensor with Expanded Nucleotide Using DNA Nanotetrahedra for Electrochemical Detection of Cancerous Exosomes," *ACS Nano,* vol. 11, pp. 3943-3949, Apr 2017.
[181] S. Fan and J. D. Joannopoulos, "Analysis of guided resonances in photonic crystal slabs," *Physical Review B,* vol. 65, Jun 15 2002.
[182] H. Inan, M. Poyraz, F. Inci, M. A. Lifson, M. Baday, B. T. Cunningham, *et al.*, "Photonic crystals: emerging biosensors and their promise for point-of-care applications," *Chemical Society Reviews,* vol. 46, pp. 366-388, Jan 21 2017.
[183] S. O. Meade, M. Chen, M. J. Sailor, and G. M. Miskelly, "Multiplexed DNA Detection Using Spectrally Encoded Porous SiO2 Photonic Crystal Particles," *Analytical Chemistry,* vol. 81, pp. 2618-2625, Apr 1 2009.
[184] A. C. Sharma, T. Jana, R. Kesavamoorthy, L. Shi, M. A. Virji, D. N. Finegold, *et al.*, "A general photonic crystal sensing motif: Creatinine in bodily fluids," *Journal of the American Chemical Society,* vol. 126, pp. 2971-2977, Mar 10 2004.
[185] J. Han, H. J. Kim, L. Sudheendra, S. J. Gee, B. D. Hammock, and I. M. Kennedy, "Photonic Crystal Lab-On-a-Chip for Detecting Staphylococcal Enterotoxin B at Low Attomolar Concentration," *Analytical Chemistry,* vol. 85, pp. 3104-3109, Mar 19 2013.
[186] I. D. Block, L. Chan, and B. T. Cunningham, "Large-area submicron replica molding of porous low-k dielectric films and application to photonic crystal biosensor fabrication," *Microelectronic Engineering,* vol. 84, pp. 603-608, Apr 2007.

[187] Y. Wang, Y. Huang, J. Sun, S. Pandey, and M. Lu, "Guided-mode-resonance-enhanced measurement of thin-film absorption," *Optics Express,* vol. 23, pp. 28567-28573, Nov 2 2015.
[188] D. Gallegos, K. Long, H. Yu, P. P. Clark, Y. Lin, S. George, *et al.*, "Label-free biodetection using a smartphone," *Lab on a Chip,* vol. 13, pp. 2124-2132, 2013.
[189] R. W. Glaser, "Antigen-Antibody Binding and Mass-Transport by Convection and Diffusion to a Surface - a 2-Dimensional Computer-Model of Binding and Dissociation Kinetics," *Analytical Biochemistry,* vol. 213, pp. 152-161, Aug 15 1993.
[190] A. A. Ibn Sina, R. Vaidyanathan, S. Dey, L. G. Carrascosa, M. J. A. Shiddiky, and M. Trau, "Real time and label free profiling of clinically relevant exosomes," *Scientific Reports,* vol. 6, Jul 28 2016.
[191] J. de Vrij, S. L. N. Maas, M. van Nispen, M. Sena-Esteves, R. W. A. Limpens, A. J. Koster, *et al.*, "Quantification of nanosized extracellular membrane vesicles with scanning ion occlusion sensing," *Nanomedicine,* vol. 8, pp. 1443-1458, Sep 2013.
[192] X. Y. Huang, T. Z. Yuan, M. Tschannen, Z. F. Sun, H. Jacob, M. J. Du, *et al.*, "Characterization of human plasma-derived exosomal RNAs by deep sequencing," *Bmc Genomics,* vol. 14, May 10 2013.
[193] E. C. Hulme and M. A. Trevethick, "Ligand binding assays at equilibrium: validation and interpretation," *British Journal of Pharmacology,* vol. 161, pp. 1219-1237, Nov 2010.
[194] U. Deichmann, S. Schuster, J. P. Mazat, and A. Cornish-Bowden, "Commemorating the 1913 Michaelis-Mentenpaper Die Kinetik der Invertinwirkung: three perspectives," *Febs Journal,* vol. 281, pp. 435-463, Jan 2014.
[195] J. Kowal, G. Arras, M. Colombo, M. Jouve, J. P. Morath, B. Primdal-Bengtson, *et al.*, "Proteomic comparison defines novel markers to characterize heterogeneous populations of extracellular vesicle subtypes," *Proceedings of the National Academy of Sciences of the United States of America,* vol. 113, pp. E968-E977, Feb 23 2016.
[196] H. Harischandra, W. Yuan, H. Loghry, M. Zamanian, and M. Kimber, "Profiling extracellular vesicle release by the filarial nematode Brugia malayi reveals sex-specific differences in cargo and a sensitivity to ivermectin," *PLoS neglected tropical diseases,* vol. 12, pp. e0006438-e0006438, 2018.
[197] Y. Zhao, M. Cao, J. F. McClelland, Z. Shao, and M. Lu, "A photoacoustic immunoassay for biomarker detection," *Biosensors & Bioelectronics,* vol. 85, pp. 261-266, Nov 15 2016.
[198] C. Huang, S. George, M. Lu, V. Chaudhery, R. Tan, R. C. Zangar, *et al.*, "Application of Photonic Crystal Enhanced Fluorescence to Cancer Biomarker Microarrays," *Analytical Chemistry,* vol. 83, pp. 1425-1430, Feb 15 2011.
[199] D. J. Oshannessy, M. Brighamburke, K. K. Soneson, P. Hensley, and I. Brooks, "Determination of Rate and Equilibrium Binding Constants for Macromolecular Interactions Using Surface-Plasmon Resonance - Use of Nonlinear Least-Squares Analysis-Methods," *Analytical Biochemistry,* vol. 212, pp. 457-468, Aug 1 1993.
[200] http://www.bio-rad.com/webroot/web/pdf/lsr/literature/Bulletin_6044A.pdf.
[201] https://www.sprpages.nl/sensorgram-tutorial/exponential.
[202] K. A. Ahmed and J. Xiang, "Mechanisms of cellular communication through intercellular protein transfer," *Journal of Cellular and Molecular Medicine,* vol. 15, pp. 1458-1473, Jul 2011.

[203] S. Rana, S. J. Yue, D. Stadel, and M. Zoller, "Toward tailored exosomes: The exosomal tetraspanin web contributes to target cell selection," *International Journal of Biochemistry & Cell Biology*, vol. 44, pp. 1574-1584, Sep 2012.

[204] H. L. Shao, J. Chung, L. Balaj, A. Charest, D. D. Bigner, B. S. Carter, *et al.*, "Protein typing of circulating microvesicles allows real-time monitoring of glioblastoma therapy," *Nature Medicine*, vol. 18, pp. 1835-+, Dec 2012.

[205] H. Im, H. L. Shao, Y. I. Park, V. M. Peterson, C. M. Castro, R. Weissleder, *et al.*, "Label-free detection and molecular profiling of exosomes with a nano-plasmonic sensor," *Nature Biotechnology*, vol. 32, pp. 490-U219, May 2014.

[206] S. D. Ibsen, J. Wright, J. M. Lewis, S. Kim, S. Y. Ko, J. Ong, *et al.*, "Rapid Isolation and Detection of Exosomes and Associated Biomarkers from Plasma," *ACS Nano*, vol. 11, pp. 6641-6651, Jul 2017.

[207] N. De Silva, M. Samblas, J. A. Martinez, and F. I. Milagro, "Effects of exosomes from LPS-activated macrophages on adipocyte gene expression, differentiation, and insulin-dependent glucose uptake," *Journal of Physiology and Biochemistry*, vol. 74, pp. 559-568, Nov 2018.

[208] F. Y. Meng and C. A. Lowell, "Lipopolysaccharide (LPS)-induced macrophage activation and signal transduction in the absence of Src-family kinases Hck, Fgr, and Lyn," *Journal of Experimental Medicine*, vol. 185, pp. 1661-1670, May 5 1997.

[209] L. Wu and X. G. Qu, "Cancer biomarker detection: recent achievements and challenges," *Chemical Society Reviews*, vol. 44, pp. 2963-2997, 2015.

[210] J. Conde-Vancells, E. Rodriguez-Suarez, N. Embade, D. Gil, R. Matthiesen, M. Valle, *et al.*, "Characterization and Comprehensive Proteome Profiling of Exosomes Secreted by Hepatocytes," *Journal of Proteome Research*, vol. 7, pp. 5157-5166, Dec 2008.

[211] S. S. Wang, R. Magnusson, J. S. Bagby, and M. G. Moharam, "Guided-Mode Resonances in Planar Dielectric-Layer Diffraction Gratings," *Journal of the Optical Society of America a-Optics Image Science and Vision*, vol. 7, pp. 1470-1474, Aug 1990.

[212] Y. F. Wang, Y. Huang, J. X. Sun, S. Pandey, and M. Lu, "Guided-mode-resonance-enhanced measurement of thin-film absorption," *Optics Express*, vol. 23, pp. 28567-28573, Nov 2 2015.

[213] S. M. Shamah and B. T. Cunningham, "Label-free cell-based assays using photonic crystal optical biosensors," *Analyst*, vol. 136, pp. 1090-1102, 2011.

[214] J. H. Han, H. J. Kim, L. Sudheendra, S. J. Gee, B. D. Hammock, and I. M. Kennedy, "Photonic Crystal Lab-On-a-Chip for Detecting Staphylococcal Enterotoxin B at Low Attomolar Concentration," *Analytical Chemistry*, vol. 85, pp. 3104-3109, Mar 19 2013.

[215] S. O. Meade, M. Y. Chen, M. J. Sailor, and G. M. Miskelly, "Multiplexed DNA Detection Using Spectrally Encoded Porous SiO2 Photonic Crystal Particles," *Analytical Chemistry*, vol. 81, pp. 2618-2625, Apr 1 2009.

[216] A. C. Sharma, T. Jana, R. Kesavamoorthy, L. J. Shi, M. A. Virji, D. N. Finegold, *et al.*, "A general photonic crystal sensing motif: Creatinine in bodily fluids," *Journal of the American Chemical Society*, vol. 126, pp. 2971-2977, Mar 10 2004.

[217] I. D. Block, L. L. Chan, and B. T. Cunningham, "Large-area submicron replica molding of porous low-k dielectric films and application to photonic crystal biosensor fabrication," *Microelectronic Engineering*, vol. 84, pp. 603-608, Apr 2007.
[218] S. Nettikadan, K. Radke, J. Johnson, J. T. Xu, M. Lynch, C. Mosher, *et al.*, "Detection and quantification of protein biomarkers from fewer than 10 cells," *Molecular & Cellular Proteomics*, vol. 5, pp. 895-901, May 2006.
[219] J. T. Xu, M. Lynch, S. Nettikadan, C. Mosher, S. Vegasandra, and E. Henderson, "Microfabricated "Biomolecular Ink Cartridges" - Surface patterning tools (SPTs) for the printing of multiplexed biomolecular arrays," *Sensors and Actuators B-Chemical*, vol. 113, pp. 1034-1041, Feb 27 2006.
[220] F. O. Martinez and S. Gordon, "The M1 and M2 paradigm of macrophage activation: time for reassessment," *F1000Prime Rep*, vol. 6, p. 13, 2014.
[221] A. A. Sina, R. Vaidyanathan, S. Dey, L. G. Carrascosa, M. J. Shiddiky, and M. Trau, "Real time and label free profiling of clinically relevant exosomes," *Scientific Reports*, vol. 6, p. 30460, Jul 28 2016.
[222] J. de Vrij, S. L. Maas, M. van Nispen, M. Sena-Esteves, R. W. Limpens, A. J. Koster, *et al.*, "Quantification of nanosized extracellular membrane vesicles with scanning ion occlusion sensing," *Nanomedicine (Lond)*, vol. 8, pp. 1443-58, Sep 2013.
[223] D. Gallegos, K. D. Long, H. J. Yu, P. P. Clark, Y. X. Lin, S. George, *et al.*, "Label-free biodetection using a smartphone," *Lab on a Chip*, vol. 13, pp. 2124-2132, 2013.